$[Ca_{24}Al_{28}O_{64}]^{4+}(e^-)_4$ electride as a novel support system for iron-based Fischer-Tropsch synthesis

MUHAMMAD MOTALA

SUPERVISOR: DR NICO FISCHER

CO-SUPERVISOR: PROFESSOR MICHAEL CLAEYS

DEPARTMENT OF CHEMICAL ENGINEERING, UCT

Thesis submission for the degree of

MSc in Chemical Engineering

December 2017

cchange DST-NRF Centre of Excellence in Catalysis

UNIVERSITY OF CAPE TOWN
CENTRE FOR CATALYSIS RESEARCH

NRF

ACKNOWLEDGEMENTS

All praise to God. This thesis is dedicated to all those researchers around the world who have persevered despite having physical, mental and financial obstacles in their way.

I am grateful for this research opportunity and express my sincere gratitude to everyone who has been a part of it. Much appreciation goes to all my friends and colleagues at the University of Cape Town. Most importantly, thank you to my supervisor, Nico Fischer, for all your incredible input and encouragement, your constant motivation, welcoming open door policy and immense patience. Many thanks to my co-supervisor, Michael Claeys, for giving me this opportunity. A special mention goes to Hennie, thank you for aiding me through my transition from an organic chemist into the field of heterogeneous catalysis.

My gratitude goes to those who have aided with experimentation in addition to the friendly faces around my labs: Stephanie, Zulfa and the team at the Analytical Laboratory, Joe from the Mechanical Workshop, Mohamed from the UCT Imaging Centre, the staff at UWC Electron Microscope Unit, my close colleague Thulani and the staff at Cardiff University for help with XPS, Shepherd, Leah and Greg from the Organometallic Research Group for use of their glove box, Sharon and company from CeBER for use of their centrifuge as well as Penny and Soraya from Materials Science for the use of their TGA. Thank you also to our administration staff, cleaning staff, academic staff as well as the technical staff, particularly Gideon, Chantal, Rachel, Marc and Waldo.

I would like to acknowledge the National Research Foundation (NRF) and the DST/NRF Centre of Excellence in Catalysis Research (c*change) for financial support without which I could not have done this.

Thank you to my research group, you have made this a comfortable and nurturing environment which I have enjoyed being a part of. A deep appreciation goes to my family and friends for their constant love and support.

And finally, mum and dad, this degree is as much yours as it is mine, well done.

DECLARATION

I know the meaning of plagiarism and declare that all the work in the document, save for that which is properly acknowledged, is my own. This thesis/dissertation has been submitted to the Turnitin module and I confirm that my supervisor has seen my report and any concerns revealed by such have been resolved with my supervisor.

Signed by candidate

Muhammad Motala

December 2017

Table of Contents

LIST OF ABBREVIATIONS AND SYMBOLS

$[Ca_{24}Al_{28}O_{64}]^{4+}(4e^-)$ - electride	C12A7:e^-
$12CaO{\cdot}7Al_2O_3$ - mayenite	C12A7
Adsorbed atom	Adatom
Anderson-Schulz-Flory	ASF
Arbitrary units	a.u.
Atomic absorption spectroscopy	AAS
Bet surface area	S_{BET}
Binding energy	BE
Brunauer-Emmett-Teller	BET
Cage conduction band	CCB
Chain growth probability	**α**
Circulating fluidised-bed reactor	CFB
Degree of reduction	DOR
Differential scanning calorimetry	DSC
Diffuse reflectance spectroscopy	DRS
Electron energy loss spectroscopy	EELS
Energy-dispersive spectroscopy	EDS
Fischer-Tropsch	FT
Fischer-Tropsch synthesis	FTS
Flame ionisation detector	FID
Four-way valve	4WV
Full width half maximum	FWHM
Gas chromatograph(y)	GC
Gas chromatograph(y) – flame ionisation detector	GC-FID
Gas chromatograph(y) – thermal conductivity detector	GC-TCD
Gas-to-liquids	GTL
High temperature Fischer-Tropsch	HTFT
Hüttig temperature	$T_{Hüttig}$
Hydrothermally produced C12A7:e^-	HT-C12A7:e^-
Inductively-coupled plasma optical emission spectrometry	ICP-OES

Infrared	IR
Intrinsic work function	ϕ_{WF}
Iron(III) acetylacetonate/ferric acetylacetonate	$Fe(acac)_3$
Liquefied natural gas	LNG
Low temperature Fischer-Tropsch	LTFT
Mass flow controller	MFC
Mass spectrometry	MS
Melting point temperature	T_m
Needle valve	NV
Normal temperature and pressure	NTP
Olefins/paraffins (ratio)	O/P
Photoelectron yield spectroscopy	PYS
Pressure regulator	PR
Sasol advanced synthol	SAS
Secondary ion mass spectroscopy	SIMS
Shell middle distillate synthesis	SMDS
Slurry bed reactor	SBR
Solid-phase produced C12A7:e^-	SP-C12A7:e^-
South Africa synthetic oil liquid	Sasol
Superconducting transition	T_c
Standard temperature and pressure	STP
Synthesis gas	Syngas
Tamman temperature	T_{Tamman}
Thermal conductivity detector	TCD
Thermogravimetric analysis	TGA
Time-on-stream	TOS
Transmission electron microscopy	TEM
Tubular fixed bed reactor	TFBR
Ultraviolet	UV
Ultraviolet photoelectron spectroscopy	UPS
Water gas shift	WGS
X-ray powder diffraction	XRD

LIST OF FIGURES

LIST OF TABLES

SYNOPSIS

Iron-based Fischer-Tropsch (FT) technology is well established in the industrial production of hydrocarbon resources. The use of a stable inorganic electride as a support system, with potential promoter effects which could replace commonly used alkali metals, may have the potential to open a new facet within the research and development of iron-based FT technology.

The hydrothermally produced $[Ca_{24}Al_{28}O_{64}]^{4+}(e^-)_4$ electride material as carrier for Ru nanoparticles for the synthesis of ammonia from its elements has been reported in literature as support system and substitute to conventional alkali promotion.[1] This is due to highly localized electrons present in the crystallographic cages of the material that may serve as a Lewis base and facilitate bond breaking of feedstock molecules adsorbed to the catalytic active sites. The hydrothermal preparation of this electride previously resulted in a surface area of up to 50 $m^2 \cdot g^{-1}$ and a two-fold rate increase in ammonia production.[2] The low work function of $[Ca_{24}Al_{28}O_{64}]^{4+}(e^-)_4$ is comparable to that of potassium, therefore the iron loading onto the electride is postulated to mimic the promoting effects of potassium(oxide) in the FT synthesis.

Following the hydrothermal synthesis of the electride produced at varying evacuation temperatures (800 °C and 1000 °C), supported iron catalysts were prepared using a stoichiometric amount of $Fe(acac)_3$ precursor to decompose as iron oxide onto the novel support. Iron supported on the unreduced mayenite precursor, $[Ca_{24}Al_{28}O_{64}]^{4+}(O^{2-})_2$, and unpromoted precipitated iron diluted in **γ**-alumina were used as control/baseline catalysts. The testing of these catalysts was conducted at 240 °C and 15 bar with a 2:1 H_2/CO ratio.

The electride and mayenite catalysts performed similarly with regards to hydrocarbon selectivities with the precipitated iron bulk catalyst. However, significantly larger CO_2 selectivity and olefin/paraffin ratios were observed for the supported catalysts showing little difference between the electride and its unreduced counterpart.

1 INTRODUCTION

Fuel and petrochemical resources are some of the most demanding yet highly controversial commodities within the global socioeconomic scale. Although there are developments to reduce the reliance on fossil fuels, these finite resources continue to dominate the large-scale chemical industry.

Interest in the Fischer-Tropsch (FT) process continues to be high over the past few decades due to its potential as an alternate pathway to liquid fuels from a diverse carbon base feed stock amid global fluctuations in the supply and demand of crude oil and as a synthesis process for commodity and fine chemicals.[3] The FT process can be summarized as the conversion of synthesis gas (syngas), a mixture of hydrogen and carbon monoxide, to hydrocarbon based products.[4]

Although the use of FT to produce fuel is applied on an industrial scale, there has been increasing interest in using the FT process to produce other chemicals for their commercial value.[5] One of the reasons for extensive interest in FT technology is due to the variety of products available through downstream refinement of the hydrocarbon stream. This has also lead to the combination of Fischer-Tropsch synthesis (FTS) with downstream processes such as hydroformylation in the production of aldehydes which can in turn be hydrogenated to alcohols. A wide range of products such as polymers, alcohols and surfactants are produced.[6]

Due to the industrial significance of the process, research on improving the FT process is continuous and a large focus is placed on increasing catalytic efficiency, stability, decreasing costs as well as the rate of catalytic deactivation.[7] Industrial gain can particularly be increased from the study of the interaction of feedstock species with the catalytic active sites in maximising yields.

Iron-based FTS plays a major role in industrial FT plants, particularly in the production of high octane gasoline (which is produced primarily from Fe FTS with coal based feedstock).[8] Coal derived syngas, important in the South African context but even more so in the fast growing market of China, produces a higher total hydrocarbon product spectrum with lighter more paraffinic hydrocarbon products than natural gas-derived syngas.[8] However, for maximum effect of these Fe based catalysts, promotion by alkali metal oxides, especially potassium, are required for enhanced activity. Alkali promotion alters the catalyst acidity, therefore improving its rate of association and dissociation of the feedstock.[9]

The compound $[Ca_{24}Al_{28}O_{64}]^{4+}(4e^-)$ (C12A7:e^-) was identified as a stable solid electride, a material which has electrons within its crystallographic cages that act as anions. The mobility of these electrons creates a strong Lewis base character, i.e. a low work function, which in turn could be used instead of alkali promotion. Omission of alkali promotion may allow for a more efficient FTS if disadvantages of alkali promotion such as increased deactivation rates and mobility of the promoter species under reaction conditions are reduced or eliminated.

The success of the electride as a support for ammonia synthesis with Ru-based catalysts has created interest for its use in other fields[1]. Once tried and tested for the FTS with an iron-based system, other catalytic reactions which benefit from increased electron availability could be investigated; these may include the production of methanol from syngas[10,11], decomposition of nitrous oxides[12,13], fuel processing[14] and fuel cell[15] applications.

2 LITERATURE REVIEW

2.1 Fischer-Tropsch process

2.1.1 History and development

The term Fischer-Tropsch was devised after Franz Fischer and Hans Tropsch, of the Kaiser Wilhelm Institute for Coal Research in Mülheim an der Ruhr (Germany), reported the synthesis of hydrocarbons from synthesis gas over a rapidly deactivating Fe catalyst in 1924.[3,16] During World War II, the FT process was extensively developed due to increased fuel demands, abundance of coal supply and lack of crude oil reserves in Germany.[5,16] During this time, there were a total of nine FT plants in operation which produced a combined capacity of 660 thousand tons of hydrocarbon product per year.[5] Although commercialisation rapidly grew, the discovery of massive crude oil fields in the Middle East lowered the price of crude derived liquid fuels, in turn reducing interest and investment in FTS. However, with an anticipated increase of crude oil prices in the 1950s and amid increasing sanctions on South Africa during the political and economic isolation of the apartheid era, a coal-based FT plant was built in Sasolburg. South Africa Synthetic Oil Liquid (Sasol) further commissioned another two plants in Secunda in the early 1980s following the crude oil crisis of the 1970s, at a time when crude oil was priced above $30 per barrel, successfully increasing their product capacity to about 6 million tons per year.[5]

Petroleum crude oil is currently the major source of the world's fuel and chemical production but an increase towards fuel from syngas produced from more abundant coal and methane/shale gas is projected as the oil reserves are depleted.[5] Recently, the possibility of a more sustainable bio-mass derived syngas, with successful hydrocarbon production, has been investigated.[17]

The thermodynamically preferred paraffin product of the FT process is methane, however the nature of the catalyst allows for the synthesis of higher

chain length compounds and is even capable of producing solid waxes stable at ambient conditions.[3]

2.1.2 FT reactions

In industry, three steps are followed in the production of hydrocarbons via the FTS; first syngas is prepared followed by the FT process itself and finally the upgrading of the obtained product stream to the desired slate. At Sasol, syngas was primarily prepared from the gasification of coal, due to its availability within South Africa, however more recently with the discovery of a large conventional natural gas field in Mozambique and in the Gulf, methane steam reforming became dominating.[3,18,19] It is envisaged that the continuing rise of shale gas will have an impact on FTS, both as a new and cheap feedstock and, possibly more importantly, also as competition due to the resulting increase in crude oil price.[20]

The FT reaction can be described as surface polymerisation of CO under a hydrogenating atmosphere[21] and the reaction can be simplified to Equation 2-1.

FT **Equation 2-1**

$$(2n+1)H_2 + nCO \rightarrow C_nH_{(2n+2)} + nH_2O$$

$\Delta H_{R,513K}$ = -153.7 kJ·mol^{-1}

On certain FT active materials, such as iron, the water gas shift (WGS) reaction is also supported (see Equation 2-2). The conversion of CO with water forming carbon dioxide and hydrogen changes the composition of syngas.[22,23] This allows for the utilisation of synthesis gas streams which are lean in hydrogen and do not adhere to a 2:1 ratio of H_2/CO as indicated in Equation 2-1.

WGS **Equation 2-2**

$$H_2O + CO \rightleftharpoons CO_2 + H_2$$

$\Delta H_{R,513K}$ = -39.7 kJ·mol^{-1}

A third reaction, the Boudouard reaction (Equation 2-3) is sometimes reported under FT conditions and converts CO feedstock into CO_2 and carbon deposits.[24] This carbon formation may lead to blocking of active sites and disintegration of catalyst particles[25] (see catalyst deactivation in section 2.4).

Boudouard **Equation 2-3**

$$2CO \rightarrow CO_2 + C$$

$$\Delta H_{R,513K} = -172.9 \text{ kJ} \cdot \text{mol}^{-1}$$

2.1.3 FT mechanisms

Fischer-Tropsch is commonly described as a surface polymerisation reaction which involves adsorption of reactant species onto the catalyst surface, an initiation step to form a chain starter, a propagation step promoting chain growth and a termination step comprising the desorption of product species (see section 2.1.4 for additional detail).[26] The hydrogen and carbon monoxide feedstock provide rise to a large amount of surface species and reaction intermediates on the catalyst surface with various reaction pathways proposed in literature.[27,28]

In terms of stoichiometry, water is a major product of the FTS. Potassium promoted Fe catalysts (see section 2.1.6) are known to be inhibited by the presence of water unlike Co catalysts.[29] A study showed a decrease in catalytic activity during addition of water vapour to dry syngas feed over iron catalysts which is almost completely reversible.[30] The WGS shift however does occur rapidly at higher temperatures on Fe FT catalysts reaching equilibrium.

CO_2 is a major by-product during Fe catalysis of FT, with the WGS reaction close to equilibrium under high temperatures (see section 2.1.7 for reaction conditions). At low temperatures, there is a lower amount of CO_2 present in the system than stoichiometrically predicted by the WGS reaction equilibrium due to secondary reactions involving H_2, CO, CO_2 and H_2O.[27,31] On cobalt catalysts, the formation of CO_2 is usually much less pronounced.

The scientific literature that follows, discusses four major FT reaction mechanisms, namely: the alkyl (derived from the carbide) mechanism, the alkenyl mechanism, the enol mechanism and the CO-insertion mechanism. The species referred to in the description of the mechanisms below are summarized in Figure 2-1.[28]

2.1.3.1 Alkyl mechanism

The alkyl mechanism[32,33] is the most established pathway for straight chain hydrocarbon synthesis in FT. Dissociative CO-chemisorption is said to generate surface carbon (3) and surface oxygen (19); the latter is hydrogenated by adsorbed hydrogen (20) to form water, a major product of the FTS or reacts with adsorbed CO to form CO_2. The surface carbon is consecutively hydrogenated to form adsorbed methylidyne (4), methylene (5) and surface methyl (6), the latter being identified as the chain starter and the methylene species is regarded as a monomer. Propagation and chain growth is believed to take place by successive addition of the monomer onto the surface alkyl species. **β**-Hydrogen abstraction or hydrogen addition to the primary C terminates chain growth and yields **α**-olefins and n-paraffins, the main product classes observed experimentally.

The surface species involved in this pathway have been identified using techniques such as secondary ion mass spectroscopy (SIMS)[34], infrared (IR) spectroscopy[35] and electron energy loss spectroscopy (EELS).[36] The alkyl mechanism was developed from the carbide mechanism, originally thought to proceed via the formation of metal carbides, followed by hydrogenation thereof and polymerisation. However, this was rejected because stable carbides which are far more commonly formed by iron-based catalysts than any other FT catalyst were experimentally determined to contribute little to the product stream.[37] The alkyl mechanism does not generally describe the formation of branched species and oxygenates which are thought to occur from parallel pathways.[27]

2.1.3.2 Alkenyl mechanism

The alkenyl mechanism proposed by Maitlis *et al*.[38] is an alternative pathway suggesting a route for the formation of **α**-olefins as primary product in the FTS. The chain starter for this route is a vinyl species ($HC=CH_2$) (11) formed from the coupling of methylidyne (4) and methylene (5) surface groups which are formed analogous to the alkyl mechanism. Chain growth occurs via the addition of a methylene monomer to the vinyl species to form a surface allyl species (12). Alkenyl (13) species are further produced from isomerisation of the allyl-vinyl species. Some of these species react with surface methylene to form branched products. Termination of this pathway comprises of the hydrogenation of the alkenyl species to form **α**-olefins.[27] However, this mechanism does not yield n-paraffins as primary product enforcing the presence of parallel reaction pathways or significant secondary reactions (see section 2.1.4).

2.1.3.3 Enol mechanism

The enol mechanism proposed by Storch *et al.*[39] is an alternative reaction pathway to explain the synthesis of oxygenates from an oxygenated (enol) surface intermediate. The chain initiator and primary monomer is an enol species (14) formed from the hydrogenation of chemisorbed CO (1). Chain propagation occurs from the condensation reaction of two enol species (14) with the elimination of water to desorb aldehydes, alcohols and **α**-olefins. Branched hydrocarbons are believed to form from the contribution of CHROH surface species (15), produced from the hydrogenation of the enol monomer (14). Secondary reactions that are believed to occur include the hydrogenation of **α**-olefins to n-paraffins, Cannizzaro reactions of primary aldehydes to form carboxylic acids and the reaction of these acids with alcohols to form esters[27,40,41] (see section 2.1.4).

2.1.3.4 CO-insertion mechanism

The CO-insertion mechanism, developed by Pichler and Schulz[42] involves CO surface species as a monomer (1) and chemisorbed methyl as the chain starter (as described in the alkyl mechanism). Chain propagation occurs to form a surface acyl species (8) by a CO-insertion (as seen in coordination chemistry complexes[35]) between the metal and alkyl surface species (7). Following hydrogenation and elimination of oxygen, long chain hydrocarbons are produced (10). Desorption to form n-paraffins and **α**-olefins can be analogous to the alkyl mechanism (**β**-hydrogen elimination).[28] However, an alternate route of chain termination, which is considered a predominant route to the formation of aldehydes and alcohols is the hydrogen addition to the acyl surface species (8) and (9).[27]

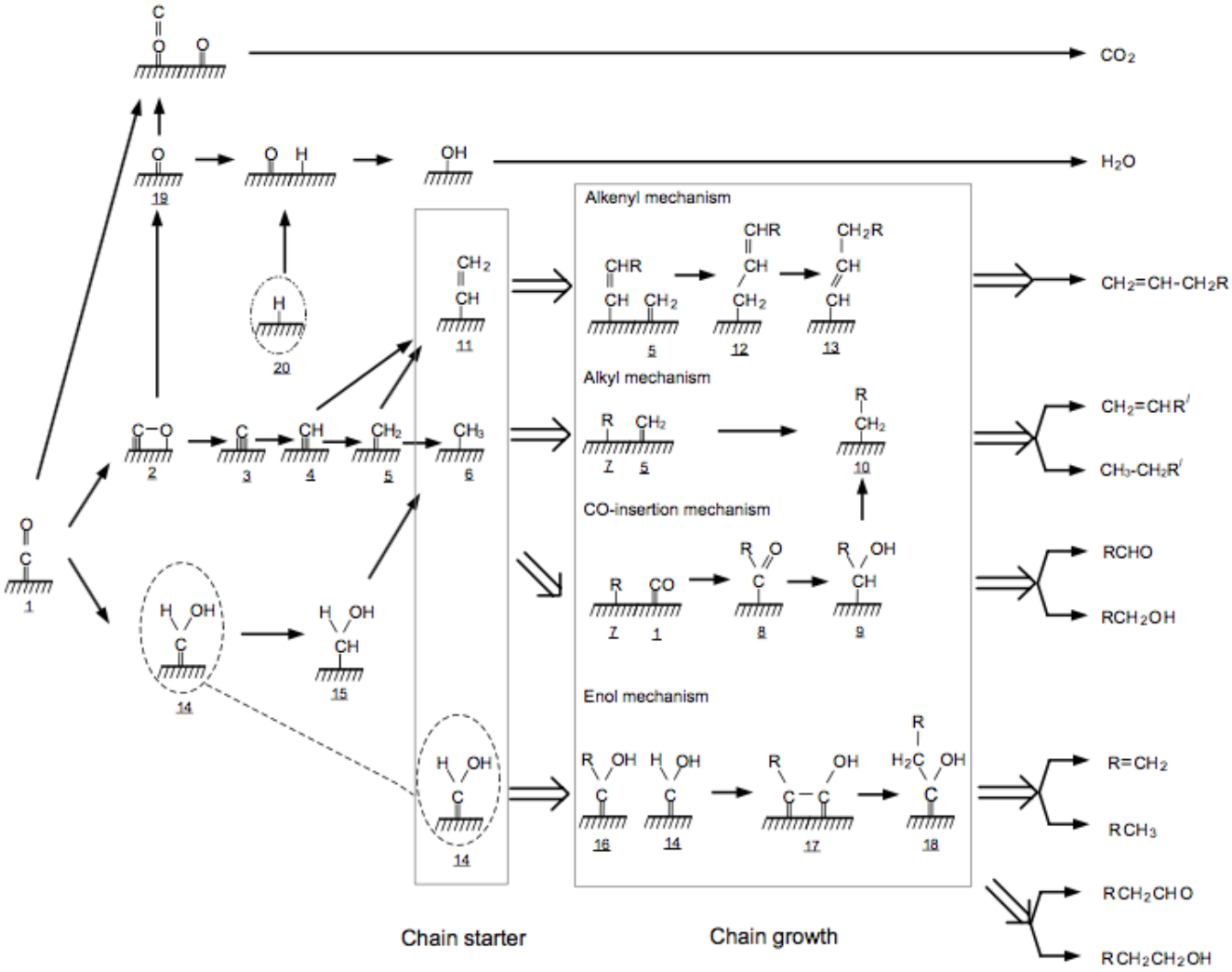

Figure 2-1 Overview of the FT mechanistic pathways and its intermediates. (From Mabaso).[28]

2.1.4 FT product formation

The FT process produces a wide variety of hydrocarbon and oxygenate products. Due to its underlying polymerisation type mechanism, no single compound (besides the undesirable methane) can be synthesised selectively, however, yields can be increased by applying subsequent product workups and downstream processes.[26,27] The primary products of FTS are generally straight chain terminal olefins and straight chain paraffins.[43,44]

As FT is a polymerisation reaction, at each step during formation, the hydrocarbon surface species has the option to desorb forming a primary FT product or to continue to grow in chain length (illustrated in Figure 2-2). Activity of a FTS catalyst is generally determined from its conversion of CO to hydrocarbon products.

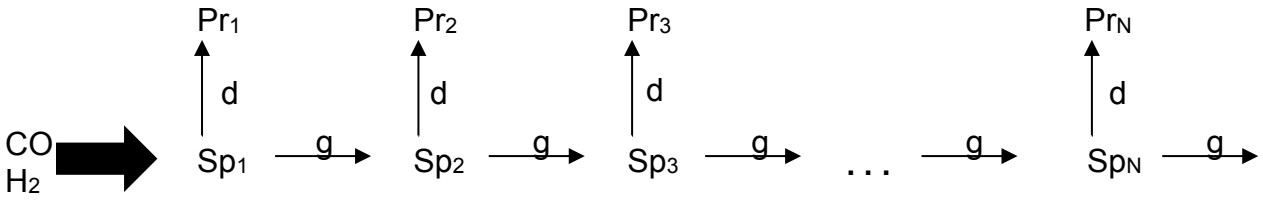

Figure 2-2 Scheme showing the kinetics of ideal chain growth (g) and product desorption (d). Sp_N is the chemisorped surface species and Pr_N is the product species for carbon number N. (Adapted from Claeys and van Steen).[27]

Secondary products can be formed via the re-adsorption of primary products and subsequent reactions such as the hydrogenation of α-olefins to n-paraffins, the re-insertion into a growing chain potentially forming branched products and oxygenates, as well as isomerisation, double bond shift and cracking of long chain hydrocarbons.[26,27,41,43,45] The kinetics of polymerisation are similarly consecutive to the primary products (illustrated in Figure 2-3).

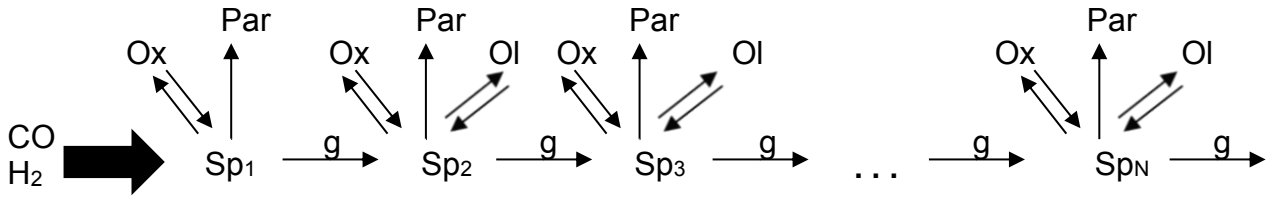

Figure 2-3 Scheme showing the kinetics of ideal chain growth (g) with paraffins (Par), olefins (Ol) and oxygenates (Ox) as desorbed product species. Sp_N is the chemisorbed surface species of a carbon number N. (Adapted from Claeys and van Steen).[27]

The probability of continuation of the hydrocarbon chain growth is described by **α**, the chain growth probability (Equation 2-4).[46]

Equation 2-4

$$\alpha_n = \frac{r_{g,n}}{r_{g,n} + r_{d,n}}$$

where:

n = Carbon number

α = Probability of chain growth

r_g = Rate of chain growth

r_d = Rate of product desorption

The chain growth probability has a direct effect on the selectivity of the reaction. The kinetics of product formation in FTS can in part be explained by the Anderson-Shulz-Flory (ASF) model; a mathematical expression of the weight content of products of a certain carbon number (W_N) as a function of carbon number (N_C).[47,48] The 'ASF plot' of the logarithmic molar fraction as a function of carbon number gives a linear relationship (Equation 2-5). Therefore, the average chain growth probability may be determined from the inverse logarithm of the gradient of the 'ASF plot' (Equation 2-5).

Equation 2-5

$$\log\frac{W_N}{N_C} = N_C \log\alpha + \log\frac{1-\alpha}{\alpha}$$

where:

W_N = Mass fraction

N_C = Carbon number

α = Probability of chain growth

Under the assumption of ideal ASF kinetics, a theoretical hydrocarbon product distribution can be modelled as a function of chain growth probability (**α**) (see Figure 2-4). The product distribution is divided into fractions: C_1 (methane), C_{2-4} (gaseous hydrocarbons), C_{5-11} (gasoline), C_{12-18} (middle distillate/diesel) and C_{19+} (waxes).[28] This product distribution shows directly the selectivity problem of the FTS. No product slate, but methane, can be synthesised in concentrations above 50 – 60 wt. % requiring extensive downstream processes.

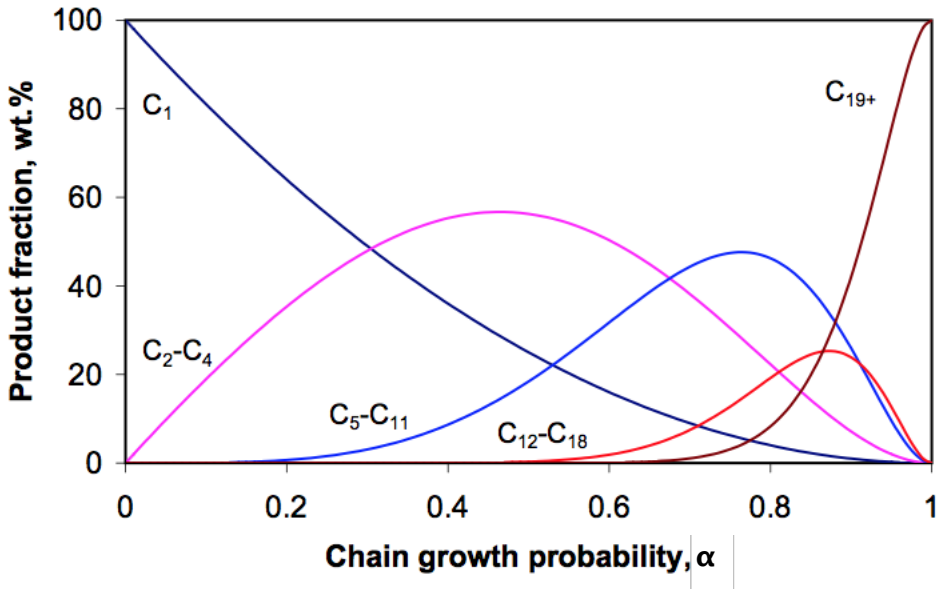

Figure 2-4 Theoretical product distribution of FTS products as a function of chain growth probability (α) under the assumption of ideal ASF kinetics. (Adapted from Mabaso and de Smit).[28,49]

The value of the chain growth probability is mainly based on process conditions. The main factors that affect this are the catalyst type, temperature and the feed gas compositions. Methane formation, which can be synthesised with a 100% selectivity when the **α** value is zero, is said to increase with increasing temperature and H_2/CO ratio.[50] Longer chain growths are usually found at lower temperatures (see section 2.1.7).[27] Potassium promotion (see section 2.1.6) and high pressures with iron-based catalysts are said to increase chain growth[47] as well as olefin and oxygenate selectivity. This is largely due to

decreased secondary reactions of these reactive products as re-adsorption to the active sites is reduced.[51]

2.1.5 FT catalysts

A variety of heterogeneous catalysts can be used in the FT process, each with varying advantages and disadvantages. The industrial catalysts fall under one of three classes: carrier free catalysts which is purely catalytic compound, coated catalysts[52,53] consisting of a fine layer of active substance coating an inert material and supported catalysts comprising of a dispersion of catalytically active substance on a usually inert material with a higher surface area.[54]

On a research scale, catalysis containing Fe, Co, Ni, Re, Mo, W along with the platinum group noble metals have been studied.[6,21,55–62] The most active of these are Fe, Co, Ni, Ru and Os, with Re and Rh described as moderately active[21]. Ruthenium is the most active of the FT catalysts but is considered very costly compared to Fe and Co.[26] Nickel is considered industrially unsuitable due to its high methane selectivity which is in turn due to its high hydrogenation activity.[6] Global Ru, Os and Rh reserves are low rendering them commercially challenging.

Iron- and cobalt-based catalysts are the only ones used industrially and can be categorized into three main classes: fused iron catalysts, precipitated iron catalysts and supported cobalt catalysts (see section 2.3).[3] Iron may be operated at one of three temperature ranges known as high temperature FT (HTFT) or low temperature FT (LTFT) with medium temperature FT (MTFT) recently emerging[63], while cobalt-based catalysts are generally operated under LTFT conditions (see section 2.1.7).[20]

Active iron-based catalysts form a mixture of different phases under reaction conditions with ongoing debate and speculation on the exact nature of the active centre.[64] Iron carbides, are thought to be the most active of iron phases; they form via carburisation of the oxide precursor or after reduction of the latter

to metallic iron (α-Fe). Hägg carbide (χ-Fe_5C_2) is considered the most active iron species.[41,65] Literature suggests the re-oxidation of carbide to magnetite (Fe_3O_4)[66] to be one deactivation mechanism, despite experimental evidence suggesting it as an active phase of iron in FTS,[67,68] in addition to the WGS reaction.[27,69] Under reaction conditions a metastable phase mixture of carbides, oxides and metallic iron species forms. Cobalt-based catalysts are active in their metallic phase and considered inactive when oxidised.[70]

Catalyst support materials are usually used to maximize surface area and avoid transport limitations in the catalyst grain, and are generally regarded as inert. The most common catalytic supports are activated carbons, zeolites and metal oxides such as alumina and silica.[71] FTS has been reported with metals loaded onto a number of different support materials including carbon nanotubes[72], carbon nanofibers[73] as well as many metal oxides.[74] To date, no FTS has been reported on any electride compounds (see section 2.2).

2.1.6 Promotion of iron FT catalysts

Alkali promotion is used to enhance the selectivity and activity of fused and precipitated iron catalysts and has a significant chemical effect on these catalysts.[3] Potassium promotion has been shown to increase FTS and WGS activity as well as α-olefin and long chain hydrocarbon selectivity.[75] Although frequent in FTS, this is not a FT specific promoter but is commonly used in other industrial processes such as the Haber-Bosch process[76], the synthesis of higher alcohols over Cu-based catalysts[77], dry reforming of CO_2 over Mo-Ni catalysts[78], soot oxidation in catalytic converters (Fe and Mn spinels) for diesel engines[79] and the decomposition of NO_x[12] and N_2O[13] using an Ag(III) and a Co catalyst respectively.

Adsorbed alkali ions (usually potassium ions) on the iron surface decrease the overall work function; therefore, the adsorption energy of CO (in the FTS) is increased and the strength of the carbon-oxygen bond is decreased.[80] A larger amount of adsorbed CO is subsequently dissociated and does not desorb. The

dissociation of hydrogen and its mobility may be restricted or suppressed to some extent by the alkali metal.[81] This affects the overall C:H ratio on the catalyst's surface and therefore directly affects the selectivity.

The FT reaction and other alkali promoted reactions display an optimum level of promotion; this needs to be high enough to achieve a low methane selectivity but low enough so that the catalyst does not begin to deactivate as active metal sites are covered by alkali atoms (see catalyst deactivation in section 2.4).[9] Alkali promotion may also increase undesirable effects such as an increased rate of carbon formation (known as coking discussed in section 2.4.2) and an increase of organic acids in the hydrocarbon products. These acids may cause corrosion during downstream refining.[3] Additional compounds within the final catalyst system may or may not influence the overall activity, however the basicity of alkali promoters may be decreased due to the formation of compounds such as alkali-silicates or alkali-aluminates produced from the reaction of the promoters with less basic silica supports or acidic alumina supports.[82] The promoter concentrations in industrial iron-based catalysis are therefore optimised for the chemical nature and surface areas of the total components of the catalyst.[82]

Contrasting from iron-based catalysts, cobalt-based catalysts are generally active without the requirements of promoters.[3] Early cobalt FTS studies showed that alkali (potassium) promotion of cobalt at atmospheric pressure increased the selectivity of waxes, however at higher pressures, which are necessary at industrial scale, these catalysts were insensitive to alkali metals.[82,83]

The use of copper as a promoter of precipitated iron catalysts in addition to alkali promotion during hydrogen activation is common to facilitate reduction of iron oxide to metallic iron as well as to minimize deactivation by sintering of the catalyst.[84] The temperature of reduction of iron(III) oxide to metallic iron was shown by O'Brien *et al*. to be dependent on the level of copper promotion.[84] Copper promotion is expected to occur via the reduction of copper oxide to its metallic state which accelerates the reduction of iron oxide due to its higher hydrogen dissociation potential and a spill over mechanism.[84]

Structural promoters may be present in a catalyst as fine particles to prevent sintering (see section 2.4) and improve their mechanical properties.[85,86]

2.1.7 FT reaction conditions

Temperature is one of the main influencing parameters in the FT process, with an increase in temperature favouring increased methane formation and a reduction in average hydrocarbon chain length.[20,21] The HTFT process operates at about 300 – 350 °C and is used to produce gasoline and linear low molecular weight alkenes as well as chemicals with iron-based catalysts, while the LTFT process operates at about 200 – 240 °C to produce high molecular weight linear waxes. In comparison to cobalt-based catalysts which would predominantly form methane at HTFT conditions, iron-based catalysts are employed in both temperature regimes. With the LTFT synthesis, a relatively high H_2/CO ratio of 1.7 is usually fed into the reactor; while with the HTFT synthesis, the WGS reaction (Equation 2-2) is rapidly reaching equilibrium allowing for significantly lower H_2 content in the feed gas and even supporting the activation of CO_2.[5] A ratio of 1.05 for $H_2/(2CO + 3CO_2)$ can theoretically convert all syngas to FT hydrocarbons.[5,82]

Recent success by Synfuels China in utilising abundant coal reserves in China to produce clean fuels using a novel MTFT process has garnered further development in the technology.[63] Operation of this process occurs with iron-based catalysts in slurry-phase reactors at 270 – 300 °C and produces a similar product spectrum to LTFT. The higher temperature compared to LTFT allows for a better recovery of heat produced from the FTS for steam production and an easier removal of heat from the reactor.[87]

Iron-based catalysts under HTFT conditions in fluidised fixed bed reactors (see section 2.1.8) are common for maximisation of gasoline production (*ca.* 40% low octane value straight run gasoline).[5] Other high yielding products such as propene and butene can be oligomerised to gasoline via secondary reactions;

these oligomers are highly branched and therefore have a favourably high octane rating. The octane value of gasoline can be enhanced by addition of di-isopropyl ether, produced from propene and water.

Petrochemicals are more economically valuable than fuels and many of which are olefin rich. FTS under HTFS conditions is also utilized to produce linear **α**-olefins.[5] Various olefins are fractioned and used to generate further useful polymers (e.g. ethylene and propylene are polymerised to polyethylene or polyvinylchloride, and polypropylene or acrylonitrile respectively). Linear alcohols can be produced by hydroformylation of long chain olefins. LTFT can be used to produce long chain linear paraffins; linear oils and waxes can acquire great profits.[5]

Contrary to gasoline production, cobalt-based processes are controlled to maximise wax production in high capacity slurry or fixed bed reactors which is subsequently cracked to produce diesel fuel.[4,5,88] Diesel quality favours a high cetane value (high linearity and low aromatic content), factors that lower the quality of gasoline. Hydrotreatment of straight run diesel (*ca.* 20% selectivity) has a cetane value of about 75, greater than the market necessary cetane value of 45.[5] Further high quality diesel can be produced from mild hydrocracking of larger products accounting for about 45-50% selectivity. The final cetane number of diesel fuel produced from FTS is about 70, which can be used to enhance lower quality diesel fuel.[5,29]

2.1.8 FT reactors

Industrial scale FTS is conducted in four types of reactors: the circulating fluidised-bed reactor, fluidised-bed reactor, tubular fixed bed reactor and slurry phase reactor.[89] The fluidised-bed reactors operate for HTFT synthesis in a two-phase system (solid and gas) and in a three-phase system (solid, liquid and gas) for LTFT synthesis; whilst the fixed bed reactors and slurry phase reactors are employed for LTFT, often in three-phase.[89] A distinguishing fact between HTFT and LTFT is that HTFT reactors do not have a liquid phase

outside the catalyst particles which could lead to agglomeration of particles which in turn could cause loss of fluidisation.[89,90] Due to the high exothermic nature of the FT process, constant removal of heat from the system needs to occur to minimise catalyst deactivation[91] (see section 2.4).

Following World War II, several companies in Germany explored LTFT reactors, with a focus on the cooling systems. These were generally fixed bed reactors adopting either internal, external by gas or liquid or direct cooling by feed or fresh syngas under medium pressure processes.[92] Initial Arge tubular fixed bed reactors (TFBR) also used by Sasol from 1955 to 1993 consist of approximately 2000 tubes with steam acting as cooling medium and were operated at about 220 °C and 25 bar.[29] The development of the Shell Middle Distillate Synthesis (SMDS) by Shell in 1973 with fixed bed multitubular reactors and cobalt catalysts allowed for the production of middle distillate fuels (gasoline and kerosene) via an advanced synthesis that manipulates the feedstock ratio to achieve the desired selectivity, and is still used today.[93] However, although reliable, ongoing improvement has taken place to improve the pressure drop, utilization of the catalyst and heat removal.[94] In 1993 Sasol commercialized slurry bed reactors (SBR)[95] with internal heat exchangers for the LTFT previously predominantly conducted in fixed beds.[96]

Modern day SBRs include ebullating bed reactors and slurry bubble columns. Slurry reactors are used to produce large amounts of wax which is subsequently cracked to diesel and naphtha fractions.[3] The naphtha slate is then largely used as a feedstock for thermal cracking to produce ethylene and other products. Major drawbacks of slurry reactors is the scale-up of catalysts due to its large gas throughput which requires large diameter reactors, extensive heat removal process via inserted cooling tubes and the difficulty of separating suspended catalysts from liquid products.[92,97]

Fluidised-bed reactors cannot be used to maximise products heavier than gasoline/naphtha as they operate on the lower end of the feasible temperature range.[89,98] At higher temperatures, these fluidised-bed reactors are subject to unwarranted carbon formation. One of two common HTFT reactors used by

Sasol is the circulating fluidised-bed reactors (CFB), a complex circulating fluidised-bed reactor used for the Synthol process which uses fused Fe catalysts operated 25 bar and 340 °C.[99,100] The other more recent fluidised-bed reactor operates the Sasol Advanced Synthol (SAS) process at 20– 40 bar and 340 °C.[100] The major advantage of the SAS reactor over the CFB is that the catalyst/gas ratio in the reaction zone is about two-fold higher for the SAS reactor which improves its relative conversion performance.[100] Other advantages of the SAS reactor include its higher energy efficient design, ability to produce more high pressure steam and cost effective scale-up of its support structure.[100]

2.2 What is an electride?

An inorganic electride is a crystalline salt in which electrons serve as anions.[101] The electrons are trapped in crystallographic cages of the material. These highly localised electrons can migrate to neighbouring cages and be seen as the smallest entities having anionic properties. They serve as strong reducing agents.[102] The three-dimensional inorganic electride C12A7:e^- (see section 2.2.1) is the first reported stable inorganic electride at room temperature; however, two pure zeolites containing caesium in their pores, ITQ-4 and ITQ-7 were previously reported to have thermally stable electride properties with a cation-to-electron ratio of 1:1.[102,103] The structure of the crystal, in conjunction with the size and length of interconnected anion channels influence the mobility of the trapped electrons within inorganic electrides.[104] Although electride electrons act as the simplest anions, their quantum nature and small mass allow them to demonstrate unusual and complex interactions with each other and the cations.[104,105]

2.2.1 Development of C12A7 and C12A7e^-

The mayenite structured material referred to as C12A7 was first reported by Hentschel in 1964 at the Eifel volcanic complex in Germany and named after the birthplace of its discovery, Mayen, Germany.[106] The elements involved in

the composition of mayenite are among the most abundant in the earth's crust.[107] C12A7 is stoichiometrically represented as $C_{12}A_{14}O_{33}$ and is a combination of $CaO\text{-}Al_2O_3$ ($12CaO\cdot 7Al_2O_3$), a constituent of aluminous cement; however, it exhibits different physical and chemical properties to the rest of its family. These include the ability to form a glass phase, fast oxygen-ion conductivity (the mobility of O^{2-}) and a volume expansion of about 10% when crystallized from a melt.[108] The crystal structure of C12A7 of mayenite-type construction has a chemical formula for the unit cell described as $[Ca_{24}Al_{28}O_{64}]^{4+}(O^{2-})_2$ in its fully oxidised state.[109] The "free oxygen ions" (O^{2-}) are localised within two cages of the positively charged framework (12 cages) of a body centred cubic (*I*43*d*) lattice structure.[107] The occupied cages can be replaced with other anions whilst the remaining 10 cages are empty.[105] The diameter of the oxide ions is about 0.25 nm in comparison to the free space of the cage of *ca.* 0.4 nm which allows the oxide ions to loosely bind to the 6 calcium cations inducing a sense of freedom to the oxides. These free oxygen ions can be removed by reduction or knock-on processes by energetic ions.[109] The mayenite can be electrically conducting following hydrogenation which substitutes the oxide ions with hydride ions. Subsequent exposure to ultraviolet (UV) light can dissociate electrons from these hydrides.[107]

In a study by Yang and co-workers, the partial oxidation of methane into syngas was explored over C12A7 (prepared by a solid-state reaction of $CaCO_3$ and **γ**-alumina) and promoted by Ni, Co, Pt, Pd and Ru.[110] A particular investigation was done on the effect of space velocities and metal loadings as well as catalytic activity of Ni/C12A7 compared to Ni supported on CaO and **α**-alumina and other calcium aluminates.[110] It was observed that the Ni/C12A7 demonstrated low coke formation and a higher activity (even at low temperatures) than Ni on the other supports due to good dispersion of NiO on C12A7 and the active oxide ions in the C12A7 crystallite cages.[110]

Matsuishi *et al.* described the production of a stable inorganic electride, $[Ca_{24}Al_{28}O_{64}]^{4+}(4e^-)$, abbreviated to C12A7:$e^-$.[102] The method describes the removal of interstitial oxygen ions from the crystallographic cages of C12A7. The resulting inorganic support compound C12A7:e^- has electrons densely localised within the cages (Figure 2-5). The conductivity of these electrons indicate their behaviour as anions within the chemically and thermally stable crystalline electride. Calculations of the electronic structure give a steady explanation of the high conductivity (*ca.* 100 $S \cdot cm^{-1}$)[102] and optical properties of the electride; the electrons in the positive framework hop between neighbouring cages.[101] At room temperature, C12A7:e^- displays metal characteristics (*ca.* 1500 $S \cdot cm^{-1}$) due to the large dispersion of electrons within a unique conduction band known as the cage conduction band (CCB), which is a result of the three-dimensional crystallographic cages.[2,111,112] The structure represented by these electrons can be interpreted as an F^+ centre and these 'anions' couple antiferromagnetically with each other to form a diamagnetic pair.[102,112]

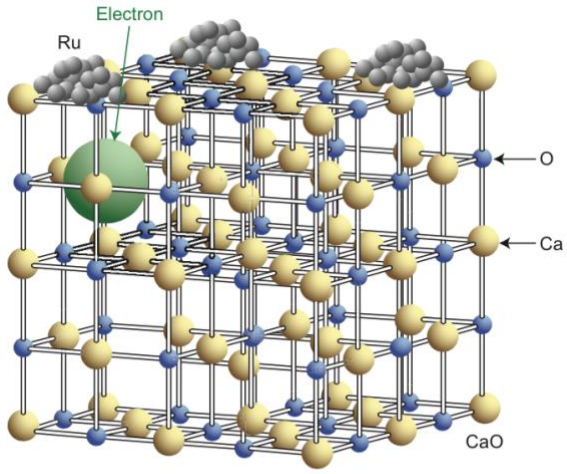

Figure 2-5 Crystallographic unit cells of C12A7:e^- showing an electron trapped within a cage. The electride is loaded with Ru nanoparticles (From Kitano[1]).

Initial synthesis of the electride was conducted via a solid-phase technique using Ca or Ti metal treatment for the reduction of C12A7 to C12A7:e^-. With increasing exposure to Ca treatment, the lattice framework and structure of C12A7 remained constant, conductivity was shown to increase and a colour change from colourless to green to black was observed.[102] Energy levels of the

clathrated electrons were shown to be *ca.* 1 eV below the CCB edge and had a small work function below 3 eV.[102] The intrinsic work function (ϕ_{WF}) of a compound is the energy required to transfer one electron from the Fermi level of a metal into a vacuum.[108] The electride is therefore thermally (melts at 1415 °C) and chemically stable in ambient environment which suggests its use for a number of practical applications.[107]

In order to determine the intrinsic work function of a compound, a pure intrinsic surface is needed.[108] This is difficult to prepare for C12A7:e^- because electrons in the cages near its surface interact with O_2 and/or water molecules in the atmosphere to form electron-deficient layers. Even if this was not to happen, the surface cages cannot trap an electron as they do not maintain the bulk cage structure, which suggest an insulating or semiconductive layer on the electride surface. Toda *et al*. particularly examined the electronic structure of C12A7:e^- using UV photoelectron spectroscopy (UPS, excited by He I and II) and photoelectron yield spectroscopy (PYS).[108] This determined the work function to be as low as *ca.* 2.4 eV, comparable to alkali metals.

Further research on this electride by Kitano *et al.* in 2012 reported the Ru-loading onto the electride support as an efficient catalyst for the ammonia synthesis from its elements.[1] Due to the high electron-donating power of the electride and its stability, the catalytic activity of this process was increased compared to other previously reported supported Ru catalysts. The encaged electrons within C12A7:e^- were postulated to donate successfully to the Ru metal. Furthermore, hydrogen poisoning of the Ru surface (see section 2.4.1), is minimised by the reversible hydrogen storage ability of C12A7:e^-.[1]

Kuganathan *et al.* further explored activity testing of the electride in 2014, which showed the enhancement of N_2 dissociation, allowing the improvement of the catalytic activity of the Ru-loaded catalyst.[113] The back donation of electrons from the metal and support to the antibonding orbital of the N_2 provide a lower activation barrier to easily dissociate the strong N-N bond. The adsorption of N_2 on Ru is either *cis*-Ru_2N_2 or *trans*-Ru_2N_2, with the latter being more stable.[113] However, the *cis*-Ru_2N_2 is more stable when complexed with the electride due

to its electron donating power. Weakening of the Ru-adsorbed N-N bond is therefore much easier.

Due to the success of the electride, Inoue *et al.* further explored its synthesis in 2014 via a novel hydrothermal process.[2] This method was considered more advantageous to the conventional solid-phase synthesis due to the increase of surface area of the material (*ca.* 20 $m^2 \cdot g^{-1}$ as opposed to previously reported 1 $m^2 \cdot g^{-1}$)[2] and a two-fold rate of ammonia synthesis over Ru-loaded onto the electride was measured. It was also revealed that Ru nanoparticles show a higher dispersion on hydrothermally produced C12A7:e^- (HT-C12A7:e^-) than on solid-phase synthesised C12A7:e^- (SP-C12A7:e^-). The former method comprises the calcination of a hydrothermally produced $Ca(OH)_2$ and $Al(OH)_3$ mixture ($Ca_3Al_2(OH)_{12}$) followed by reduction with CaH_2 [2] (see experimental section 4.1). A variation in the synthesis by Inoue *et al*. involved a change in evacuation temperature; this was the temperature at which the C12A7 powder was heated at under vacuum during synthesis. The Brunauer-Emmett-Teller surface area (S_{BET}) and pore volume for the HT-C12A7:e^- was shown to decrease with increasing evacuation temperature. Decrease in surface area was suggested to be due to the aggregation of C12A7 nanoparticles. The absorbance spectra of the interstitial electrons within the electrides was determined in order to get their electron densities, which were calculated from the Kubelka-Munk[114] transformation of diffuse reflectance spectroscopy (DRS) results by Matsuishi *et al*.[109] These were shown to increase with increasing evacuation temperature (see Table 2-1).

Table 2-1 BET surface area, pore volume, and electron density of the synthesised C12A7:e$^-$ samples (adapted from Inoue *et al.*)[2]

Sample	*Evacuation Temperature (K)*	*Pore Volume ($cm^3 \cdot g^{-1}$)*	*S_{BET} ($m^2 \cdot g^{-1}$)*	*Electron Density (10^{21} cm^{-3})*
HT-C12A7:e$^-$	873	0.155	46	
	973	0.105	37	
	1073	0.037	23	0.7
	1173	0.036	17	1.0
	1273	0.020	6	1.6
SP-C12A7:e$^-$	1273	0.002	1	2.0

The proposed pathway for ammonia synthesis using C12A7:e$^-$ loaded with Ru can be expressed in four steps (Figure 2-6).[1] The first step involves an electron transfer to the Ru nanoparticles deposited on the C12A7:e$^-$ surface. Back donation from the Ru *d*-orbitals to the π^*-antibonding orbitals of the N_2 feedstock adsorbed to the Ru surface causes N-N bond weakening in the second step. Hydrogen adsorbed atoms (adatoms) are spilled over onto C12A7:e$^-$ following a dissociative adsorption. Step three consists of the spilled adatoms being reduced to hydride anions from the electrons within the nanocages of C12A7:e$^-$. Nitrogen adsorbed to the Ru surface interacts with these hydride anions, which then allows the resulting electrons to be recovered back to the nanocages of C12A7:e$^-$. The final step allows for the formation of ammonia from the intermediate species adsorbed to the catalytic active site and recovery of the electride system.[1] Kitano *et al*. further discovered in 2015 that the rate-determining step is not the N-N triple bond dissociation but the subsequent formation of N-H_n species.[115]

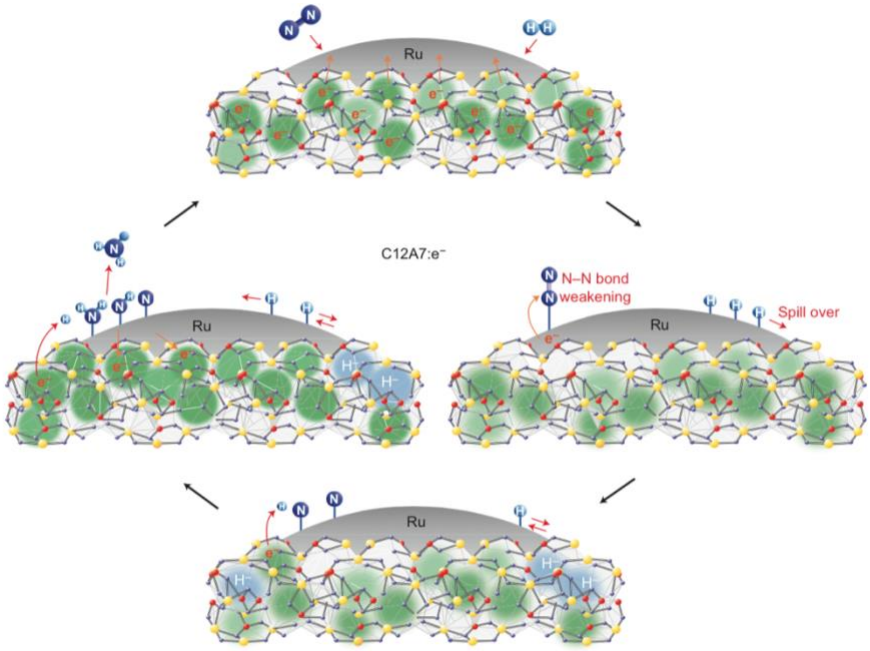

Figure 2-6 Proposed pathway of ammonia synthesis using Ru/C12A7:e$^-$ (From Kitano[1]).

As no superconductivity was reported for representative metal oxides such as Al_2O_3 and SiO_2, or any electrides, a study by Miyakawa *et al*. investigated the magnetic susceptibility as well as electrical resistivity with and without an external magnetic field for single crystal and thin films of the C12A7:e$^-$ electride.[105] They found that superconducting transition (T_c) was observed for all samples, with the T_c in the range of 0.14 – 0.4 K.[105] The electride was prepared via the solid-phase synthesis and included reduction treatment by Ti metal. At 300 K bulk electride showed electric conductivity (~770 – 810 S·cm^{-1}).[105] Further observations indicated that the electride is a superconductor below ~0.4 K dependent on the anionic electron concentration; the superconductivity is destroyed by a magnetic field above a critical magnetic field of 30 mT.[105] These results indicate the electride as a favourable material for research in novel superconductors.

2.2.2 Potential of C12A7:e$^-$ electride - $[Ca_{24}Al_{28}O_{64}]^{4+}(e^-)_4$ for use as a substitute to alkali promotion of Fe FTS

With the increasing interest of Chinese companies to develop FT technology centred on coal based synthesis gas, iron-based FT catalysts are experiencing

a renaissance.[116] These catalysts are always electronically promoted by alkali which enhance the selectivity and activity of the catalyst; the alkali levels are proportional to the chain growth probability.[21] Due to having a low work function, these metals act as Lewis bases to control the acid/base sites on the catalyst surface.[117] Improvement of final catalyst surface area may be stimulated by addition of structural promoters.

Optimal alkali content is favoured as it decreases methane selectivity, however a level above the optimum induces an increased rate of carbon formation on the catalyst. Potassium (typically as K_2O or other salts) is one of the most common alkali promoter, amongst other metals such as Li, Na, Rb and Cs for iron FT synthesis.[82,118] Alkali promotion is said to also increase the overall WGS activity.[22] However, the alkali metal may affect the catalytic activity of the FTS depending on the conversion levels, such as Li which was shown to act as a promoter at low conversions and as an inhibitor at high conversions.[118]

The ability to donate electrons to the active site of the catalyst can lead to an increased bond strength between C and the catalyst surface resulting in a decrease of the C-O bond. The C12A7:e^- electride is postulated to mimic the effects of potassium promotion for iron catalysts in the FTS.[22]

The use of alkali metals, although generally advantageous to catalytic activity, may induce unwarranted effects on the FTS such as a possible increased methane selectivity (at high conversions), blockage of pore sites leading to increase deactivation rates and higher WGS activity.[9,119] The use of the electride system to increase electron availability, may reduce some of these effects with the elimination of alkali content, thereby increasing the overall efficiency of the Fe FT catalyst.

2.2.3 Additional electride compounds with potential for use in FTS and other catalytic reactions

Since the discovery of C12A7:e^- as a Lewis base, research into electride compounds has drawn greater interest. Further crystalline compounds with thermal and chemical properties have been studied to determine if they may possess electride effects.

A class of compounds of interest that may be considered electride compounds is that of nitrides with alkali metals or alkaline earth metals. From these compounds of interest, Li_3N[120] was shown to be the only stable alkali metal nitride with partial stability shown in compounds such as Be_3N_2, Mg_3N_2, Sr_2N[121] and Ba_3N[122] from the alkaline earth metals.[123] However, of particular interest in the field of nitride electrides is Ca which forms the ionic nitride Ca_3N_2[124] and the stable subnitride Ca_2N.[123,125,126] Dicalcium nitride has been regarded as the first two-dimensional electride compound containing a layered structure with its anionic nature suggested as $[Ca_2N]^+ \cdot e^-$.[127,128]

The C12A7:e^-, although chemically and thermally inert may not be as stable under pressure due to its three-dimensional structure with the binary nitride compound expected to test better under pressure. The Ca_2N material was reported by Lee and co-workers to have a high electron mobility (520 $cm^2 \cdot V^{-1} \cdot s^{-1}$) and low work functions of 3.5 and 2.6 eV leading it to be the most delocalised anionic electride system reported to date.[128] Several synthetic routes to form Ca_2N have been reported, the most notable being the reduction of Ca_3N_2 under Ar, the reduction of Ca_3N_2 under vacuum and the reaction of Ca in liquid Na with N_2 gas.[123] Synthesis methods involve the use of inert atmosphere as Ca_2N and molten alkali and alkaline earth metals are highly reactive with atmospheric water vapour and oxygen. Research of two-dimensional electride systems in practical applications analogous to the C12A7:e^- family is projected to increase over the foreseeable future.

2.3 Catalyst preparation techniques

There are several ways of preparing a catalyst, the technique used does affect the stability, selectivity and activity of the catalyst.[129] Solid catalysts fall into one of three classes regarding the preparation technique required: bulk catalysts (active substances) and supports, impregnated catalysts (an existing support impregnated with the active phase or pre-active phase) and mixed agglomerated catalysts (agglomeration of a mixture consisting of active material with powdered support or support precursor).[130]

Iron-based catalysts may be prepared via precipitation, fusion of iron oxides or by decomposition of iron precursors onto support materials. Bulk catalysts are generally precipitated out as a solid from a liquid solution. Fusing of unsupported metallic or oxidic precursors occurs in either the gas-phase or liquid-phase.[54]

The two most common methods to deposit iron onto a support material are incipient liquid-phase (wetness) impregnation and precipitation/co-precipitation.[131] The first method involves an introduction of the catalyst precursor at a volume equal to the pore volume of the support material; thus, allowing no solution to remain outside of the pores of the support material.[47,132] The impregnation technique to deposit a metal salt species onto a support material may occur in the solid-liquid phase involving four steps: impregnation, equilibrium or aging, solid-liquid separation and drying. The alternative gas-solid or solid-solid interface involves two additional steps: air-calcination (in the case of oxidic catalysts) and activation (such as hydrogen reduction of metallic catalysts and sulphidation of sulphided catalysts).[133]

The precipitation technique involves the dissolution of a metal precursor (often a salt) into a homogenous solution in the presence of the support material; or with simultaneous precipitation of the support material from another precursor/salt for co-precipitation.[28] A precipitation agent such as a base solution is used to alter the pH and precipitate the metal salt onto the support.[134]

Physical deposition methods include mechanical milling, laser ablation, flame spraying and thermal decomposition; whilst chemical methods include sol-gel processing, hydrothermal, precipitation, combustion methods, vapour phase deposition and microemulsion.[134] Other more infrequently used techniques include ion exchange and synthesis from organometallic compounds.[135]

The present model catalysts in this study require iron deposition onto the novel support systems without destroying the crystallite nanocages of the electride support. Careful deliberation is required to choose a suitable preparation technique of the iron deposition. A metal decomposition technique in which a metal precursor is decomposed over the support system is recommended for the decomposition of the iron-based catalyst onto the C12A7:e^- support.[136] The C12A7:e^- is sensitive to ion exchange, and it would be most appropriate to attempt deposition by dry techniques in order to preserve the electron storage ability of the electride.

2.4 Catalyst deactivation

Unfortunately, all heterogeneous catalysts are subject to deactivation with time-on-stream (TOS). The various processes contributing to this decay in efficiency range over several time scales from seconds to years. Under reaction conditions catalysts are subjected to deactivation by chemical, thermal and mechanical stress, which may reduce their rate of regeneration.[137]

Five main mechanisms of catalytic decay have been reported; these include poisoning, vapour compound formation (which can involve leaching amidst transport from the catalytic active site), as well as gas-solid or solid-solid reactions. Mechanical deactivation can occur by fouling or attrition/crushing. Catalysts can also be subjected to thermal degradation such as sintering.[137,138] Iron-based FT catalysts are most vulnerable to fouling, sintering, chemical poisoning (usually by sulphur) and the loss of active phase species to an inert phase.[49]

2.4.1 Poisoning

Poisoning occurs through strongly chemisorbed compounds to the catalytic active site, which decrease the availability of sites for catalysis to occur; often poisoning is by feed stream compounds and can be reversible or irreversible.[137,139,140] The adsorption strength of a species, be it reactant, product or impurity determines its ability to adsorb to catalytic active sites. A species may be considered a poison if its ability to chemisorb to these sites is significantly higher relative to the reactant species.[137,139] Adjacent or nearby sites may be affected by poisoning due to induced geometric or electronic changes in the structure of the catalytic surface. The deactivation caused by reversible and irreversible poisons is the same for the duration of the poison being adsorbed to the catalytic surface, however the effects of reversible poisons, which are observed less frequently, are temporary as they can be desorbed under special treatment.[137,140,141] Irreversible poisons, such as many sulphur-containing compounds block the catalytic surface permanently.

Poisons can be categorized by varying aspects including their selectivity to metal surfaces, degree of shielding and oxidation states (having a higher or lower number of electrons available for bonding).[139] The efficiency of the poison is directly proportional to its atomic/molecular size and electronegativity.[142] In the FTS, particularly with iron-based catalysts, the most common poisons, many of which are present in the feed stream, include metal carbonyls, H_2S, COS, CH_3SH[143] , C_2H_5SH[144], NH_3 and As.[49,137]

The selectivity of a poison can be investigated via comparing the catalyst activity (normalized reaction rate) against the normalized poison concentration. Poisoning can be selective, anti-selective or nonselective. Nonselective poisoning occurs from a directly proportional relationship of loss of activity to amount of chemisorbed poison.[145] Selective poisoning comprises that the poison is preferred on most active sites to other species at low concentrations.[137,141] Anti-selective poisoning occurs if active sites are blocked initially by other species than poisons.[146]

2.4.2 Fouling

Fouling is the deposition of mostly carbonaceous species onto the catalytic surface and within its pores resulting in a loss of activity due to pore blockage.[49] This could lead to the disintegration of catalyst particles as well as transport limitations and site blockage. Carbon (produced from CO disproportionation) and coke (produced from hydrocarbon decomposition or condensation) are generally deposited onto the surface sites, including other chemisorbed carbons and condensed hydrocarbons.[137] These residues may vary in molecular size depending on the catalyst or reaction type and conditions.

The mechanism of formation varies depending on the catalyst. For example, on supported metal catalysts, carbon formation blocking active sites may occur by mono- or multilayer chemisorption, particle encapsulation, micro- or mesopore blockage resulting in limited access of reactants to pores within crystallites and total disintegration of particles by large carbon build-ups induced by stress.[137,147]

Reaction temperature and reactant composition has a major effect on fouling rates, and on the difference between the rate of formation and gasification of carbon/coke precursors.[147–149] For hydrocarbon reactions on metal oxide and sulphide catalysts, coking may occur in the gas phase and on both active and non-active surfaces.[137] Cracking reactions often lead to coke formation from acid catalysis.[150,151] Factors affecting this are the precursor structure, reaction conditions, pore structure and catalyst acidity.[137,148]

Researchers have widely categorized catalytic reactions as coke-sensitive or coke-insensitive, the latter includes FTS.[152]

2.4.3 Thermal degradation

Thermal degradation and sintering involves loss of catalytic surface area by heat and pressure causing a solid agglomeration on the catalyst surface without melting.[137] This process occurs via structural modifications and is physical in

nature.[138] Thermal degradation may also induce loss of support area/catalytic active area due to a collapse of the support or pore structure and is stimulated by high temperatures and the presence of water vapour.[137,147]

In supported metal catalysts, small metal crystallites can agglomerate into larger ones reducing the active surface area of the catalyst. Several factors may enhance the rate of sintering, however the temperature remains the most influential followed by the atmosphere.[153] Others include the metal type, metal dispersion, porosity, the presence of promoters/impurities, and the support surface area and texture. The temperatures at which thermal degradation occurs are indicated as the Hüttig or Tamman temperatures and are directly related with the melting point of the metal (T_{mp}). At the Hüttig temperature (0.3 T_{mp}), the weakly bound surface atoms at edges and corners known as defect sites dissociate and diffuse over the catalyst. At the Tamman temperature (0.5 T_{mp}) the bulk atoms become mobile.[137,154]

In the atomic migration model, or Ostwald ripening, used to describe sintering, metal atoms from the crystallite surface are released and transported across the support surface or via gas-phase movement and collide with other (ultimately larger) metal crystallites.[137] Larger crystallites are increased due to their stronger metal-metal bond energies than metal support interactions. In the crystallite migration model, sintering occurs via migration of the crystallites along the support material with the coalescence of two or more crystallites. Although the atomic migration model is favoured over crystallite migration model at lower temperatures, the pathways of sintering are often believed to be coupled and occur simultaneously as the reactions proceed.[137]

Sintering of support materials such as the electride may occur by one or more mechanisms including surface diffusion, solid-state diffusion, volatile atoms/molecule evaporation/condensation, grain boundary diffusion and phase transformations. Alkali metals such as potassium are known to accelerate sintering and the omission of these metals, with the proposed use of the electride in this FTS study is suggested to reduce one aspect of catalyst deactivation.[153–156]

2.4.4 Vapour-solid and solid/solid reactions

Gas-solid and solid-solid reactions occur from reactions of the catalyst metal and gas, the support or a promoter in the pore system to render the catalyst inactive. Gas-solid reactions, although similar to poisoning, are different as the adsorbed gas species such as oxide bearing compounds in the iron catalysed ammonia synthesis causes loss of activity by inducing a phase change i.e. from Fe^0 to iron oxide.[137,157]

Metal loss can cause significant deactivation over a wide range of conditions through the formation of volatile compounds such as metal carbonyls, oxides, sulphides and halides through vaporization.[137,147] Solid-solid diffusion is an important mechanism in the degradation of complex catalysts used for hydrocarbon synthesis, oxidation and dehydrogenation reactions. In FTS, this is particularly important in the formation of inactive or less active/selective carbides in Fe/K/Cu catalysts.[137,158] A major cause of deactivation in precipitated iron FT catalysts is proposed to be due the oxidation of iron carbide phases Fe_xC and χ-Fe_5C_2.[159]

2.4.5 Attrition/crushing

Attrition/crushing is the result of mechanical stress due to abrasion within a reactor as a result of movement and/or thermal strain.[137] Mechanical failure could occur due to crushing of granular/pellet catalysts in fixed bed reactors; and erosion or fracture of catalytic particles or monolith coatings at high inlet gas feeds.[137,160,161] Besides the loss of catalytic material, increased pressure drops or blockages can be the result. Mechanical stress may also be caused by particle collisions and shear forces in a fluidised bed.

Iron catalysts often experience attrition at increased temperatures when exposed to syngas.[162,163] Attrition was shown by Kalakkad and co-workers to occur on precipitated iron FT catalysts on both a micro- and nano-level scale by breakup of agglomerates into primary crystallites due to physical stress and by phase transformations or carbon deposits on the catalyst.[163] A major

disadvantage of FT slurry phase and fluidised-bed reactors over fixed bed reactors (see section 2.1.8) is that they experience a greater deal of catalyst particle breakdown due to attrition and/or carburisation.[49]

3 SCOPE OF STUDY

3.1 Aims

The aim of the proposed study is to synthesize a support material that supplements the common physical properties of a support material, i.e. increasing catalytic surface area and particle separation through possessing anchoring sites, by providing a chemical role of having a low intrinsic work function comparable to potassium promotion.

3.2 Motivation for research

The C12A7:e^- electride is expected to perform these tasks in section 3.1, however without the disadvantages such as coverage of active sites by alkali promoters. C12A7:e^- has shown an increased activity in the Ru catalysed ammonia synthesis due to an increased N_2 adsorption and dissociation. It is anticipated to have similar effects on CO adsorption and dissociation in the FTS.

3.3 Objectives

i. The first objective is the synthesis and characterisation of C12A7:e^- using the hydrothermal process described by Inoue *et al.* (section 4.1.1) due to its ability to produce higher surface area materials compared to the solid-phase synthesis.[1,2,109] Two variations of the synthesis is conducted to tune the work function; i.e. different temperatures are applied during the vacuum calcination (800 °C and 1000 °C). The unreduced C12A7:e^- compound, the mayenite (C12A7) precursor, serves as a control for this study as it is expected not to possess the electronic properties of its reduced counterpart. A baseline performance is defined by an unpromoted bulk precipitated iron catalyst.

ii. Iron(III) oxide is deposited onto the three support materials using a dry metal precursor decomposition method of an organometallic precursor (section 4.2) to avoid any re-oxidation of the supports through aqueous techniques. Deposition of iron(III) oxide on freshly synthesised Stöber silica spheres is used to investigate the iron phases and deposition conditions prior to deposition on supports of interest.

iii. Investigation of the iron-loaded electride and mayenite systems is compared to the unpromoted precipitated iron catalyst under LTFT synthesis conditions.

3.4 Hypothesis

The novel chemically and thermally stable inorganic electride, C12A7:e^- has shown to result in a two-fold increase in catalytic activity of ammonia synthesis from its elements using a Ru catalyst. It is expected to have a similar catalytic effect in the iron-based FTS. This is rationalised through the electron donating ability of the electride, therefore acting as a Lewis base aiding in the strengthening of the C-catalyst bond and weakening the C-O bond facilitating CO dissociation. Based on this functionality, the electride is expected to act as a substitute to alkali promotion of the Fe FT catalyst as well as provide a rigid support which improves dispersion and increases the number of catalytic active sites. The selectivity and activity of the electride catalysts is expected to be enhanced at a lower methane and higher C5+ selectivity, and higher olefin selectivity due to suppressed secondary reactions compared to control catalysts.[9]

3.5 Key questions

1. Can the C12A7 and C12A7:e^- compounds be reproducibly synthesised according to hydrothermal synthesis method previously described in literature?[2]

2. Is $Fe(acac)_3$ a suitable organometallic precursor to deposit onto the support material in a dry deposition technique?

3. Is it possible to substitute alkali promotion of Fe FT catalysts with the C12A7:e^- electride support system, thereby increasing its catalytic activity and enhancing its selectivity compared to that of the control catalysts?

4 EXPERIMENTAL SECTION

4.1 Preparation of iron support systems

4.1.1 Hydrothermal synthesis of C12A7 (mayenite)

The hydrothermal synthesis of the mayenite precursor has previously been described in literature.[2] A stoichiometric mixture of $Ca(OH)_2$ (≥ 96%, Sigma-Aldrich) and $Al(OH)_2$ (ACS, Sigma-Aldrich) (Ca:Al = 12:14) was milled in distilled water (*ca.* 0.135 g solid per mL water) with agate beads for 4 h using a McCrone micronizing mill. The resulting product was treated in a Teflon-lined autoclave (Berghof BR-300 high pressure reactor and BTC-3000 temperature controller) at 150 °C (5 °C·min^{-1}) for 6 h under stirring (150 rpm). The solid product was separated from the liquid via centrifugation at 7000 rpm (Beckman Coulter Avanti J-E centrifuge) and dried at 120 °C overnight in air (Memmert Oven). The mixed metal hydroxide, proposed by Inoue and co-workers[2] to be of the structure $Ca_3Al_2(OH)_{12}$, was calcined in a vertical quartz fluidised-bed reactor (see Figure 4-1) at 600 °C for 5 h in air (10 °C·min^{-1}, 60 mL·min^{-1}) yielding mayenite - $12CaO{\cdot}7Al_2O_3$ powder.

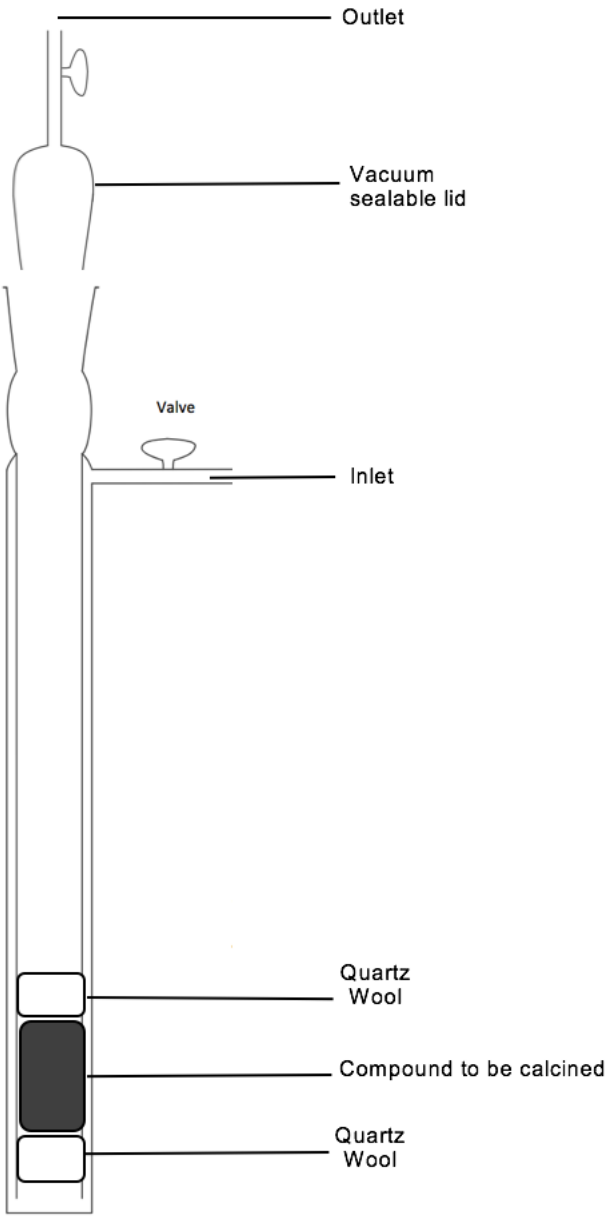

Figure 4-1 Schematic of calcination tube (under 60 mL·min^{-1} air or vacuum) set-up which is inserted into a vertical tubular furnace.

4.1.2 Hydrothermal synthesis of C12A7:e$^-$ (electride)

C12A7 was heated in the previously described calcination reactor at either 800 or 1000 °C (10 °C·min^{-1}) for 5 h under constant vacuum (*ca.* 1 x 10^{-4} Pa, Edwards pump, model: RV3 with EXT76DX turbomolecular pump) to remove water and hydroxyl groups within the crystallographic cages or adsorbed on the compound's surface.[2] Reduction to the electride, i.e. replacement of O^{2-} ions in the crystallographic cages with four electrons, is achieved by mixing the

mayenite with an excess amount of CaH_2 (powder, 99.99% trace metals basis, Sigma-Aldrich) (0.1333 g CaH_2 per gram of C12A7, ~ 77 % stoichiometric excess) in a quartz reactor tube under an inert N_2 atmosphere (MBRAUN UNIlab Pro Glove Box Workstation with PLC Control Panel – Siemens Simatic OP7 Operator Panel and Edwards RV3 pump). The tube is sealed and a vacuum is applied (*ca.* 1 x 10^{-4} Pa) before heating to 650 °C (10 °C·min^{-1}) for 15 h. The obtained electride compound is annotated in the present study as C12A7:e^- (800 or 1000 °C depending on initial vacuum calcination temperatures).

4.1.3 Synthesis of Stöber silica spheres

Synthesis of Stöber spheres was performed using a method described by Wang *et al*. in 2010.[164] Ammonia solution (25% A.R., Sigma-Aldrich, 102.5 mL) was added to an Erlenmeyer flask with ethanol (99.9 %, A.R., Kimix, 513 mL) and stirred for 10 min (200 rpm, Heidolph HG3001K). A TEOS (98%, A.R., Fluka, 5.13 mL) in ethanol (20.52 mL) solution was added to the ammonia bearing flask and stirred for an additional 2 h at RT (200 rpm). A further TEOS (71.82 mL) in ethanol (287.28 mL) solution was added to the ammonia solution dropwise over 20 min. The final solution was stirred at RT for 2 h (200 rpm) to allow for silica precipitation. The precipitate was subsequently centrifuged at 8000 rpm for 10 min (Beckman Coulter Avanti J-E centrifuge) and washed with ethanol four times, followed by further centrifugation and drying overnight at 120 °C in air. A schematic of the synthesis process is shown in Figure 4-2.

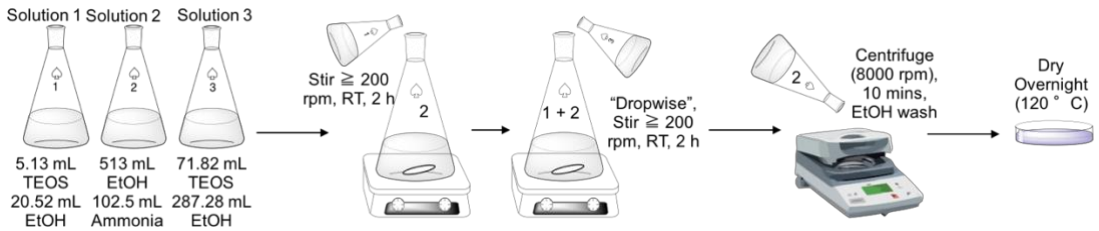

Figure 4-2 Schematic representation of the synthesis of Stöber SiO_2 spheres as described in Wang *et al.*[164]

4.2 Iron loading onto support materials/catalyst deposition method

Metal deposition onto the electride and mayenite substrates was realized using iron(III) acetylacetonate ($Fe(acac)_3$) (≥ 99.9% trace metals basis, Sigma-Aldrich) as the precursor. To determine the ideal conditions of the metal decomposition onto the selected supports, thermogravimetric analysis (TGA) was performed of the iron precursor to determine its decomposition temperature conditions (section 4.4.2). Trial deposition of $Fe(acac)_3$ was then done onto Stöber silica spheres at the selected temperatures under stagnant or flowing (100 $mL \cdot min^{-1}$) argon or synthetic air to determine which condition selectively ensures a majority hematite phase on the support.

A stoichiometric amount of $Fe(acac)_3$ (10 wt. %) was added to the support of choice and dry-sonicated for 20 min to achieve a good mixing (Labcon Ultra-Sonic 5019(L)). The resulting mixture was placed in a stainless-steel reaction chamber between two stainless-steel rods and sealed (Figure 4-3). The reactor set-up was positioned in a horizontal tubular furnace (Labofurn, Kiln Contractors (Pty) Ltd. with a Caho P961 temperature controller). The sample was heated to 100 °C (2.5 $°C \cdot min^{-1}$) under a constant flow of synthetic air (100 $mL \cdot min^{-1}$) for 30 min. Subsequently the temperature was increased to 400 °C (10 $°C \cdot min^{-1}$) and held for 2 h to facilitate the decomposition of iron. The air flow was stopped and after cooling to room temperature, the sample was removed from the reaction chamber.

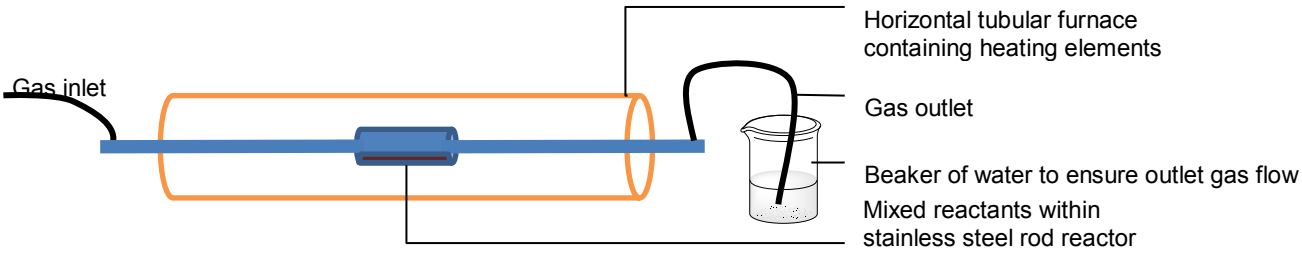

Figure 4-3 Generalised setup of the metal deposition reactor set-up for $Fe(acac)_3$ deposition.

4.3 Synthesis of unpromoted precipitated iron

The synthesis of unpromoted precipitated iron was previously reported by Iglesias *et al*.[165,166] Aqueous iron nitrate solution (1 M $Fe(NO_3)_3 \cdot 9H_2O$), 500 mL, Sigma-Aldrich) was heated to 95 °C. Quick precipitation was induced by addition of hot aqueous ammonia solution (5 wt. %) to the iron solution under vigorous stirring (24 000 rpm, Ultra Turrax T25 Basic) until a pH of 7 was reached. The obtained precipitate was filtered using a Buchner funnel and repeatedly washed with boiling deionized water. The catalyst precursor was subsequently dried overnight at 120 °C in air (Memmert Oven) forming a solid filtercake that was crushed using a mortar and pestle to a size fraction of 150 – 212 µm. The desired fraction was calcined in air in a fluidised-bed reactor (quartz tube) at 400 °C for 3 h (100 $mL \cdot min^{-1}$, 10 $°C \cdot min^{-1}$). To counter fines formation in the calcination process, the obtained powder was pelletized (3 T compression, Specac Auto Atlas Power T25 Hydraulic Press) and then crushed to the desired fraction.

4.4 Characterization

4.4.1 Particle size distribution during milling

The average particle size of the starting materials ($Al(OH)_3$ and $Ca(OH)_2$) as well as the slurry mixture of the combined starting materials was measured using the Malvern Mastersizer 2000. Laser diffraction of particles of assumed spherical geometry is used to determine a mean particle size distribution, with a stirrer speed of 820 rpm, pump speed of 2000 rpm and obscuration between 10 and 20. The sample was suspended in a water-bath (Hydro 2000G) and sonicated for 10 seconds prior to measurements in order to increase dispersion of particles. The refractive index parameter of the instrument was chosen to be 1.57. This value was based on the Mie theory[167], an assumption of spherical particle geometry, which the instrument uses and was estimated based on a library of used refractive indices for similar compounds provided by the manufacturer.

4.4.2 Thermogravimetric analysis (TGA) and differential scanning calorimetry (DSC)

The decomposition of the iron precursor, $Fe(acac)_3$ under argon and synthetic air (30 $mL \cdot min^{-1}$) was studied with a combined TGA/DSC instrument (NETZSCH STA 409 CD with TASC 414/3 controller). A known mass of sample was placed in a pre-weighed alumina crucible and heated to 800 °C (10 $°C \cdot min^{-1}$) under either gas while the weight loss was recorded.

The DSC scan was taken concurrently against a blank reference cell and no area or enthalpy measurements were taken. Indium was used as a standard to form the thermometric correction curve. The temperature of the adiabatic jacket was gradually heated during an upscan mode ensuring constant power to the main jacket heaters under constant gas flow. The samples were degassed before loading.

4.4.3 Powder X-ray diffraction (XRD)

Powder X-ray diffraction (XRD) was utilized to characterize the structure and crystalline phases of the starting materials, the synthesized mayenite, and electride compounds, both before and after iron deposition as well as in the spent catalysts. Stöber spheres (section 4.1.3) and the precipitated iron catalyst (section 4.3) were also analysed by XRD. The instrument used was a Bruker D8 Advance Laboratory X-ray diffractometer with a Co-Kα radiation source of 1.79026 Å wavelength at 35 kV and 40 mA equipped with a position-sensitive detector (LYNXEYE_XE energy-dispersive 1D mode, Bruker). The scan range was chosen between 20° and 120° 2Θ using a step scan mode (step size: 41.73 °/s, time per step: 1s, scan time: 4173 s, 15 rpm). Diffraction reflexes were compared to those reported by Inoue *et al.*[2] and reference patterns reported in the International Centre for Diffraction Database (PDF-2/Release 2008 RDB).

Where necessary, the crystallite size for an individual plane was calculated using the Scherrer equation[168,169] (Equation 4-1) by the instrument software.

Equation 4-1

$$\tau = \frac{K \cdot \lambda}{\beta \cdot cos\theta}$$

where:

τ = average size of the ordered crystalline domains

K = dimensionless shape factor (usually close to 1)

λ = X-ray wavelength

β = line broadening minus instrumental line broadening at full width half maximum (FWHM) (radians)

θ = Bragg angle (degrees)

4.4.4 Transmission electron spectroscopy (TEM)

Fresh catalysts were studied via TEM (FEI Tecnai F20 equipped with a LaB6 field emission gun operated at 200 kV). Each sample was suspended in methanol or ethanol, briefly sonicated and a droplet from the supernatant was loaded onto a carbon coated copper grid and dried for viewing in the microscope. All micrographs were processed using the Digital Micrograph (Gatan) software.

Further energy-dispersive spectroscopy (EDS) (operated in bright field mode at an accelerating voltage of 200 kV using an EDAX liquid nitrogen cooled lithium doped silicon detector) coupled to FEI Tecnai G2 20 field-emission gun TEM was performed on the Ca-Al hydroxide mixture and C12A7 compounds. This analytical technique involves the induction of a high-energy electron beam over various regions of focus within the sample in order to obtain an elemental analysis comparison of the homogenous starting material compound and proposed crystal cage structure based on the electromagnetic emission spectra of the atoms present.

4.4.5 Brunauer-Emmett-Teller (BET) physisorption

The Brunauer-Emmett-Teller (BET) surface area was determined by N_2 adsorption and desorption[170] (Micromeritics TriStar II 3020 Micromeritics Instruments Corp., USA). Each sample was placed in a physisorption tube, degassed under vacuum at 90 °C for 1 h to ensure the sample was dry and all water was removed. The temperature was increased to 120 °C, further degassed overnight and subsequently cooled to room temperature. Analysis was initiated by cooling the samples to cryogenic temperature using liquid N_2. Nitrogen gas was then flowed over the samples at various controlled pressures. The pressure of the system is proportional to the number of gas molecules adsorbed to the sample surface. The relative pressure ratio (P/P_0) is determined from the saturation pressure (P_0) and absolute pressure (P) recorded from the system along with the total quantity of gas adsorbed by the sample (v). The BET equation (Equation 4-2)[170] was plotted with (P/P_0) on the x-axis and the left-hand side of Equation 4-2 on the y-axis. The gradient and y-intercept of the linear plot observed was then used to calculate the values for the volume of the monolayer of gas adsorbed to the catalyst surface (v_m) and a constant referred to as the BET constant (c).

Equation 4-2

$$\frac{1}{v \cdot \left[\left(\frac{P}{P_0}\right) - 1\right]} = \frac{c - 1}{v_m \cdot c} \cdot \left(\frac{P}{P_0}\right) + \frac{1}{v_m \cdot c}$$

where:

v_m = volume of the monolayer

c = BET constant

P = absolute pressure

P_0 = saturation pressure

v = adsorbed gas quantity

The BET surface area (S_{BET}) was subsequently calculated from Equation 4-3.[171]

Equation 4-3

$$S_{BET} = \frac{v_m \cdot N \cdot s}{V \cdot a}$$

where:

v_m = volume of the monolayer

N = Avogadro's number

s = adsorption cross section of the adsorbing species

V = molar volume of adsorbate gas

a = mass of the solid sample

4.4.6 Confirmation of iron loading

Both atomic absorption spectroscopy (AAS) and inductively-coupled plasma optical emission spectroscopy (ICP-OES) was performed to determine the Fe loading (wt. % Fe) on the supported catalysts. Samples were mixed with distilled water to a solid concentration of 0.500 $g \cdot L^{-1}$. In an Xpress Teflon tube, 50 mL of this suspension was mixed with 6 mL HCl, 2 mL HNO_3 and 2 mL HF consecutively, stirred with a glass rod and stored overnight in a room temperature fume hood to let the reaction complete and to prevent pressure build up due to collection of volatile gases. The suspension was then placed in a MARS-5 microwave digester for 15 min (1600 W, 180 °C). Once digested, the samples were made up to a volume of 100 mL using deionized milli-Q water. The samples were analysed using the AAS instrument (Varian SpectraAA 110) and/or the ICP-OES instrument (Varian 730-ES). The Fe loading can be determined according to Equation 4-4.

Equation 4-4

$$L = \frac{x \cdot 10}{m}$$

where:

L = wt. % Fe loading

x = concentration of Fe obtained from instrument measurement in $mg \cdot L^{-1}$

m = mass of the catalyst digested in mg.

4.4.7 X-ray photoelectron spectroscopy (XPS)

The oxidation state of the iron oxide species deposited on the electride was studied using X-ray photoelectron spectroscopy (XPS) (Kratos Axis Ultra DLD photoelectron spectrometer utilising monochromatic Al radiation – 1486.6 eV photon energy). The data for high resolution spectra and survey scans was obtained at a pass energy of 40 eV and 160 eV respectively; while the step size was 0.1 eV and 1 eV respectively. All spectra were calibrated to the C(1s) line which was taken to be 284.8 eV following the charge compensation which was achieved by the Kratos immersion lens system.

4.4.8 Temperature programmed reduction (TPR)

Temperature programmed reduction (TPR) was performed with the Fe-loaded mayenite, and electrides (800 °C and 1000 °C). A quartz U-tube with 30 – 50 mg of catalyst for each experiment was set up in the TPR instrument (Micromeritics Autochem 2950 HP). To determine the degree of reduction (DOR) of the supported catalysts, two separate TPR experiments were performed on each of the catalysts. The first was a conventional TPR experiment which involved heating the catalyst to 800 °C (100 $mL \cdot min^{-1}$ 5% H_2 in Ar, 10 $°C \cdot min^{-1}$), followed by cooling down under Ar at room temperature to re-equilibrate the system flushing out any residue gas. The second experiment involved three steps, a treatment of fresh catalyst under the chosen reduction conditions for FTS (100 $mL \cdot min^{-1}$ H_2, 400 °C, 10 h, 1 $°C \cdot min^{-1}$), cooling to 50 °C (50 $mL \cdot min^{-1}$ Ar, 10 $°C \cdot min^{-1}$) followed by the conventional TPR as the third step. The DOR was determined by comparison of the hydrogen consumption of conventional TPR and TPR after reduction. It has to be noted that due to a lack of phase information, the present approach to obtain the DOR can potentially, especially at low DOR values, be translated to various phase compositions, i.e. various iron oxide species present.

4.5 Catalyst testing

4.5.1 Reactor set-up and experimental procedure

A catalyst sample corresponding to 100 mg of Fe was packed into a ¼" stainless steel (ID = 3.8 mm) U-tube reactor (see Figure 4-4) within the test unit set-up (see Figure 4-5). In order to ensure a stable temperature control, the reactor was mounted in an insulated aluminium block powered by two heating cartridges and holding a controlling K-type thermocouple at its centre.

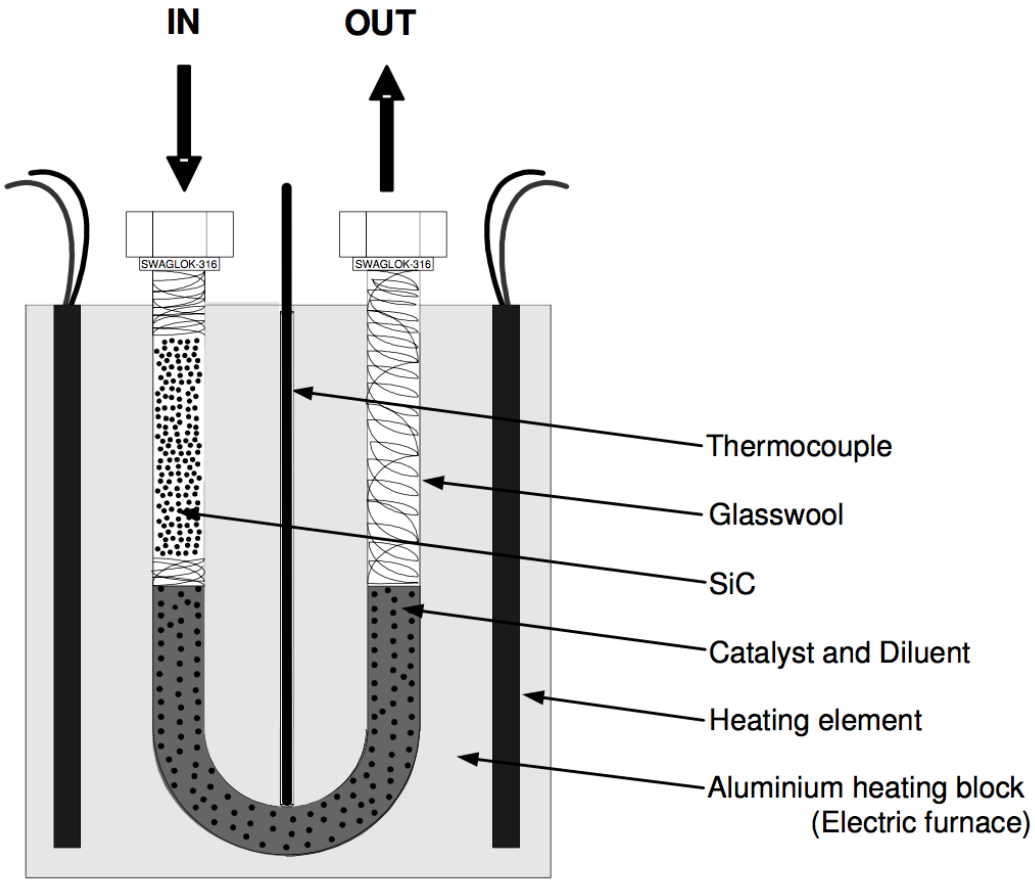

Figure 4-4 Arrangement of U-tube reactor and contents. (From Cairns.)[172]

All samples were reduced in situ in a stream of pure hydrogen (400 °C, 100 mL·min^{-1}, 10 h, 1 °C·min^{-1}, 1 bar) fed via a mass flow controller (MFC) (Brooks Instrument). After cooling to reaction temperature (240 °C) under a continuous flow of nitrogen, the reactor pressure is increased to 15 bar (absolute). The flow of N_2 at the desired pressure is controlled by a downstream

needle valve (NV). The flow is set slightly higher than the anticipated synthesis gas flow. The synthesis gas mixture (60 mLSTP·min^{-1} H_2/CO of 2:1) was allowed to stabilize via the bypass. Reference gas, a mixture of 0.1061 % neohexane in argon at 4.22 mLSTP·min^{-1}, was fed to the product stream after the pressure drop via the NV. The total gas stream is split between the online GC-TCD (gas chromatograph – thermal conductivity detector) and an ampoule sampler system (explained below) before going to vent. Once constant, the reaction is started by switching the four-way valve (4WV) to reactor mode and feeding syngas to the reactor and the pressure holding gas N_2 to the downstream line. Due to very low conversions, liquid product collection was not necessary using a hot or cold trap. All lines downstream of the reactor were kept at 180 °C. The analysis of the permanent gases (CO, H_2, N_2, CH_4, CO_2 and Ar) was conducted via online gas chromatography (GC) in a micro GC (Varian CP 4900) equipped with three separate column thermal conductivity detector (TCD) assemblies (see section 4.5.2.1).

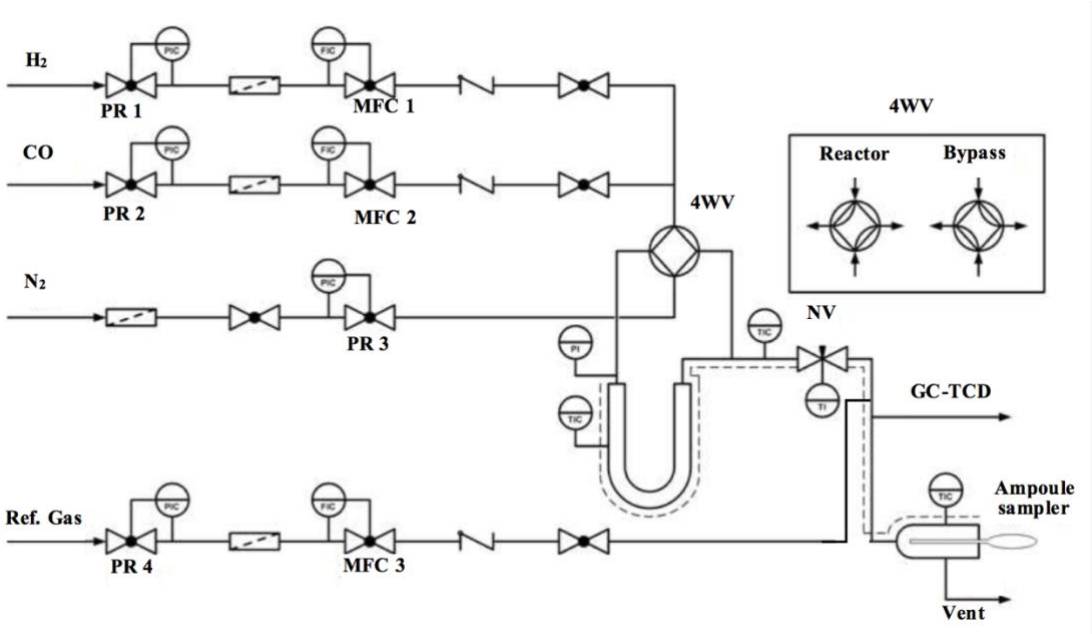

Figure 4-5 Schematic representation of the test unit set-up used for FT experiments. (Adapted from Fischer in 2011).[173]

The ampoule technique developed by Schulz *et al.*[174] was used to collect product gas for offline analysis by a flame ionisation detector (FID) equipped GC (see section 4.5.2.2).

Product gas was collected using limestone glass ampoules fashioned from commercially available Pasteur pipettes. A capillary (of *ca.* 120 mm in length and 1.5 mm in diameter) was drawn and sealed from one end using a butane/oxygen flame. The ampoule was evacuated using a vacuum pump and fully sealed (with internal volume *ca.* 2 mL). The glass capillary of the evacuated vessel is inserted through a septum into the product gas stream. With a breaking fork, the tip of the capillary is broken off resulting in the collection of product gas in the ampoule. The gas is entrapped by sealing off the remaining capillary with a blow torch, (see in Figure 4-6). Ampoules were collected at a relatively high frequency (i.e. every minute to every 30 minutes), while after *ca.* 6 h, ampoules were collected every 6 to 12 hours.

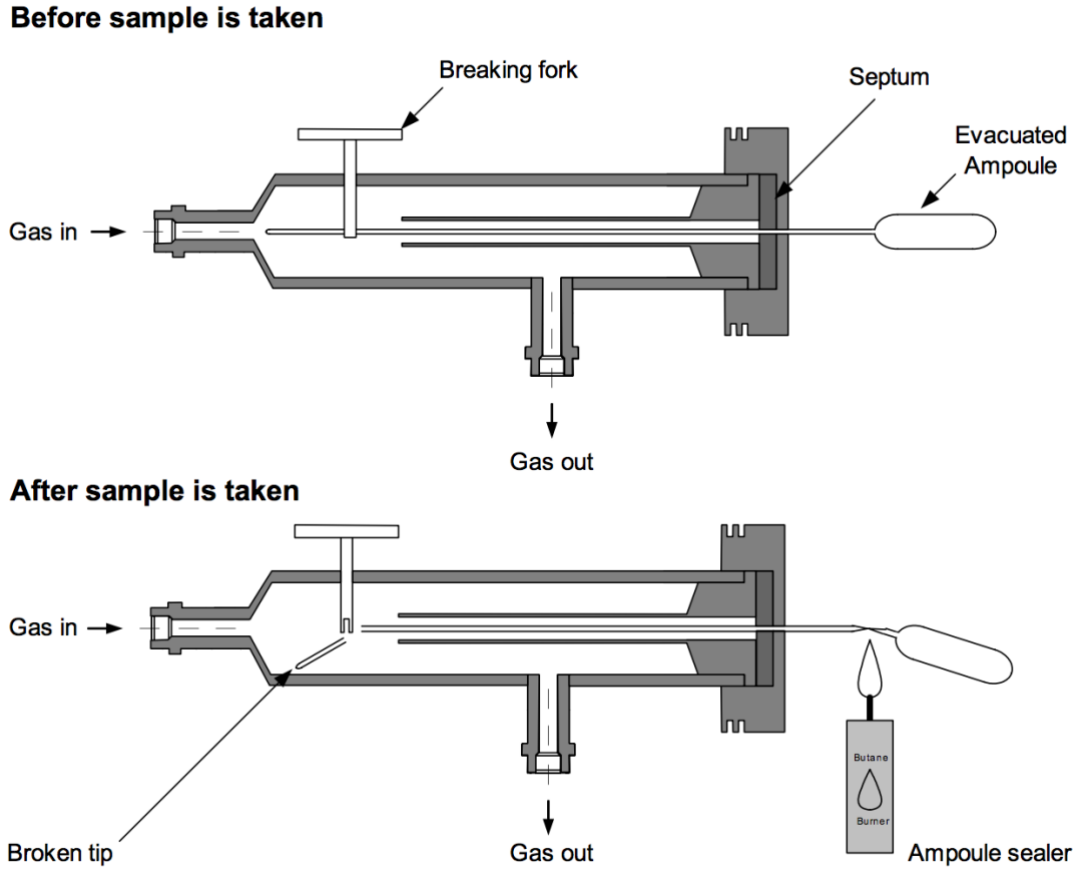

Figure 4-6 Schematic representation of the ampoule collecting system. (From Mabaso.)[28]

After a TOS of 48 h, the reaction was terminated by switching the 4WV back to bypass and switching off the synthesis and reference gas flows. The reactor was allowed to cool down under pressure and nitrogen flow.

The spent catalyst was removed from the reactor environment to be studied externally (section 4.4.3).

4.5.2 Product analysis

4.5.2.1 Gas chromatography – thermal conductivity detector (GC-TCD) analysis

Analysis of permanent gases, i.e. Ar, CH_4, CO, N_2, H_2 and CO_2 was achieved via a micro GC (Varian CP 4900) equipped with three columns and three thermal conductivity detectors (TCD) (for detailed set-up see Table 4-1). A known flow of argon in the reference gas was used as the internal standard. The product composition was determined via the correlation of peak area and response factor as a function of the Ar with the concentration in the gas stream according to Equation 4-5 to Equation 4-7. The respective response factors were obtained from a calibration with a reference gas mixture containing known amounts of Ar, N_2, CH_4, CO, H_2 and CO_2 (Afrox).

Equation 4-5

$$f_A \cdot \frac{[A]}{A_A} = f_B \cdot \frac{[B]}{A_B}$$

Equation 4-6

$$\frac{f_A}{f_B} = \frac{[B]A_A}{A_B[A]} = f_{Af(Ar)}$$

Equation 4-7

$$[A] = \frac{1}{f_{Af(Ar)}} \cdot \frac{[Ar] \cdot A_A}{A_{Ar}}$$

where:

f_X = response factor of species X

$[X]$ = concentration/molar flow rate of species X

A_X = area of species X in the TCD spectrum

$f_{Xf(Ar)}$ = response factor of species X as a function of Ar

Due to the very low conversion levels in the present study, only the CO_2 quantification was conducted via the GC-TCD while hydrocarbons selectivities as well as the CO conversion was calculated based on the formation rates obtained from gas chromatography – flame ionisation detector (GC-FID) analysis (see section 4.5.2.2).

Table 4-1: Conditions for GC-TCD

	Column 1	*Column 2*	*Column 3*
Detector	TCD	TCD	TCD
Column Type	20 m MS5A	10 m PPQ	10 m MS5A
Carrier Gas	H_2	H_2	N_2
Flowrate (mL (NTP)/min)	30	30	30
Analysis Temperature (°C)	80	50	80
Inlet pressure (kPa)	150	80	150
Injection time (ms)	300	80	80
Injector temperature (°C)	100	100	100
Backflush time (s)	120	n/a	120
Analysis time (s)	180	180	180

4.5.2.2 Gas chromatography – flame ionization detector (GC-FID) analysis

Product gas from the FTS system collected in ampoules at various time intervals was analysed using a GC coupled to a flame ionization detector (Varian 3900). The gas was either manually injected into the instrument using a Hamilton syringe or the entire ampoule was placed in a sealed nitrogen filled ampoule breaker and mechanically crushed using a hydraulic system. The contained gas was subsequently introduced into the injector of the gas chromatograph (see Figure 4-7). The added neohexane in Ar (0.1061 %) was used as an internal standard for quantification purposes. Details of the GC-FID

instrument and conditions can be seen in Table 4-2.

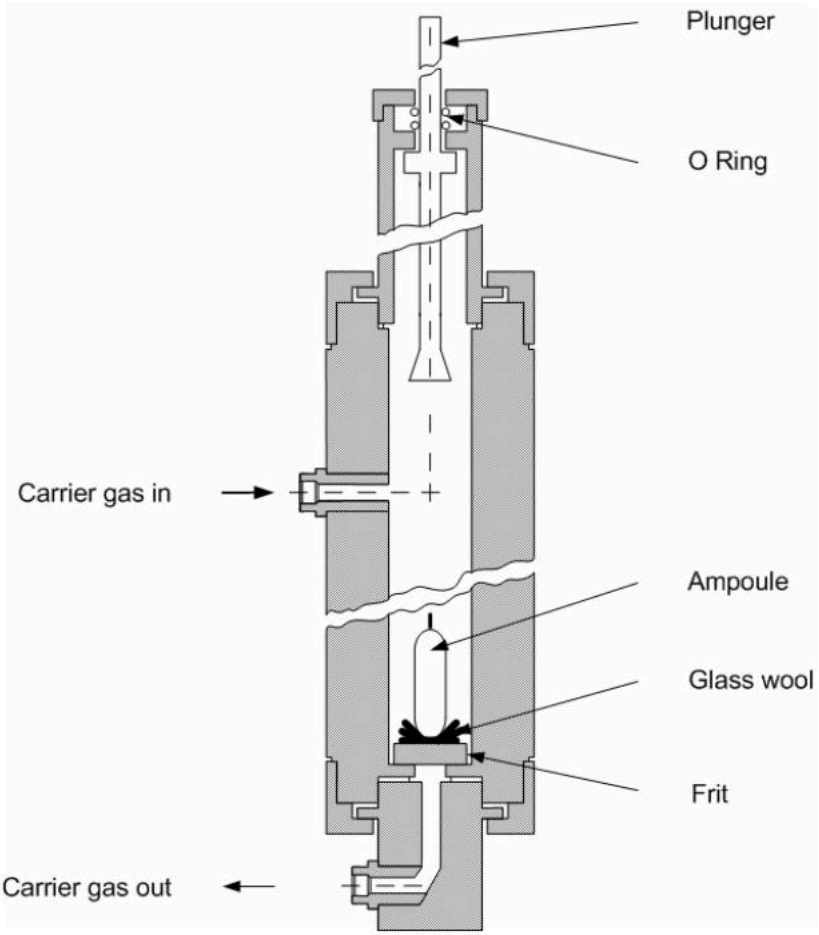

Figure 4-7 Configuration of Ampoule Breaker. (From Cairns.)[172]

Table 4-2: Conditions for GC-FID

Gas Chromatograph	*Varian 3900*
Detector	FID
Column Type	Varian capillary column, CP-Sil 5CB 25m 0.15mm 2µm #CP7692
Detector and Injector Temperature	250 °C
Ampoule Breaker Temperature	180 °C
Injector	Split Injector Split Ratio: Splitless to 1:7 depending on sample
Carrier Gas	H_2 (30 mL·min^{-1})
Introduction Gas	N_2 (25 mL·min^{-1})
Coolant	CO_2
Duration of analysis	29.89 min

Temperature Program

Rate (°C/min)	Step (°C)	Total Time (min)
initial	-55	1.5
20	0	4.25
14	100	11.39
10	280	29.89

The response factors for the different hydrocarbon species and oxygenates were calculated by the increment method published by Kaiser.[175] For each organic species i detected by the GC-FID, a response factor f_i was calculated using Equation 4-8. The molar flowrates, n_i of each species were then determined using Equation 4-9 and this was multiplied by the number of carbon atoms in the compound (N_i) to get n_{iC}, the molar flow rate of the compound on a carbon basis (Equation 4-10). The identification of each species was determined by comparison with known product spectra (an example of which can be seen in Figure 4-8) and by approximate identification via Kováts' indices for each compound.[176]

Equation 4-8

$$f_i = \left(\frac{N_{C,i}}{N_{C(noO)} + 0.55\left(N_{C(CO)}\right)}\right)$$

Equation 4-9

$$n_i = \left(\frac{N_{standard}}{N_i}\right) \cdot \left(\frac{f_i A_i}{f_{standard} A_{standard}}\right) \cdot n_{standard}$$

Equation 4-10

$$n_{iC} = N_{standard} \cdot \left(\frac{f_i A_i}{f_{standard} A_{standard}}\right) \cdot n_{standard}$$

where:

f_i = response factor for compound i

$N_{C,i}$ = total number of carbon atoms in compound i

$N_{C(noO)}$ = number of carbon atoms without bonds to oxygen atoms

$N_{C(CO)}$ = number of carbon atoms with a single bond to an oxygen atom

$N_{standard}$ = number of carbon atoms in internal standard (= C_6)

N_i = number of carbon atoms in compound i

n_i = molar flowrate of compound i

A_i = peak area of compound i in the chromatogram

$A_{standard}$ = peak area of internal standard in the chromatogram

$n_{standard}$ = molar flowrate of internal standard

$f_{standard}$ = response factor for internal standard from Equation 4-8 (= 1)

n_{iC} = molar flowrate of compound I on a carbon basis

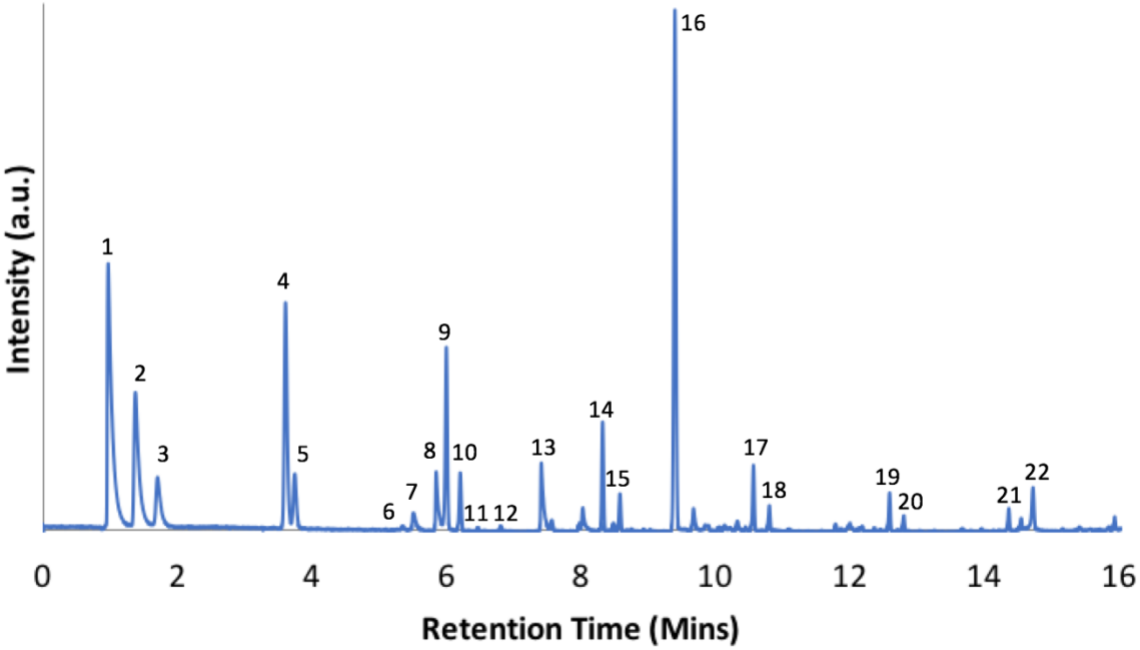

Figure 4-8 A typical GC-FID chromatogram showing FT products with the major peaks numbered: 1 – methane, 2 – ethene, 3 – ethane, 4 – propene, 5 – propane, 6 – ethanal, 7 – 2-me-propane, 8 – methanol, 9 – n-butene(1), 10 – n-butane(1), 11 – t-butene, 12 – c-butene, 13 – ethanol, 14 – n-pentene(1), 15 – n-pentane(1), 16 – neohexane, 17 – n-hexene(1), 18 – n-hexane(1), 19 – n-heptene(1), 20 – n-heptane(1), 21 – n-octene(1), 22 – n-octane(1).

4.5.2.3 Data processing of GC-TCD and GC-FID results

The CO conversions were calculated via the formation rates obtained from GC-FID. Agilent Technologies Galaxie Chromatography Software V1.10.0.5590 was used to analyse all GC products.

The molar flowrate of CO out of the reactor, $n_{CO,out}$ was calculated from the sum of the formation rates of the FT products using the GC-FID. The Anderson-Schulz-Flory[177] (ASF) 'plot' (see section 2.1.4) was created for each sample point. A single gradient relationship was assumed between carbon numbers 3 and 7 or 8 and a straight-line equation was determined (see Appendix A). This equation was used to extrapolate the molar flowrates of the species from carbon number 5 to 100. The total sum of the products was calculated from the addition of molar flowrates of carbon number 1 to 4, the extrapolated molar flowrates of carbon number 5 to 100 and the molar flowrate of CO_2 produced

(acquired from the GC-TCD) and used to determine the CO conversion (see Equation 4-11).

Equation 4-11

$$X_{CO} = \frac{\sum_1^{100} n_{iC} + n_{CO_2}}{n_{CO,in}}$$

where:

X_{CO} = conversion of CO

$n_{CO,in}$ = molar flowrate of CO into the reactor

n_{CO_2} = molar flowrate of CO_2 produced

n_{iC} = molar flowrate (carbon based) of FT products with carbon number i

The yield of compound i is expressed in Equation 4-12 and can be multiplied by the carbon number of compound i to get the yield on a carbon basis (Equation 4-13).

Equation 4-12

$$Y_i = \frac{n_i}{n_{CO,in}}$$

Equation 4-13

$$Y_{i,C} = \frac{n_{i,C}}{n_{CO,in}}$$

where:

Y_i = yield of compound i

$n_{CO,in}$ = molar flowrate of CO into the reactor

n_i = molar flowrate of compound i

n_{iC} = molar flowrate of compound i on a carbon basis

$Y_{i,C}$ = yield of compound I on a carbon basis

The selectivity of compound i is expressed in Equation 4-14 and multiplied by the carbon number of compound i to get this on a carbon basis (Equation 4-15).

Equation 4-14

$$S_i = \frac{Y_i}{X_{CO}}$$

Equation 4-15

$$S_{i,C} = \frac{Y_{i,C}}{X_{CO}}$$

where:

Y_i = yield of compound i

X_{CO} = conversion of CO

S_i = selectivity of compound i

$S_{i,C}$ = selectivity of compound i on a carbon basis

$Y_{i,C}$ = yield of compound I on a carbon basis

The chain growth probability ($\boldsymbol{\alpha}$) was calculated as the antilog of the gradient of the ASF plot. All error bars for values of conversions, selectivities and chain growth probabilities were determined as the positive and negative standard deviation of value for one time point determined in triplicate. For the products of carbon number 1 to 5, the olefin/paraffin ratios were determined from the quotient of the sum of the molar flowrates of all the olefins of a specific carbon number and the sum of the molar flowrates of the paraffins of that carbon number (Equation 4-16). The selectivity from hydrocarbons was determined from the hydrocarbon pool of products in order to best compare values independent of the influence of CO_2.

Equation 4-16

$$\frac{O}{P}\ ratio = \frac{\sum n_{C_i,C\ (olefins)}}{\sum n_{C_i,C\ (paraffins)}}$$

where:

$n_{C_i,C\ (olefins)}$ = molar flowrate of compound with carbon number i on a carbon basis

$n_{C_i,C\ (paraffins)}$ = molar flowrate of compound with carbon number i on a carbon basis

5 RESULTS AND DISCUSSION

5.1 Characterization before and during syntheses

5.1.1 Particle size distribution

The particle size distribution of the starting materials (calcium and aluminium hydroxide) used to synthesise the C12A7 and subsequently the C12A7:e^- compounds was measured as received and after milling (see section 4.1.1). Each sample was measured 5 times and an average value of the obtained distributions was calculated (see Figure 5-1). The particle size distribution of $Al(OH)_3$ is monomodal with the highest distribution of particles by % of total volume, having particle size between 20 and 30 μm and an average particle size of *ca.* 23 μm. All particles are larger than *ca.* 0.2 μm and smaller than *ca.* 200 μm. The distribution of $Ca(OH)_2$ is similarly monomodal with generally smaller particles than $Al(OH)_3$; average particle size of *ca.* 50 μm with a lowest size of *ca.* 0.3 μm and a largest size of *ca.* 400 μm.

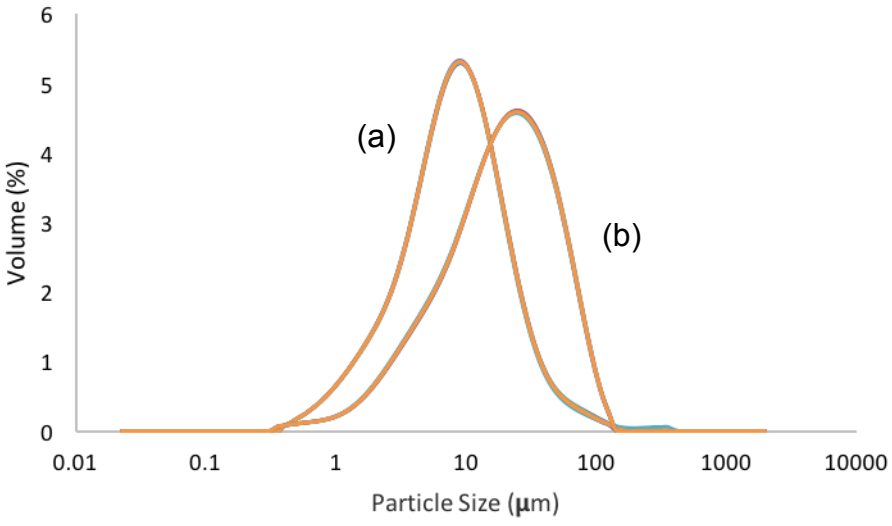

Figure 5-1 Average particle size distribution of (a) $Al(OH)_3$ and (b) $Ca(OH)_2$

After milling as an aqueous slurry (see section 4.1.1 for details), the particle size distribution was re-measured (see Figure 5-2). While the aim of the treatment was to generate an even particle size distribution for the two materials, a multimodal particle size distribution is observed. The lower size

detected in the mixture is *ca.* 0.2 μm and the upper *ca.* 400 μm. The average measurement is not superimposable on the individual measurements as before the milling. The milling was observed to change the average size distribution and allows for a more homogenous mixture. This can be assumed to be an advantage over a bimodal distribution of the stoichiometric addition of the starting materials due to the minimisation of the aggregation of similarly sized particles.

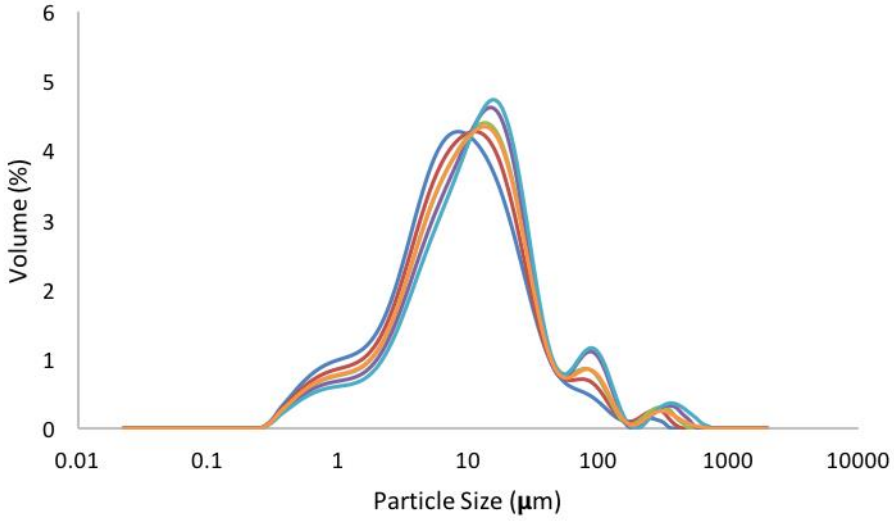

Figure 5-2 Particle size distribution of $Ca(OH)_2$ and $Al(OH)_3$ slurry after micronizing. Each colour plot represents a different measurement, with the average plot represented centrally in the colour orange.

5.1.2 Thermogravimetric analysis (TGA) and differential scanning calorimetry (DSC)

The decomposition of the iron precursor $Fe(acac)_3$ in air and Ar was studied with TGA-DSC (see Figure 5-3). The decomposition of the material under both conditions is similar with a first exothermic weight loss event around 140 °C (slightly lower onset for treatment in Ar). Literature[178–181] suggests this decomposition to correlate to the partial decomposition of acetylacetone ligands. It can be accepted that the cleavage of the acetylacetone groups may result in the formation of CO_2.[180] Decomposition under air flow with increasing temperature facilitates the bulk loss of the organics present and occurs

gradually with the partial loss of these components associated with narrow DSC exotherms and a broad DSC exotherm. Under Ar flow, the organic decomposition occurs in two major steps leading to the supposed decomposition of the ligands to CO_2.[178,182,183] This decomposition is associated with a broad exotherm and would have a larger heat of fusion under Ar flow. Complete decomposition to a residual iron(II) oxide species was observed at 670 °C in both Ar and air. Although three distinct mass loss occurrences associated with the loss of each of acetylacetone ligand did not occur as suggested in the supplementary information by Sahu and co-workers[184] (see Figure 5-4), the cumulative weight loss of organics and residual component is comparable.

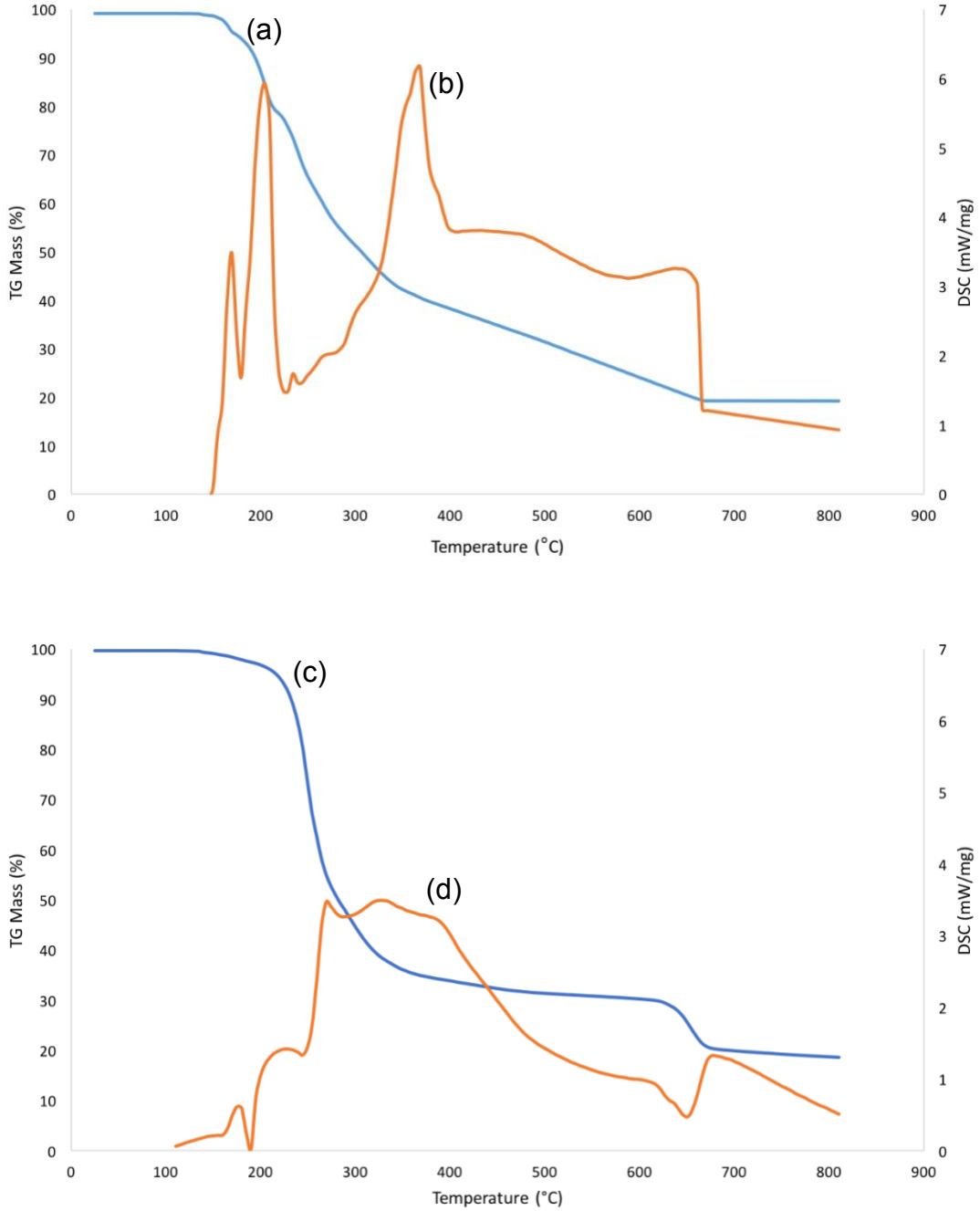

Figure 5-3 (a) TGA and (b) DSC profile of $Fe(acac)_3$ under 30 mL·min^{-1} air flow, (c) TGA and (d) DSC profile of $Fe(acac)_3$ under 30 mL·min^{-1} Ar flow.

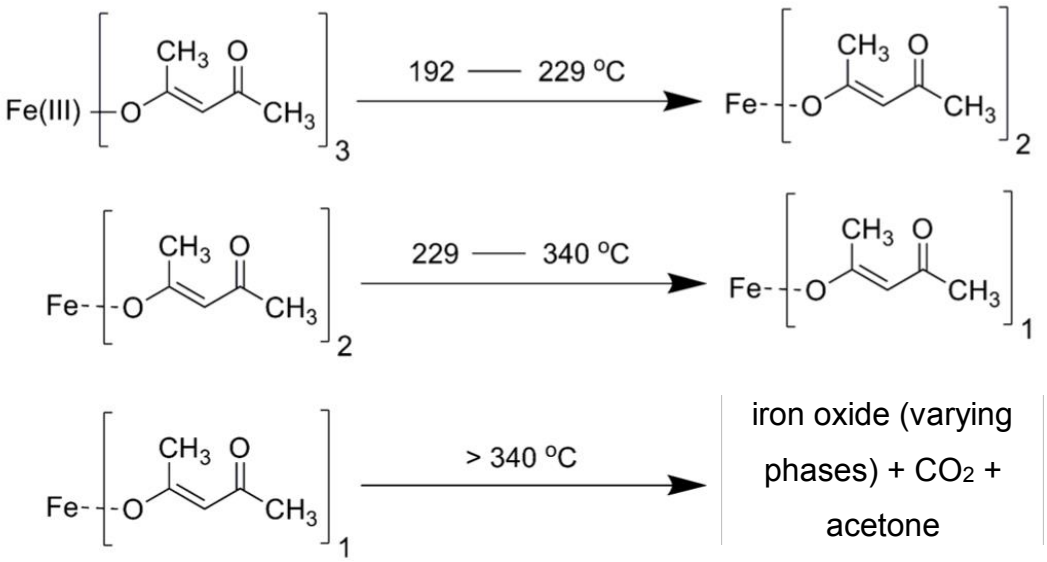

Figure 5-4 Suggested $Fe(acac)_3$ decomposition (Adapted from Sahu *et al.*)[184]

5.1.3 Powder X-ray diffraction (XRD)

Powder X-ray diffraction is used to follow the evolution of the crystal phases throughout the catalyst synthesis process starting with the calcium and aluminium precursors (see Figure 5-5). All XRD scans were normalised to the highest peak. While $Al(OH)_3$ appears to be poorly crystalline, $Ca(OH)_2$ corresponds well to the described reference pattern.

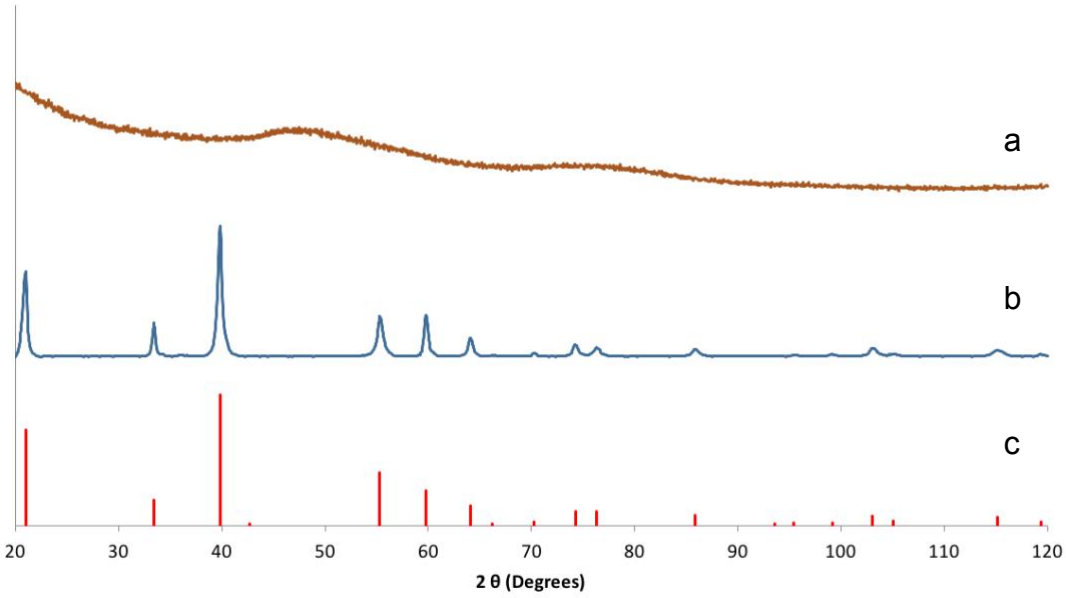

Figure 5-5 XRD Pattern of (a) aluminium hydroxide and (b) calcium hydroxide starting materials with reference pattern for (c) $Ca(OH)_2$

Following the hydrothermal treatment and drying (see section 4.1 for details), the XRD pattern shows a number of different reflexes with different shapes and widths, indicating the presence of multiple crystalline phases (see Figure 5-6). However, the observed pattern cannot be correlated to available reference patterns of the hydroxide precursors, mayenite or CaO. At this stage, the structure is unknown.

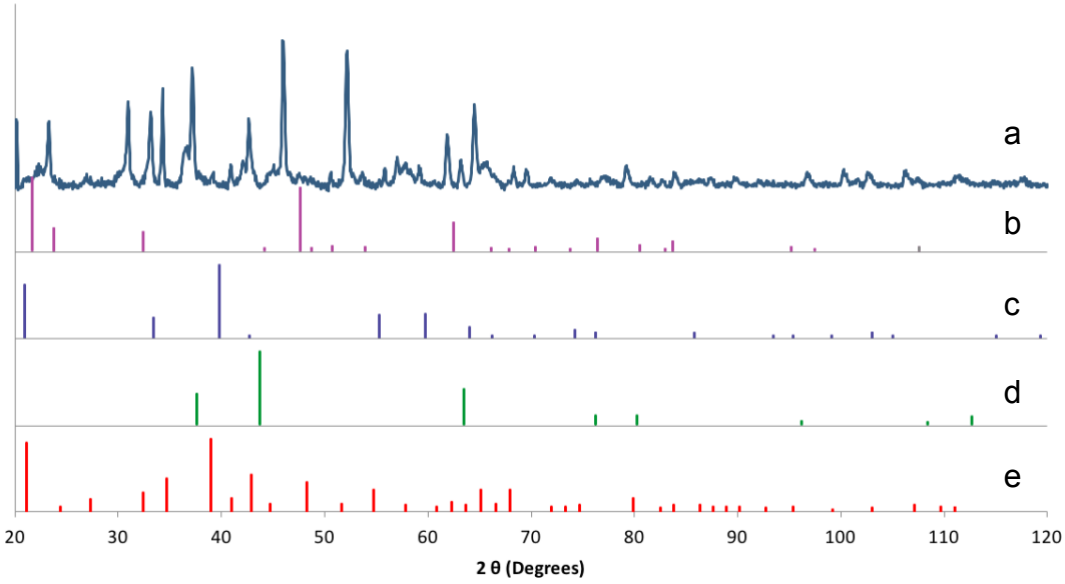

Figure 5-6 XRD pattern of (a) calcium-aluminium hydroxide mixture after autoclave step with reference patterns for (b) $Al(OH)_3$, (c) $Ca(OH)_2$, (d) CaO and (e) C12A7.

Upon calcination in air at 600 °C for 5 h, the presence of mayenite is evidenced in conjunction with CaO (see Figure 5-7). CaO present is believed to form from a side dehydration reaction of $Ca(OH)_2$.[185,186]

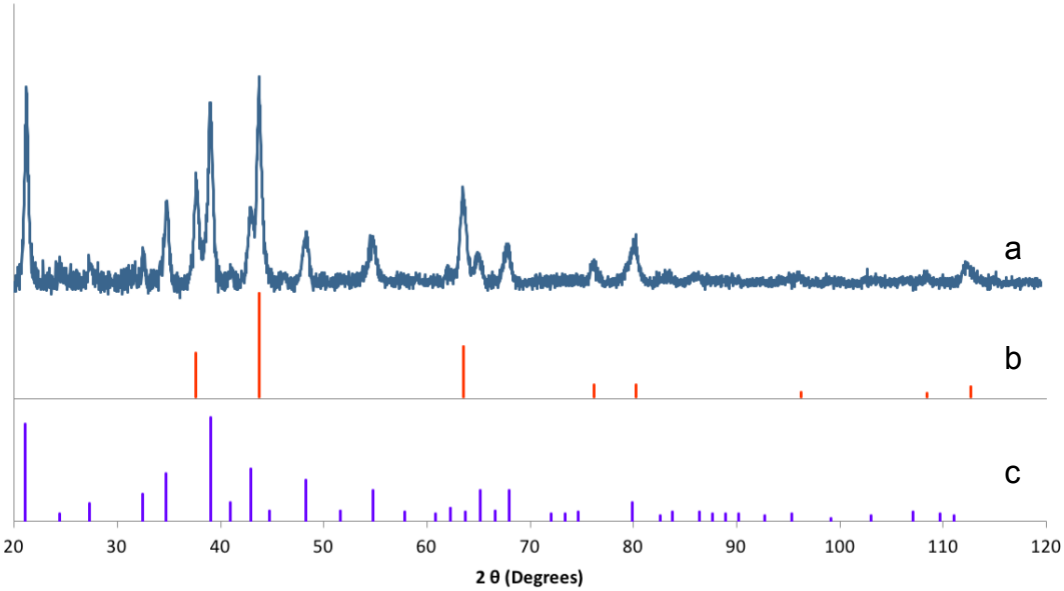

Figure 5-7 XRD pattern of (a) C12A7 (mayenite) powder with reference patterns for (b) CaO and (c) C12A7.

After high temperature (800 °C and 1000 °C) treatment under vacuum (1 x 10^{-4} Pa) and reduction by CaH_2, the obtained electride materials were again studied with XRD (see Figure 5-8). Compared to the mayenite phase after calcination in air (Figure 5-7), little difference in the present diffraction patterns can be observed. Both the 800 °C and 1000 °C electrides show the mayenite as well as CaO structures.

The crystallite size of each containing compound within the studied samples was calculated using the Scherrer equation based on the individual diffraction peaks listed in Table 5-1. The crystallite size of CaO in all supported catalysts was similar (slightly higher in the mayenite compound) to each other suggesting most of its formation during identical conditions – during the initial calcination in air (see section 4.1.1). The increase in concentration of CaO in the electride compounds can be associated to the reaction of the CaH_2 to CaO during reduction of the mayenite. The electride materials displayed a grey colour as opposed to the opaque white colour of its mayenite precursor. This shows a similarity with the white to black colour change reported in literature.[2] The grey shade observed is attributed to the dilution of electride with (white) CaO and/or incomplete reduction of the C12A7 precursor. The crystallite size of the mayenite shows an increasing trend with dehydrated calcination and the subsequent increase in temperature of the dehydrated calcination. These values and their trend is in agreement with Inoue *et al*. and is significantly smaller than the average crystallite size of the their reported solid-phase synthesised mayenite powder.[2]

In the case of the 1000 °C electride, the XRD pattern showed an additional compound, tricalcium aluminate ($3CaO{\cdot}Al_2O_3$). Under the high temperature treatment, the crystal structure of the mayenite may collapse forming the aluminate or it is the product of the over-stoichiometric addition of CaH_2. This occurrence was also reported for the 1000 °C electride synthesised by Inoue and co-workers supplementing the notion that the mayenite construction is partially destroyed at the higher evacuation temperature.[2] The crystallite size of this compound is slightly larger than the mayenite framework and may be more agglomerated.

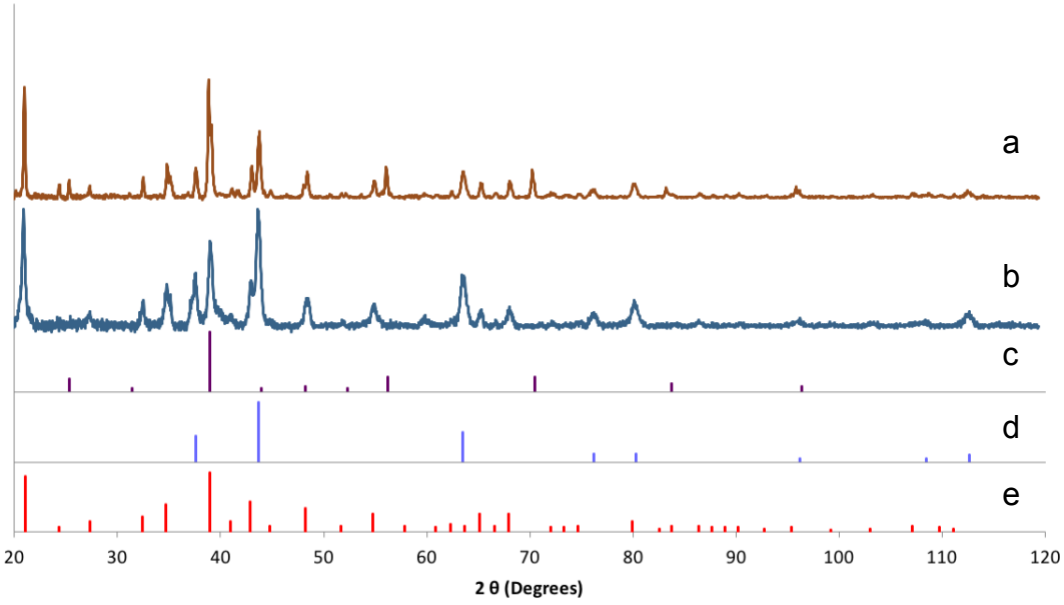

Figure 5-8 XRD pattern of C12A7:e$^-$ compounds produced at the (a) 800 °C and (b) 1000 °C evacuation temperatures with reference patterns for (c) $3CaO{\cdot}Al_2O_3$, (d) CaO and (e) C12A7.

Table 5-1 Crystallite size for an individual plane of each containing material within the mayenite and electride compounds

Sample	*Compound*	*2θ*	*Plane*	*Crystallite size (Å)*
C12A7	C12A7	21.080	2 1 1	255.5
	CaO	76.215	3 1 1	306.7
C12A7:e$^-$ (1000 °C)	C12A7	65.122	6 4 0	369.0
	CaO	63.512	2 2 0	248.9
	$3CaO{\cdot}Al_2O_3$	69.974	8 4 4	452.2
C12A7:e$^-$ (800 °C)	C12A7	21.080	2 1 1	357.4
	CaO	37.601	1 1 1	257.2

Due to the crystallinity of the mayenite structure, the phase of the iron oxide supported on it could not be determined by XRD. As proxy for the mayenite/electride support, amorphous SiO_2 spheres, so called Stöber spheres[164], were employed for the sole purpose of studying the decomposition product of $Fe(acac)_3$ after different treatments. At 400 °C, the samples, i.e. a physical mixture of $Fe(acac)_3$ and SiO_2, were exposed to stagnant air, a

continuous air flow, stagnant Ar and a continuous flow of Ar for 2 h. All four treatments yielded Fe^{3+} oxides in conjunction with the SiO_2 species (see Figure 5-9). While stagnant atmospheres as well as a constant flow of Ar resulted in the formation of FeO(OH), a flow of air yielded hematite – **α**-Fe_2O_3. As hematite is the common form of calcined precipitated iron catalysts (see section 5.2.1), the treatment in a flow of air was chosen for the decomposition of the $Fe(acac)_3$ precursor.

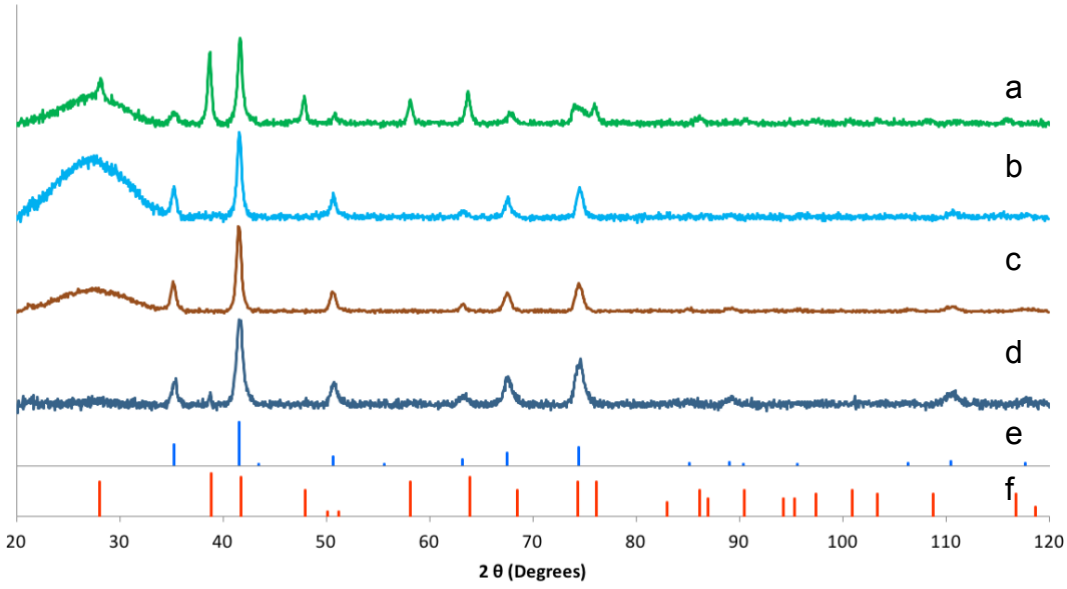

Figure 5-9 XRD pattern of the iron loaded silica spheres[164] produced under (a) continuous air flow, (b) continuous Ar flow, (c) stagnant Ar and (d) stagnant air with reference patterns for (e) FeO(OH) and (f) hematite.

The XRD diffractograms provide significant evidence that all support materials intended for metal deposition were synthesised. However, the quantity of side products present in each was not determined. Although XRD evidence cannot distinguish between the mayenite and electride compounds due to its identical peak pattern, it can confirm that the stability of the mayenite structure is retained through synthesis (see section 5.2.1) and catalysis (see section 5.3.1).

5.1.4 Transmission electron microscopy (TEM)

Elemental analysis via energy-dispersive X-ray spectroscopy coupled to TEM (EDS-TEM) allowed for an indication of the stoichiometry and composition of certain areas of focus on TEM micrographs of the pre-calcined hydroxide mixture and the subsequent air-calcined mayenite material. The electron beam was directed at the encircled regions of the micrographs (see Figure 5-10) and allowed for an estimated identification or elimination of certain species that may be present within the structures based on their elemental weight percentage (see Table 5-2). At a magnification with a 200 nm scale, the elemental analysis of the hydroxide mixture with the EDS beam directed at the encircled section (Figure 5-10a) shows an elemental composition of Ca, Al and O in a close relation to the theoretical stoichiometric weight % composition needed to form the mayenite compound (Table 5-2). This is a good indication that the stoichiometry is correct but does not indicate the type of species present. However, at further magnification of the chosen section of the sample observed with a 50 nm scale (Figure 5-10b), the weight % observed favours Al and O, indicating a separation of the Ca element and a clear notion that the mayenite structure has not been formed or is not present in the assembly studied. As this assembly is consistent throughout the sample and lacks substantial Ca content to form the mayenite construction, its morphology may be ruled out as the mayenite compound in the subsequent micrographs.

A focus of the EDS beam on the rod-like flakes along the edge and the agglomerated centre of the C12A7 sample at a magnification observed on a 200 nm scale (Figure 5-10c and d respectively) showed two unique elemental compositions. When the area of focus is the centre of the sample, the composition of Ca, Al and O is closer to the theoretical composition of C12A7. However, the flakes observed along the edges of the specimen have a low composition of Ca. Further EDS analysis of the flake-like complex at a higher magnification observed on a 100 nm scale confirmed the low Ca content. Although aluminium oxides were not found in the sample at high enough intensities via XRD analysis, the high Al and O content of these flake-like structures may indicate their presence as an amorphous phase.

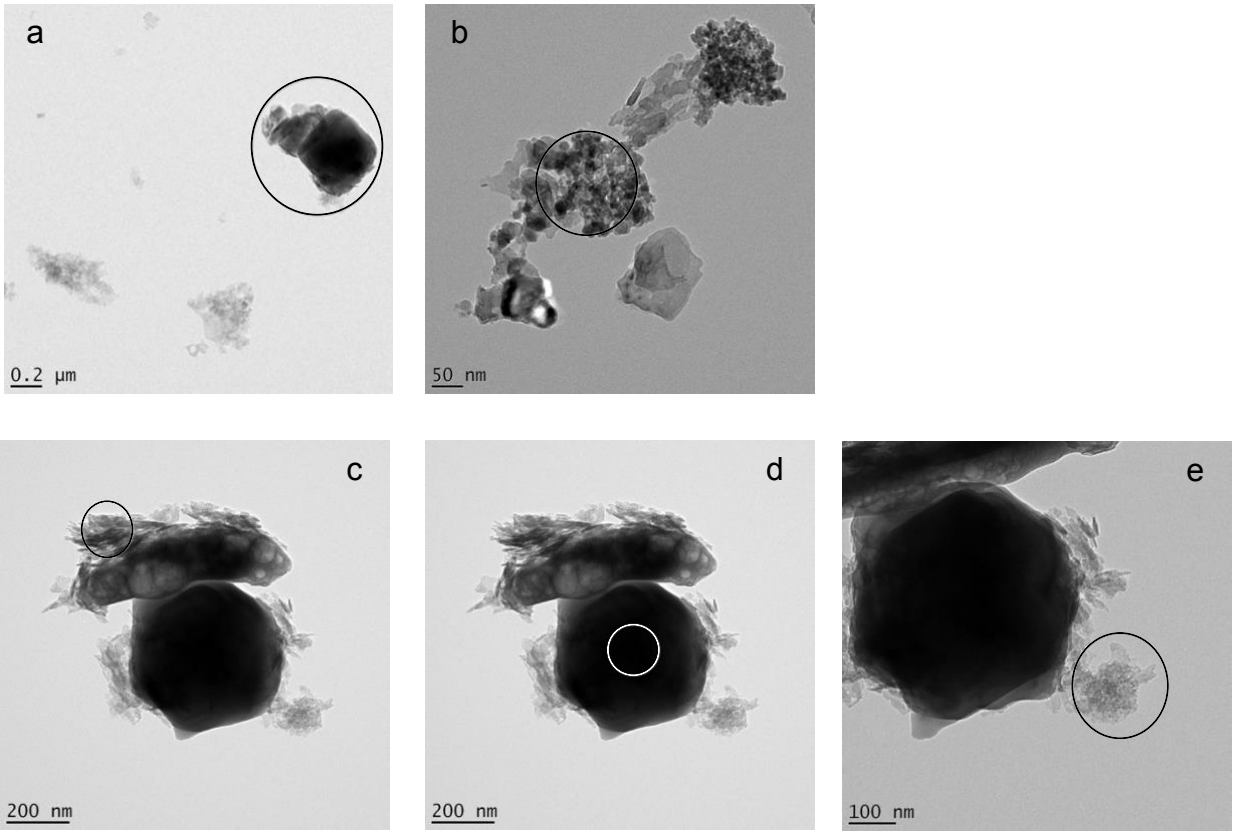

Figure 5-10 TEM of (a) Ca-Al hydroxide mixture with 200 nm scale, (b) Ca-Al hydroxide mixture with 50 nm scale, (c) C12A7 with 200 nm scale, (d) C12A7 with 200 nm scale and (e) C12A7 with 100 nm scale with the area of focus by the EDS beam encircled in each micrograph.

Table 5-2 Theoretical elemental analysis and calculated elemental analysis of the encircled areas in Figure 5-10

Compound	*Theoretical Element Weight %*		
	Ca	Al	O
C12A7	34.68	27.24	38.08
CaO	71.47	0	28.53
Al_2O_3	0	52.92	47.08
Area of Focus	*Observed Element Weight % (Uncertainty)*		
	Ca	Al	O
Figure 5-10 a	33.94 (0.21)	20.35 (0.16)	45.69 (0.34)
Figure 5-10 b	3.37 (0.09)	40.15 (0.23)	56.46 (0.38)
Figure 5-10 c	5.41 (0.12)	45.97 (0.30)	48.61 (0.43)
Figure 5-10 d	46.36 (0.27)	17.65 (0.17)	35.97 (0.35)
Figure 5-10 e	8.32 (0.32)	44.34 (0.57)	47.33 (0.92)

The flake-like morphology was observed to diminish in the standard TEM micrographs from the pre-calcined Ca-Al hydroxide mixture to the mayenite and electride compounds at a magnification showing a 100 nm scale (Figure 5-11) and a 50 nm scale (Figure 5-12). Aluminates or other side products may be represented by the rod like structures present.

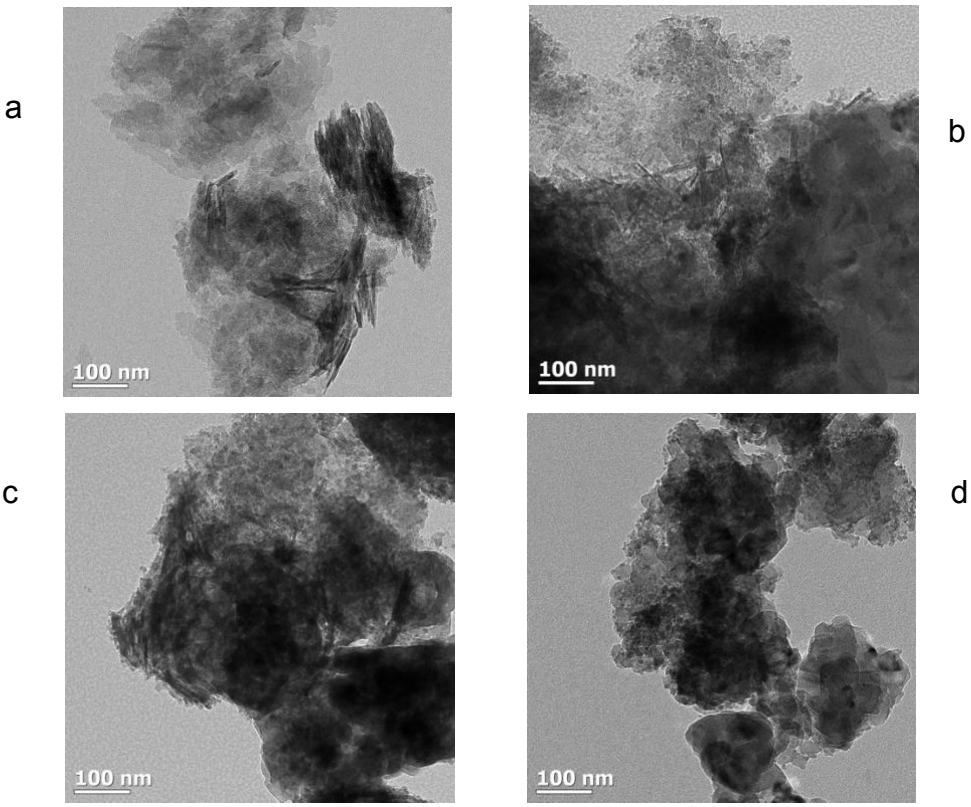

Figure 5-11 TEM at a magnification with 100 nm scale observed of (a) Ca-Al Hydroxide Mixture, (b) C12A7, (c) C12A7:e^- (800 °C) and (d) C12A7:e^- (1000 °C)

The morphologies observed of the mayenite and electride compounds is largely consistent and clearly layered (apparent from the darker textures due to higher agglomerations). The layered structures can be seen to increase in size between the mayenite and the electrides. This observation can be substantiated by the XRD analysis of these compounds which indicate the presence of the mayenite phase with a trend of increasing crystallite size between the mayenite and electrides. Apart from this size variation, the morphology of the crystalline cages within the mayenite and electride compounds are expected to remain unchanged, similar to the XRD pattern of the mayenite throughout synthesis.

It remains relatively uncertain whether the morphology of CaO shown to be present via XRD is visible in the TEM micrographs. However, if the observed trend suggesting a decrease in CaO crystallite size from mayenite to electride is to be believed, the major structural morphologies observed in the TEM micrographs show little evidence of a decrease in size. This could eliminate their identification as CaO.

Tricalcium aluminate believed to be present in the C12A7:e^- (1000 °C) sample from XRD analysis was also not identified under TEM analysis as its unknown morphology was not strikingly present in the sample opposed to its 800 °C electride counterpart.

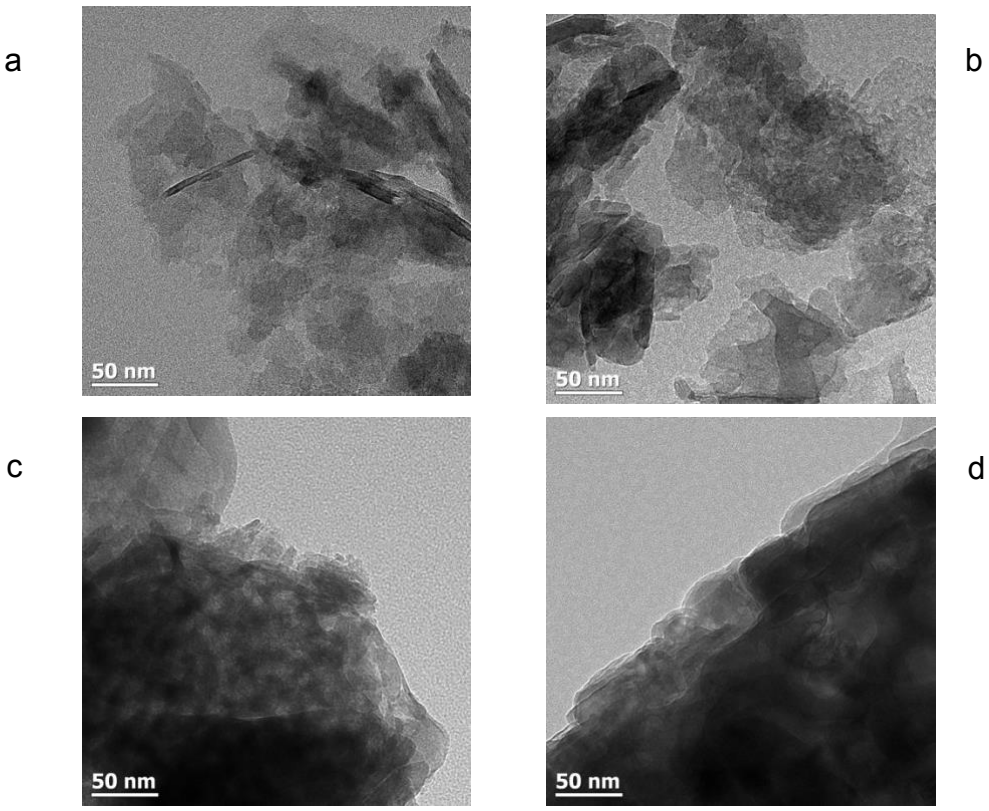

Figure 5-12 TEM at a magnification with 50 nm scale observed of (a) Ca-Al Hydroxide Mixture, (b) C12A7, (c) C12A7:e^- (800 °C) and (d) C12A7:e^- (1000 °C).

5.2 Characterisation of iron catalysts

5.2.1 Powder X-ray diffraction (XRD)

The XRD of the calcined unpromoted precipitated iron control catalyst can be seen in Figure 5-13 before dilution with Puralox (**γ**-alumina). The calcination yielded hematite or **α**-Fe_2O_3. A very crystalline and low background scan was observed indicating little to no side products or alternate iron oxide phases present.

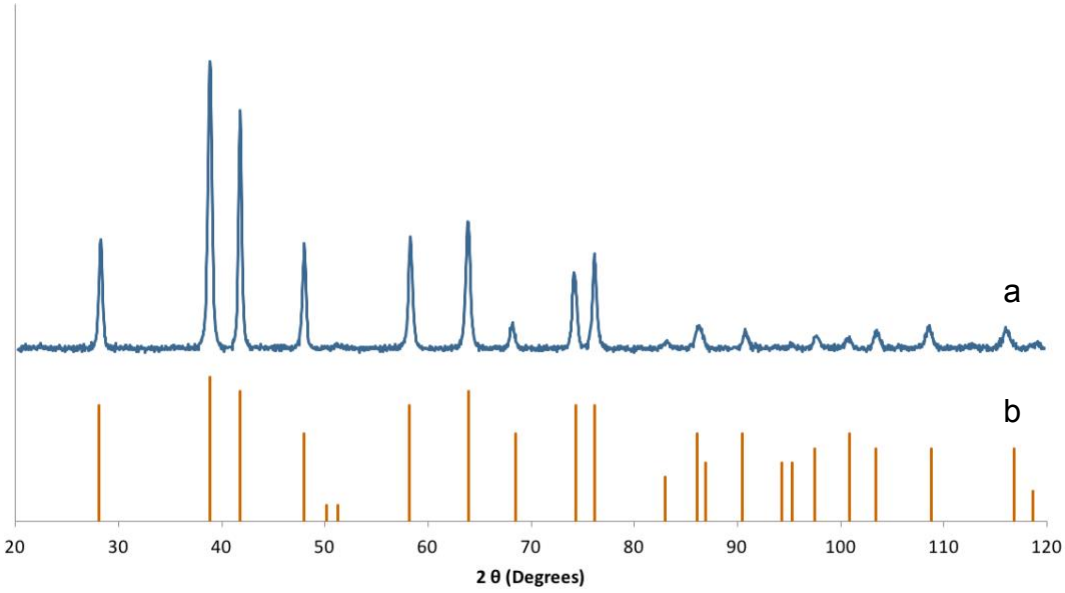

Figure 5-13 XRD pattern of (a) the unpromoted precipitated iron control/baseline catalyst before dilution with Puralox (γ-alumina) with the reference pattern for (b) hematite iron phase.

After a target 10 wt. % of iron was loaded under identical conditions on the mayenite and electride compounds, the fresh supported catalysts were studied via XRD (see Figure 5-14). All three of the final supported catalysts were observed to have the mayenite framework present. The 1000 °C electride retained the presence of $3CaO{\cdot}Al_2O_3$ and to a much lower extent, CaO. The CaO from the previous unloaded supports was shown to be present in the Fe-C12A7 and Fe-C12A7:e^- (800 °C) catalysts only in trace amounts. This is believed to be due to its conversion to $CaCO_3$. All final supported catalysts indicated a presence of $CaCO_3$ due to reaction of the synthesis side product CaO, and CO_2, a product of acetylacetonate decomposition. As the Fe

decomposed onto the supports was of a low intensity, it was not possible to determine the iron oxide or carbide phases present on the supported catalysts via XRD analysis and its presence was confirmed by other means (ICP-OES/AAS and XPS).

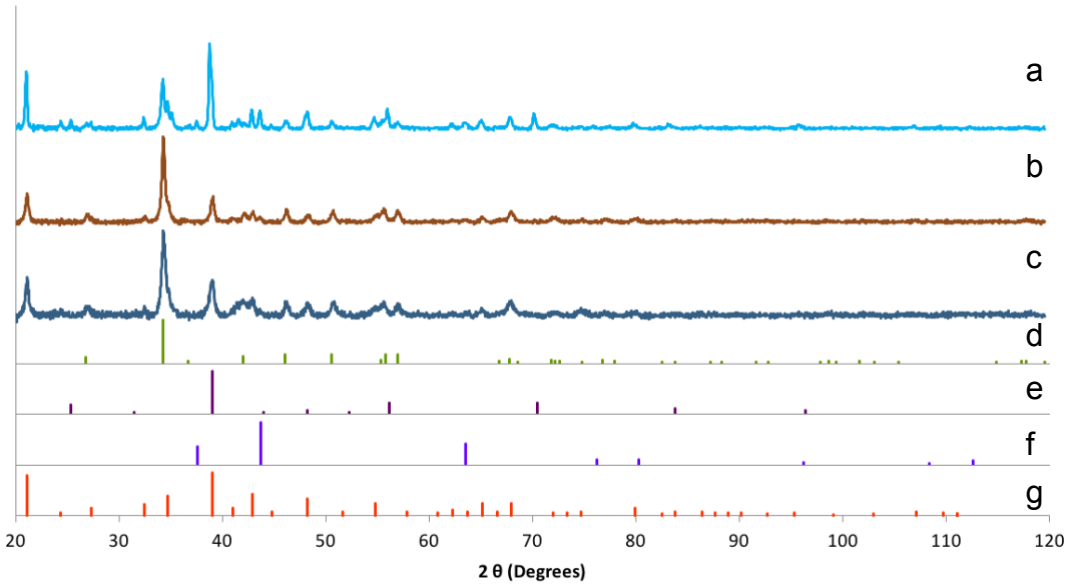

Figure 5-14 XRD pattern of the supported iron catalysts: (a) Fe-C12A7, (b) Fe-C12A7:e^- (1000 °C) and (c) Fe-C12A7:e^- (800 °C) with reference patterns for (d) $CaCO_3$, (e) $3CaO{\cdot}Al_2O_3$, (f) CaO and (g) C12A7.

The crystallite size of the mayenite framework is shown to increase upon deposition of iron particles onto the supports for all supported catalysts (see Table 5-3).

As most of the CaO present in the compounds was converted to $CaCO_3$, it's crystallite size was only possible to be calculated for Fe-C12A7:e^- (1000 °C) showing an approximate two fold increase in size. This CaO present in a low concentration may have been aggregated or shielded under deposition conditions preventing its conversion to $CaCO_3$. The newly formed $CaCO_3$ however was observed to be within a small size range for all the supported catalysts due to its formation at identical conditions. The crystallite size of the tricalcium aluminate in Fe-C12A7:e^- (1000 °C) remained around the same size

after iron deposition suggesting that the deposition conditions had little effect on it.

Table 5-3 Crystallite size for an individual plane of each containing material within the fresh catalysts

Sample	*Compound*	*2θ*	*Plane*	*Crystallite size (Å)*
Fe-C12A7	C12A7	21.080	2 1 1	282.2
	CaO	N/A (too low intensity)		
	$CaCO_3$	46.091	1 1 3	232.7
Fe-C12A7:e⁻ (1000 °C)	C12A7	21.080	2 1 1	509.2
	CaO	37.601	1 1 1	482.5
	$CaCO_3$	56.411	1 1 6	316.7
	$3CaO{\cdot}Al_2O_3$	25.328	3 2 1	464.8
Fe-C12A7:e⁻ (800 °C)	C12A7	21.080	2 1 1	486.7
	CaO	N/A (too low intensity)		
	$CaCO_3$	46.091	1 1 3	233.5

5.2.2 Transmission electron microscopy (TEM)

TEM analysis after decomposition of the iron precursor yielding iron-based compounds supported on the mayenite and electride materials at a magnification with a 100 nm scale (Figure 5-15) and 50 nm scale (Figure 5-16) largely suggest evidence of spherical black particles dispersed across their surfaces. These particles are believed to be the calcined iron oxide particles, and although agglomerated in parts of the micrograph samples, are observed in even quantities across the samples. The fresh catalysts have retained the structures and morphologies of the unsupported support systems (section 5.1.4) with the flakey rod-like structures originally observed in the Ca-Al hydroxide mixture present in marginal quantities if observed.

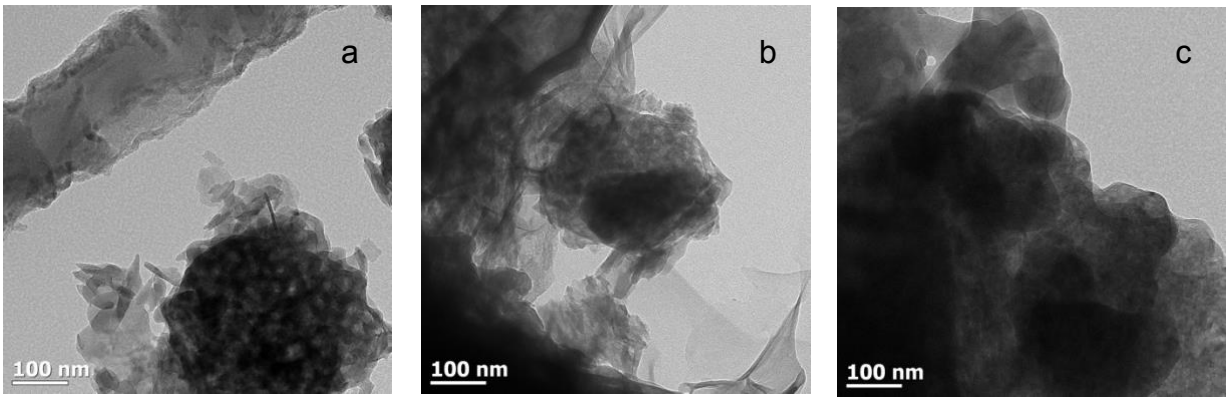

Figure 5-15 TEM at a magnification with 100 nm scale of (a) Fe-C12A7, (b) Fe-C12A7:e^- (800 °C) and (c) Fe-C12A7:e^- (1000 °C)

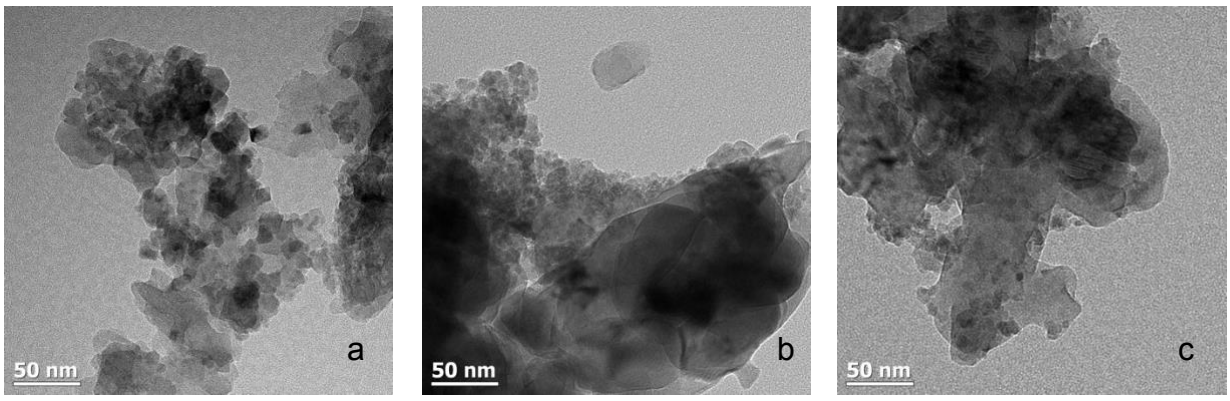

Figure 5-16 TEM at a magnification with 50 nm scale of (a) Fe-C12A7, (b) Fe-C12A7:e^- (800 °C) and (c) Fe-C12A7:e^- (1000 °C)

5.2.3 BET physisorption

The BET surface areas of each of the Fe-loaded electride and mayenite catalysts were calculated after analysis of their N_2 physisorption behaviour (see Table 5-4).

An expected decrease in catalytic surface area is observed from the mayenite catalyst, which was subjected to no evacuated calcination, to the electride catalysts exposed to 800 °C and 1000 °C evacuated calcinations respectively. The trend of decreasing surface area with evacuated calcination and furthermore the increased temperature of the evacuated calcination has

previously been reported in literature.[2] This occurrence is due to the aggregation of the mayenite nanoparticles and can be explained via the increase in density of the support particles in the TEM images of the catalysts in both before (most notably Figure 5-12 from b to d) and after (Figure 5-15 from a to c) iron deposition.

Table 5-4 BET surface area of iron-loaded mayenite and electride supports

Catalyst	*BET Surface Area ($m^2 \cdot g^{-1}$)*
Fe-C12A7	28
Fe-C12A7:e- (800 °C)	20
Fe-C12A7:e- (1000 °C)	16

5.2.4 Confirmation of iron loading

The target weight % loading of Fe on each of the electride and mayenite supports was chosen to be 10 % based on several literature LTFT studies.[28,187,188] The average loading was determined from the results of both ICP-OES and AAS techniques (see Table 5-5) and was relatively close to the target loading. This average loading was used in determining the amount of catalyst used for each testing run as the iron content was kept constant for each of the catalytic experiments.

Table 5-5 Fe loading onto support materials

Catalyst	*AAS Loading (wt. %)*	*ICP-OES Loading (wt. %)*	*Average Loading (wt. %)*
Fe-C12A7	9.18	9.10	9.14
Fe-C12A7:e- (800 °C)	9.31	9.08	9.20
Fe-C12A7:e- (1000 °C)	8.85	8.79	8.82

Both techniques yielded results in a close range of each other and may be considered fairly accurate under the assumption of complete catalyst digestion prior to analysis.

5.2.5 X-ray photoelectron spectroscopy (XPS)

The XPS analysis shows the spectral fitting of the Fe atom's 2p region for the iron supported electride evacuated at 1000 °C (see Figure 5-17). The Fe 2p spectra shows well resolved complex multiplet splitting and the presence of satellite features which suggests the iron compounds present to be high-spin, in turn indicating the presence of Fe(III) and/or Fe(II).[189]

The spectral fitting shows the Fe $2p_{\frac{3}{2}}$ peak at a binding energy (BE) of 710.7 eV with its satellite peak at 719.4 eV and the Fe $2p_{\frac{1}{2}}$ peak at 724.6 eV with its satellite peak at 733.3 eV. As the BE of the Fe $2p_{\frac{3}{2}}$ orbital peak for iron oxide is significantly shifted compared to metallic iron (706.7 eV)[190], the presence of metallic iron can be excluded. The Fe $2p_{\frac{1}{2}}$ peak may be further shifted for Fe(III) compared to Fe(II).

The presence of Fe(III) could indicate the iron phase hematite (**α**-Fe_2O_3), maghemite (**γ**-Fe_2O_3) and goethite (**α**-FeO(OH)). The presence of both Fe(III) and Fe(II) could indicate the iron phase magnetite (Fe_3O_4).

As internal standards to determine the BE's of pure iron oxide phase compounds were not obtained, a comparison of the results and literature BE peaks for the Fe 2p spectra of some of the most common iron oxide phases was conducted. This resulted in an increase in the uncertainty due to the inherent uncertainty of different analysis instruments. The first and second peak of the Fe 2p spectra reported in literature for some of these iron phases (see Table 5-6) which in most cases refers to the Fe $2p_{\frac{3}{2}}$ orbital and its satellite feature can be compared to the observed values in Figure 5-17.

The BE obtained for the first peak of the catalyst, 710.7 eV closely correlates with Grosvenor *et al*.'s BE for hematite, the most common iron phase in calcined samples.[191] However, a correlated similar value (BE of 710.6 eV) has also been determined for Fe_3O_4 by Yamashita *et al*.[192] It is known that surfaces of hematite are often found covered with a layer of magnetite.[28,193] The BE of 710.7 and 710.8 eV determined by Biesinger and co-workers[190] for their second hematite and maghemite peaks respectively is approximately the same as the first BE peak for the catalyst in this study which further suggests the presence of Fe(III) over Fe(II).

The iron deposition conditions chosen in section 4.2 based on trial depositions done on Stöber silica spheres showed predominantly hematite deposits in XRD (Figure 5-9, section 5.1.3) which is similarly expected to form in all supported catalysts in this study.

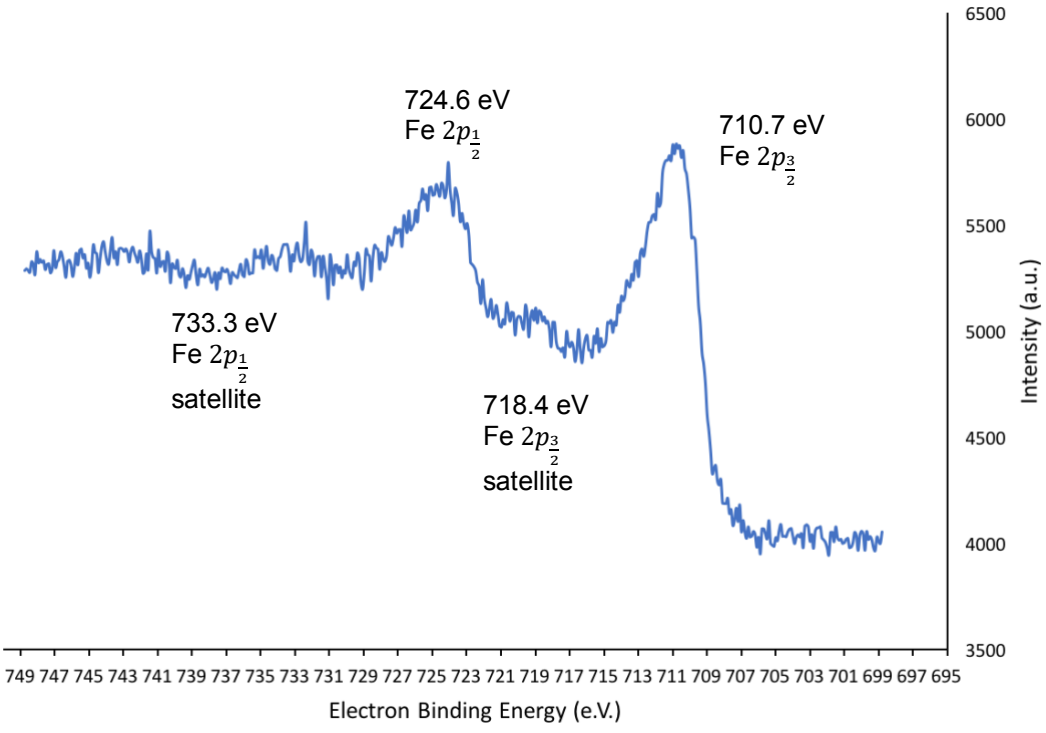

Figure 5-17 XPS analysis showing spectral fitting of 2p region for Fe-C12A7:e^- (1000 °C)

Table 5-6 Iron oxide phase compounds' binding energies from literature

Literature	*Iron Oxide Phase*	*Peak 1 (eV)*	*Peak 2 (eV)*
Grosvenor et al.[191]	Hematite (**α**-Fe_2O_3)	710.8	
	Maghemite (**γ**-Fe_2O_3)	711.0	
	Geothite (**α**-FeO(OH))	711.4	
	Magnetite (Fe^{3+})	711.4	
	Magnetite (Fe^{2+})	709.0	
Yamashita et al.[192]	Hematite (**α**-Fe_2O_3)	711.0	
	Magnetite (Fe_3O_4)	710.6	
Biesinger et al.[189]	Hematite (**α**-Fe_2O_3)	709.8	710.7
	Maghemite (**γ**-Fe_2O_3)	709.8	710.8
	Geothite (**α**-FeO(OH))	710.2	711.2
	Magnetite (Fe^{3+})	710.2	711.2
	Magnetite (Fe^{2+})	708.4	709.2

5.2.6 Temperature programmed reduction (TPR)

Temperature programmed reduction (TPR) was performed on each of the prepared supported catalysts. The TPR profiles of each catalyst show evidence of a two-step reduction (see Figure 5-18 b, d and f) with a clear shoulder at about *ca.* 480 °C and a prominent hydrogen consumption peak at *ca.* 600 °C. This behaviour hints on a reduction from hematite over magnetite to metallic iron. The two steps of reduction of the hematite iron phase (represented by Equation 5-1 and Equation 5-2) are attributed to the reduction of Fe(III) to Fe(II) and the subsequent reduction to metallic Fe.

Equation 5-1

$$3Fe_2O_3 + H_2 \rightarrow 2Fe_3O_4 + H_2O$$

Equation 5-2

$$Fe_3O_4 + 4H_2 \rightarrow 3Fe + 4H_2O$$

To obtain information on the degree of reduction (DOR) before exposure to FT conditions a second experiment was conducted. The calcined catalyst was reduced in the TPR instrument in a stream of pure hydrogen at 400 °C for 10 h with a ramp rate of 1 °C·min^{-1}. Subsequently, the sample was cooled to 50 °C and the gas exchanged to 5 % H_2/Ar. The hydrogen consumption was recorded upon heating to 800 °C in 10 °C·min^{-1}. Comparing the hydrogen consumption of the conventional TPR experiment and the TPR after reduction treatment yields a degree of reduction in reference to the hydrogen consumption (see Equation 5-3). In all three samples this DOR is over 99 % (see Table 5-7). Each of the supported catalysts is therefore believed to be reduced almost fully to its metallic state when exposed to H_2 pre-treatment prior to catalyst testing. The instability of the baseline in some of the measurements can be attributed to instrumental error despite a prior wait for a stable baseline.

Equation 5-3

$$Degree\ of\ Reduction = \frac{Area\ under\ the\ curves\ of\ Normal\ TPR - Area\ under\ the\ curves\ of\ pretreated\ TPR}{Area\ under\ the\ curves\ of\ Normal\ TPR} \text{ x } 100$$

Table 5-7 Summary of TPR results

Catalyst	*Area under curves of normal TPR (a.u.)*	*Area under curves of pretreated TPR (a.u.)*	*Degree of Reduction (%)*
Fe-C12A7	658.85	1.20	99.82
Fe-C12A7:e$^-$ (800 °C)	544.91	3.85	99.29
Fe-C12A7:e$^-$ (1000 °C)	435.30	1.90	99.56

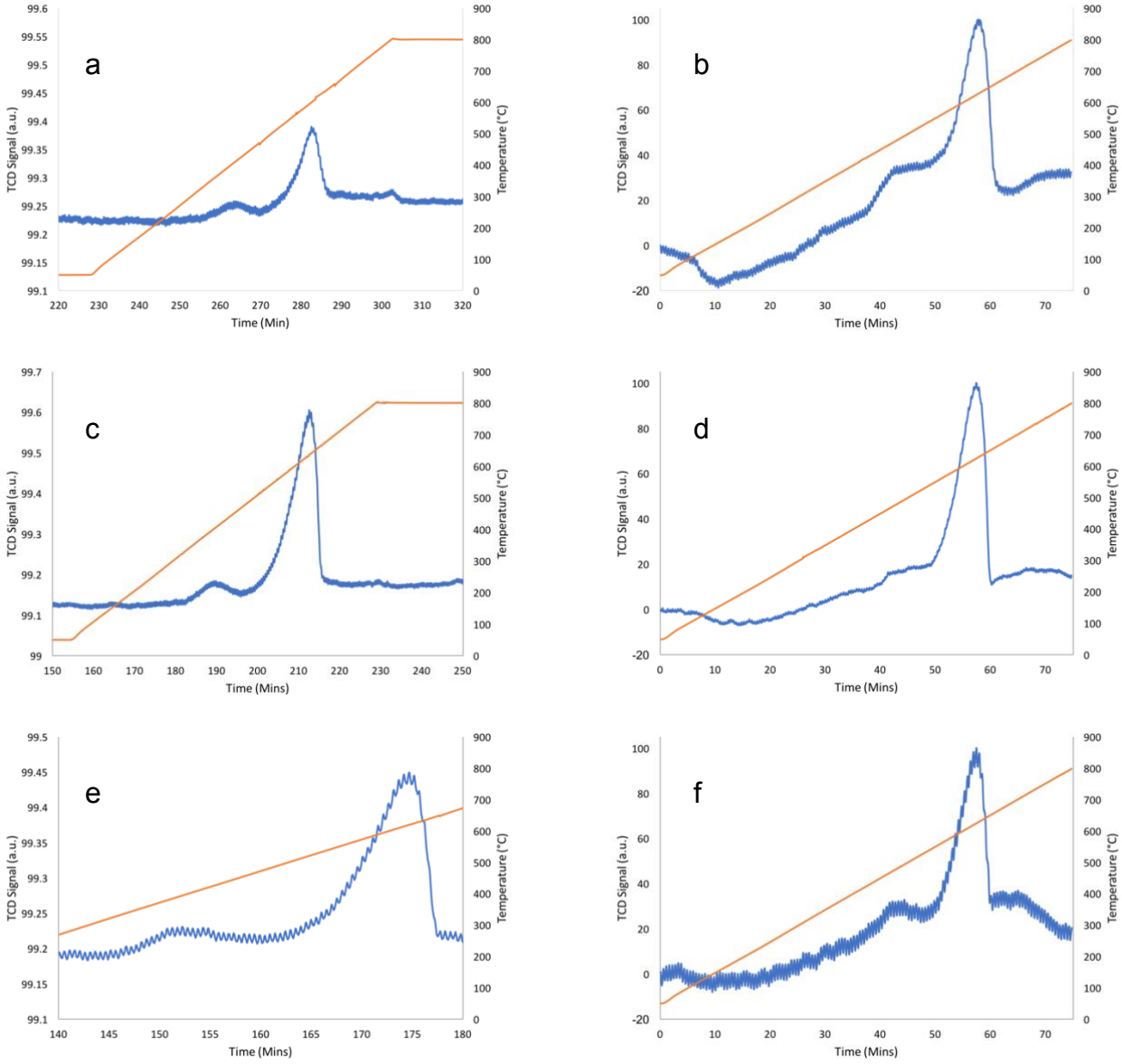

Figure 5-18 TPR profiles of (a) Fe-C12A7 post reduction pre-treatment, (b) Fe-C12A7, (c) Fe-C12A7:e^- (800 °C) post reduction pre-treatment, (d) Fe-C12A7:e^- (800 °C), (e) Fe-C12A7:e^- (1000 °C) post reduction pre-treatment and (f) Fe-C12A7:e^- (1000 °C) with the straight line graphs representing temperature and the curves representing TCD signal.

5.3 Characterization of spent catalysts

5.3.1 Powder X-ray diffraction (XRD)

As the spent precipitated Fe catalyst was diluted with Puralox (γ-alumina), its Fe-based XRD pattern can be excluded to a separate scan in which the XRD pattern of pure Puralox was subtracted (see Figure 5-19). In this scan a clear indication of the presence of metallic iron (α-Fe) was seen along with a lower

intensity indication of Hägg carbide (χ-Fe_5C_2). While these forms of iron may have been active during catalysis, there is still much speculation in the scientific community as to the which iron phases are most active and which are present during in situ testing.

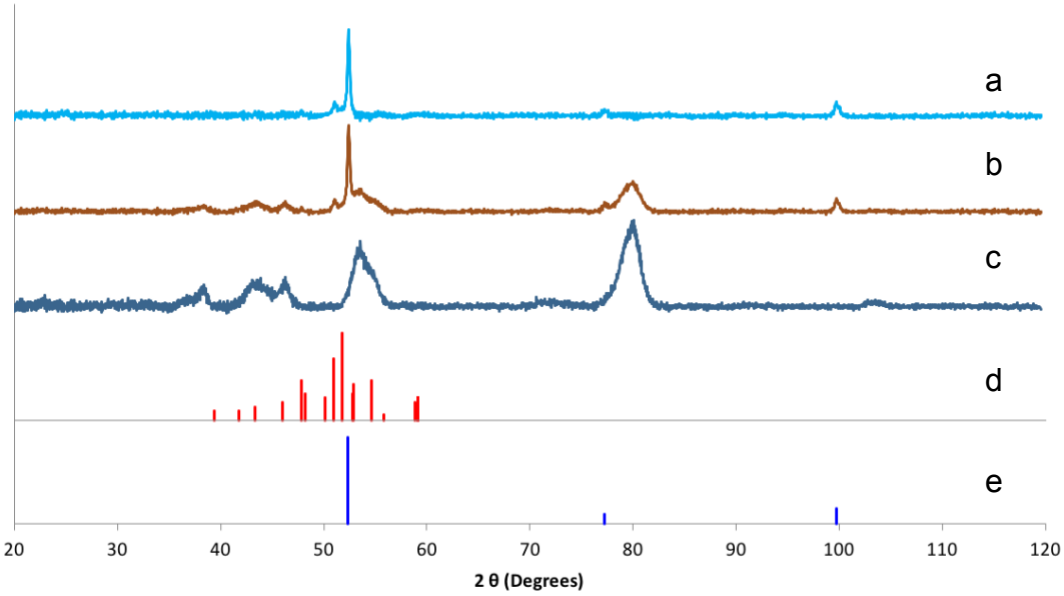

Figure 5-19 XRD pattern of (a) the spent unpromoted precipitated iron catalyst subtracting the Puralox scan, (b) the spent unpromoted precipitated iron catalyst and (c) Puralox (γ-alumina) with reference patterns for (d) Hägg carbide and (e) α-Fe.

As seen previously in the fresh supported catalysts (section 5.2.1), the C12A7 reference pattern (note that the electride is not expected to display a different pattern) was clearly identified within the XRD scans of the spent Fe loaded catalysts (see Figure 5-20). This indicates a stability of the mayenite structure as it remains present after catalysis. The CaO, $CaCO_3$ and $3CaO{\cdot}Al_2O_3$ (the latter on the 1000 °C electride only) presence was retained throughout catalysis testing for all supported catalysts. As the amount of Fe present in the sample was of low intensity, it was once again not able to be distinguished by XRD analysis. However, α-Fe and Hägg carbide is expected to be present based on the XRD analysis of the spent precipitated iron catalyst (see Figure 5-19).

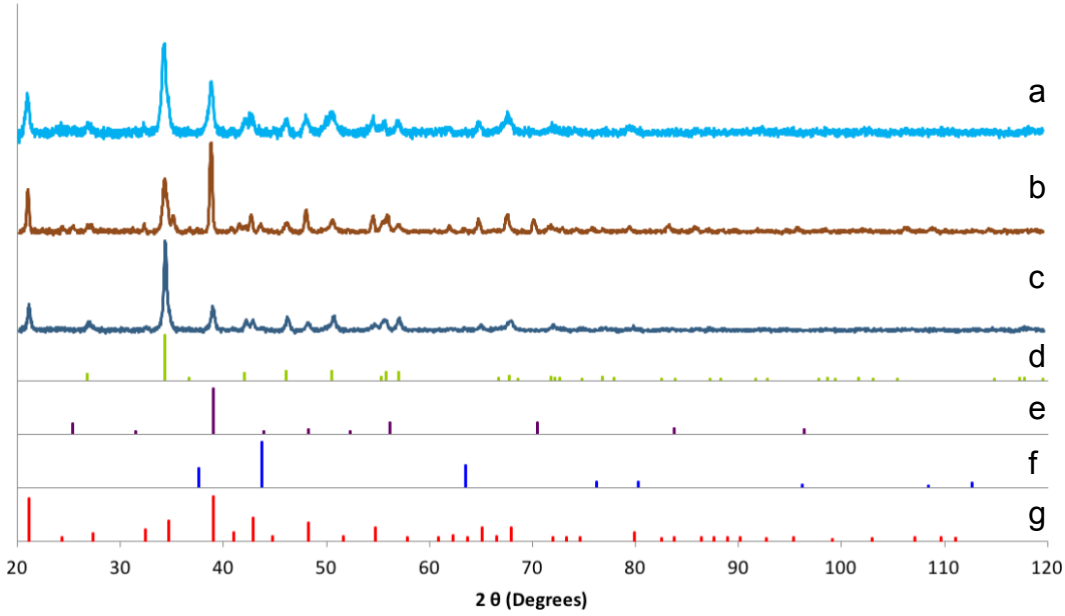

Figure 5-20 XRD pattern of the spent supported iron catalysts: (a) Fe-C12A7, (b) Fe-C12A7:e^- (1000 °C) and (c) Fe-C12A7:e^- (800 °C) with reference patterns for (d) $CaCO_3$, (e) $3CaO{\cdot}Al_2O_3$, (f) CaO and (g) C12A7.

The crystallite size of the mayenite framework, shown to increase in size upon deposition of iron particles onto the supports (section 5.2.1), was lower in size after catalyst testing (see Table 5-8). The decrease in crystallite size can possibly be hypothesized due to mechanical decomposition of the catalysts and in particular the breakdown of agglomerates to primary crystallites from attrition/crushing. The trend describing the increase in crystallite size between the catalysts based on the addition of dehydrated calcination and its subsequent temperature increase continued to hold.

Table 5-8 Crystallite size for an individual plane of each containing material within the spent supported catalysts

Sample	*Compound*	*2θ*	*Plane*	*Crystallite size (Å)*
Fe-C12A7 (Spent)	C12A7	21.080	2 1 1	316.2
	CaO	N/A (too low intensity)		
	$CaCO_3$	34.282	1 0 4	282.9
Fe-C12A7:e⁻ (1000 °C) (Spent)	C12A7	21.080	2 1 1	407.1
	CaO	43.697	2 0 0	363.6
	$CaCO_3$	56.411	1 1 6	276.2
	$3CaO{\cdot}Al_2O_3$	69.974	8 4 4	356.3
Fe-C12A7:e⁻ (800 °C) (Spent)	C12A7	21.080	2 1 1	387.6
	CaO	N/A (too low intensity)		
	$CaCO_3$	46.091	1 1 3	348.3

5.4 Catalyst Testing – LTFT

This is a comparison between the 48 h LTFT tests of each catalyst synthesised in this study: iron dispersed on the hydrothermally produced mayenite compound (Fe-C12A7); iron supported on the electrides at two evacuation temperatures: Fe-C12A7:e^- (800 °C) and Fe-C12A7:e^- (1000 °C) and the unpromoted precipitated iron bulk catalyst. CO conversions were calculated from the sum of formation rates using the GC-FID due to the very low conversions limiting the stability of the GC-TCD data. Error bars were calculated for all catalysts using the standard deviation of one time point measured in triplicate.

The CO conversion for the testing of all catalysts show low activity – below 3 % conversion throughout the runs (see Figure 5-21). Only the precipitated iron catalyst reached a very stable steady-state at around 1.5 % conversion. The mayenite and electride catalysts showed a gradual increase in conversion

throughout the runs, 2 % conversion towards the end of the testing period, and may not have achieved a steady-state at the end of 48 h.

As TPR results showed an above 99% reduction of the iron oxides, the amount of inactive iron oxide present in each catalyst can be considered negligible ruling out the possibility of a variation in the volume of active iron between catalysts prior to catalysis. Although optimal alkali promotion is suggested to increase the activity of FT catalysts (by as much as 50 %[119,194,195]), the CO conversions of the electride compounds do not show any increase compared to the mayenite supported sample.

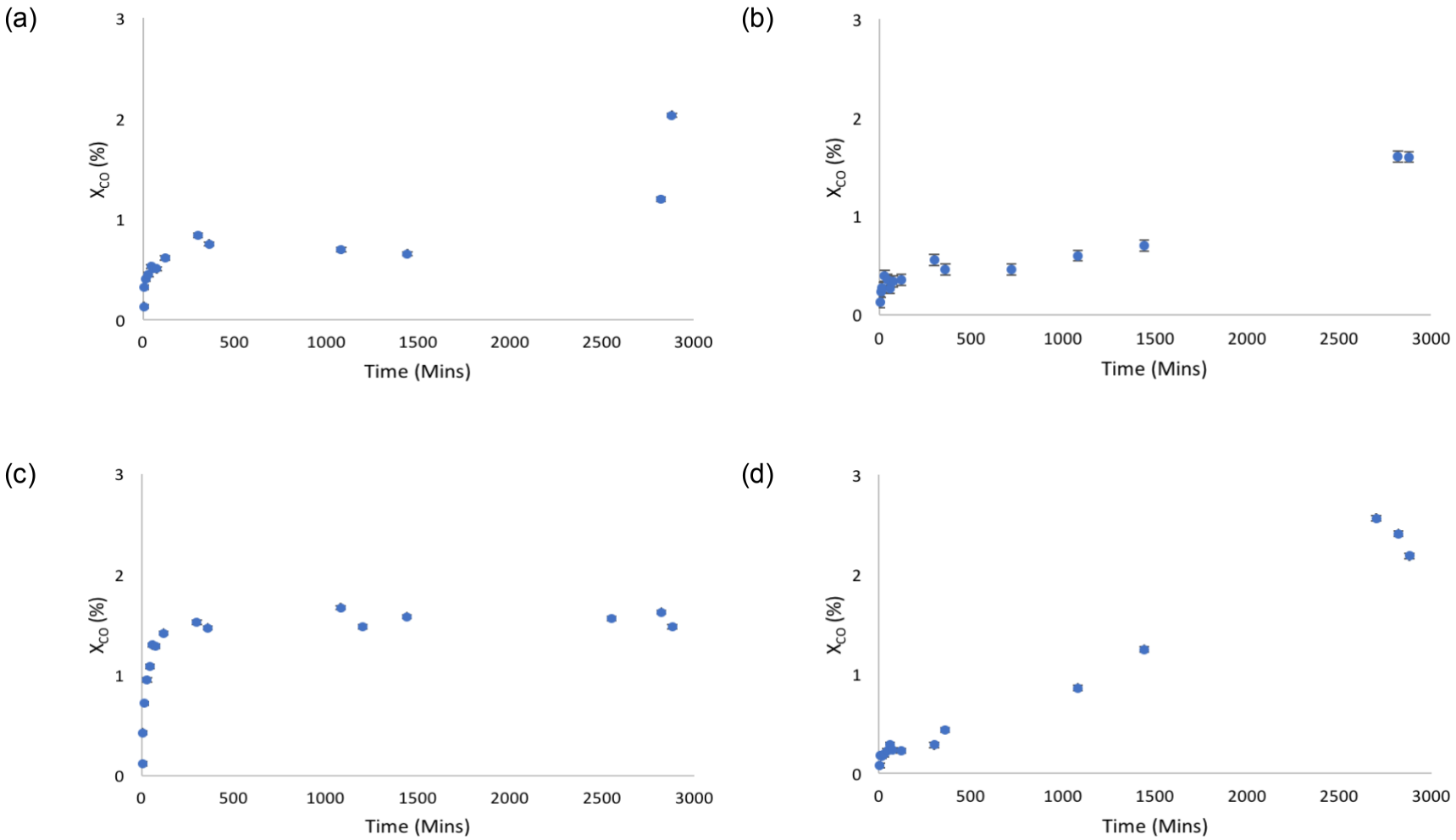

Figure 5-21 CO Conversion for (a) Fe-C12A7 (b) Fe-C12A7:e^- (800 °C) (c) Unpromoted Precipitated Fe and (d) Fe-C12A7:e^- (1000 °C)

The chain growth probability (α) for all four catalysts proved to be very similar (see Figure 5-22). This was between *ca.* 0.4 and *ca.* 0.6. The chain growth probabilities obtained for the four catalysts correlating to their obtained hydrocarbon weight fractions (methane and C5+ selectivity in Figure 5-24 and C2 – C4 selectivity in Figure 5-25) with TOS proved to be very similar to chain growth values correlated with the theoretic hydrocarbon weight fractions in Figure 2-4 (see section 2.1.4).

It can be seen for the two control catalysts, that a marginally higher but very stable steady state is reached for the chain growth probability values over time. Higher chain growth probabilities for the precipitated iron catalyst are consistent with a lower methane selectivity.

The chain growth probability (particularly in precipitated iron catalysts) has been suggested to increase with increasing alkali promotion through a maximum/optimal value by effectively increasing the C/H ratio on the catalyst's surface resulting in a reduced hydrogenation probability.[21,159] As the level of alkali promotion is zero for the precipitated iron catalyst, its coherent steady-state stability can be justified. However, the lower chain growth probability of the electride supported samples again suggests an absence of a Lewis base-like promoting functionality. The mayenite and electride supported samples are hardly distinguishable in terms of their chain growth probabilities.

As the chain growth probability is largely dependent on process conditions, the effect of identical process conditions such as temperature, residence time and initial H_2/CO ratios can be eliminated from contributing to the variation in α values for the catalysts.[196]

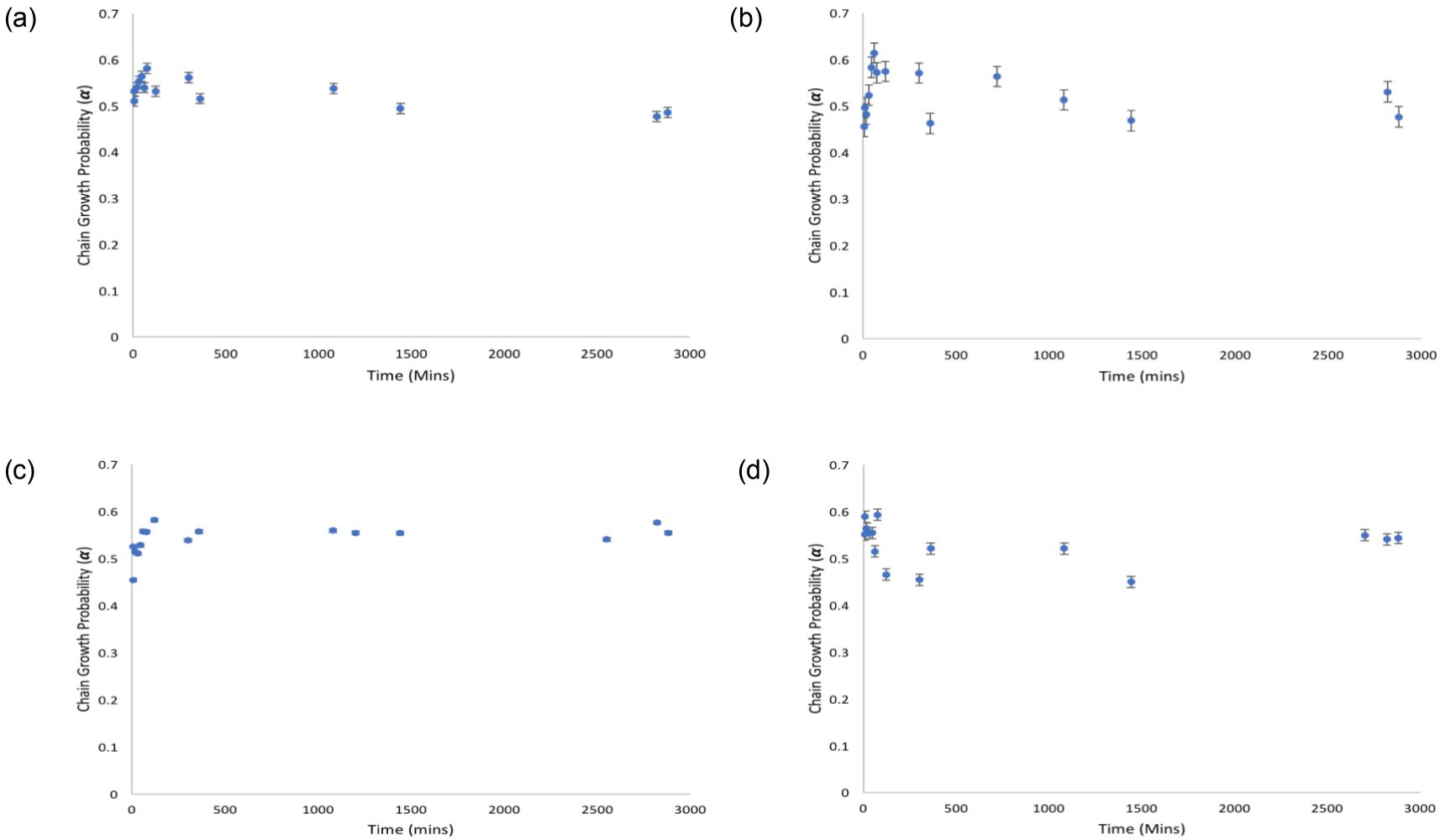

Figure 5-22 Chain Growth Probability for (a) Fe-C12A7 (b) Fe-C12A7:e^- (800 °C) (c) Unpromoted Precipitated Fe and (d) Fe-C12A7:e^- (1000 °C)

The water gas shift (WGS) selectivity, defined as the selectivity of feedstock CO to CO_2 formed via the WGS reaction (Equation 2-2, section 2.1.2), was evidently distinguishable between the catalysts studied (see Figure 5-23). For the mayenite sample the CO_2 selectivity peaks between 20 and 25 % reaching steady state (note, due to a technical error no data was recorded beyond 1100 min TOS, but comparison to the other supported catalysts suggests that WGS steady state has been achieved at this stage). For the precipitated iron catalyst, CO_2 selectivity reaches only around 5 % indicating a significantly lower WGS activity throughout the testing period compared to all supported catalysts. At steady state the Fe-C12A7:e^- catalysts reach between 15 and 17 % CO_2 selectivity.

What can be noted from these observations is that despite the activity and hydrocarbon selectivities being similar between the supported catalysts and the precipitated iron catalyst, the supported catalysts exhibit significantly higher CO_2 selectivities which is also characteristic for alkali promotion effects of iron-based FT catalysts.[119,197] However, the mayenite catalyst exhibited the highest steady state WGS indicating that the underlying cause cannot be associated to the electride but rather to characteristics already present in the mayenite sample.

Although the WGS reaction generally increases the H_2/CO ratio, in which the catalyst active sites are exposed to a higher content of hydrogenating species, a significant change in these ratios is not expected for the catalysts in this study due to the low conversions experienced.[198] While the change in syngas composition may complement the electronic effects of alkali promoted FTS in increasing the average molecular weight hydrocarbon fraction[119], it is expected to remain stable throughout TOS for these catalysts studied. As the correct mechanism of how the WGS reaction is promoted by alkali metals and in this case the electride and mayenite supports is still not well understood, the lack of a significant increase in high molecular weight hydrocarbons cannot be attributed to WGS activity differences between the studied catalysts.[119]

Although various iron phases have different levels of activity for the WGS reaction such as magnetite being much more active than iron carbides[31,199], all iron oxide is believed to be reduced during in situ testing and ideally only variation between metallic and carbidic forms of iron is expected to be present at the beginning of catalysis. Nevertheless, as synthesis proceeds, syngas may become more oxidising in nature with an increasing amount of oxide formed with TOS.[30] Again, the overall very low conversion levels make re-oxidation during FTS unrealistic.

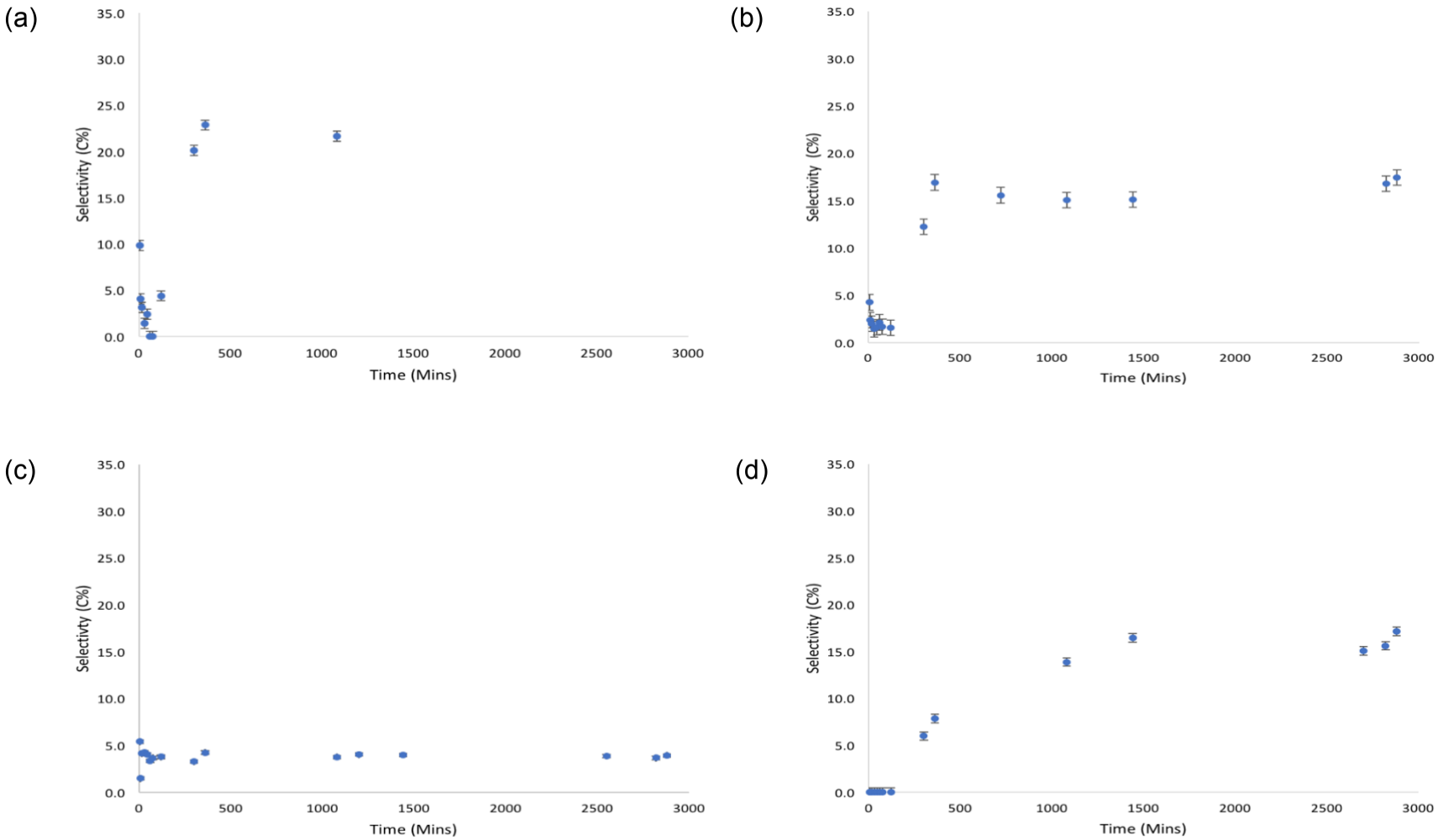

Figure 5-23 CO_2 Selectivity from hydrocarbons for (a) Fe-C12A7 (b) Fe-C12A7:e^- (800 °C) (c) Unpromoted Precipitated Fe and (d) Fe-C12A7:e^- (1000 °C)

The methane and C5+ selectivity in the hydrocarbon fraction at steady state is similar for all four catalysts ranging between 20 to 35 % and 10 to 15 % respectively (see Figure 5-24). Although alkali promotion of iron-based catalysts is generally reported to decrease methane formation, little change is seen between the electride catalysts and the precipitated iron in terms of methane selectivity. However, a study with potassium promoted precipitated iron FT catalysts showed only a slight decrease in methane selectivity with increasing alkali content at 50 % CO conversion or higher, bearing in mind these conversions are several times larger than those obtained in the present study.[9] In the initial stages of the experiment a lower methane selectivity can be observed for the supported catalysts compared to the precipitated iron.

Much like the methane selectivity, the C5+ selectivity is within a close range of each other and little increase in longer chain hydrocarbons concentrations is observed over time. The effect of alkali promotion is reported to enhance the C5+ selectivity and can be explained in terms of the electron donation from the alkali to Fe.[119,159,200,201] The effect of the electride supports on FTS therefore cannot be proven by means of a visible decrease in methane selectivity and increase in C5+ selectivity compared to the precipitated iron catalyst.

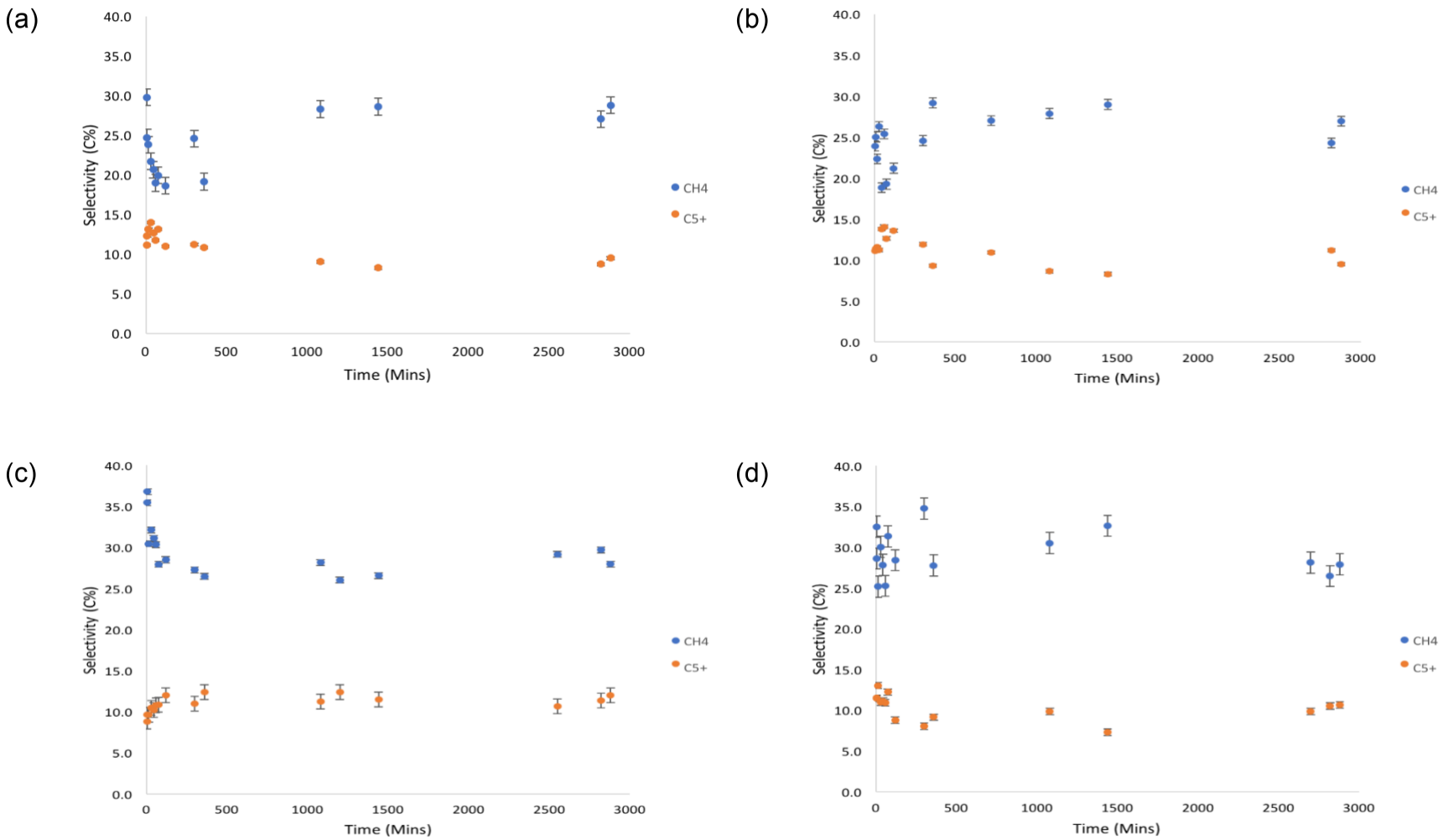

Figure 5-24 CH_4 and C5+ Selectivity from hydrocarbons for (a) Fe-C12A7 (b) Fe-C12A7:e^- (800 °C) (c) Unpromoted Precipitated Fe and (d) Fe-C12A7:e^- (1000 °C)

The selectivity of the C2, C3 and C4 fractions were of similar and consistent values for each of the four catalysts (see Figure 5-25). The selectivity towards each of the combined fractions for a carbon number decreased from C2 to C3 to C4. However, in some cases the C3 fraction outweighed the C2 fraction, this was particularly seen for the precipitated iron catalyst towards the end of the testing period. The C2 selectivity was generally between 25 and 30 % for the supported catalysts, with the average C2 selectivity being about 5 % lower for precipitated iron. In all tests, the C3 selectivity was between 20 and 25 %, while the C4 selectivity was observed to be around 10 to 20 %.

The selectivities observed for the C2 – C4 fractions were in close proximity to the theoretical fractions expected when their calculated chain growth probabilities were used in the theoretical product distribution curves – (Figure 2-4, section 2.1.4).

Whilst potassium promotion is known to decrease methane selectivity and increase C5+ selectivity in Fe-based FTS, the selectivity of the C2 – C4 fraction may be lowered. A study has shown K promotion to increase C5+ selectivity resulting in a decrease in the selectivity of the C2 – C4 fraction with Fe-Cu-K/SiO_2 catalysts.[199] Nevertheless, the total selectivity of the C2 – C4 fraction is not observed to change by a significant amount between the catalysts tested in this study.

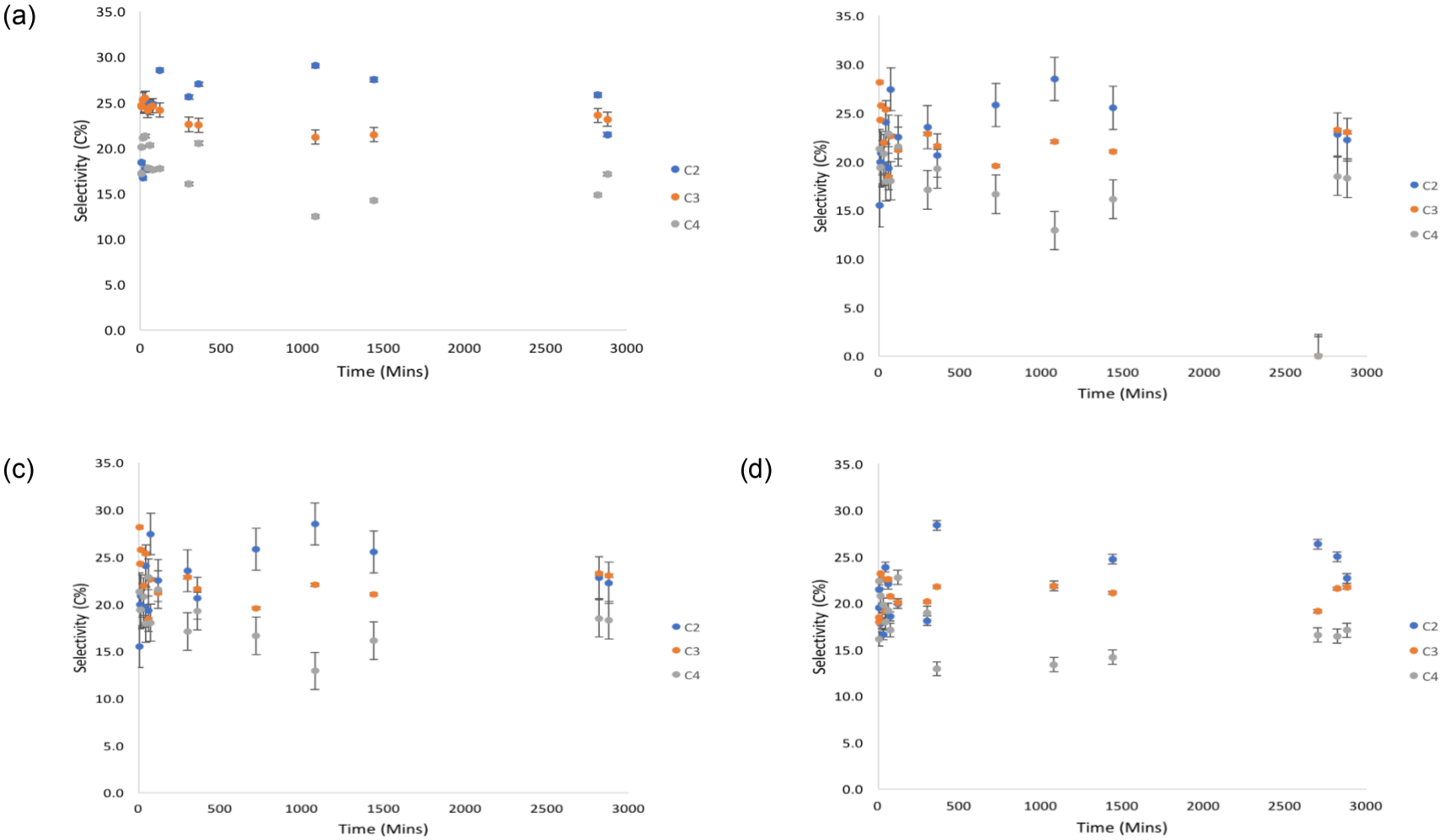

Figure 5-25 C2, C3 and C4 Selectivity for (a) Fe-C12A7 (b) Fe-C12A7:e^- (800 °C) (c) Unpromoted Precipitated Fe and (d) Fe-C12A7:e^- (1000 °C)

The olefin to paraffin (O/P) ratios for the four catalysts as a function of carbon number (Figure 5-26) and as a function of time (Figure 5-27) give a strong indication of the influence of alkali promotion. In decreasing order, the O/P ratios for all catalysts tested in this study generally follow the trend: C3 > C4 > C5 > C2. Clear evidence from both representations show that the O/P ratios are significantly lower with a general decrease over time for the precipitated iron baseline catalyst. The supported catalysts do have a similar and higher O/P ratio which further increases with TOS. Despite the mayenite catalyst not being hypothesised to exhibit promoting effects, its O/P ratios remain high along with the electrides. Once steady state is achieved, the O/P ratios remain stable for each catalyst, notwithstanding minor fluctuations. Alkali promotion has been seen to create a higher selectivity to olefins over paraffins by means of suppression of secondary reactions.[197] The higher O/P ratios for the supported catalysts could therefore suggest a promoted effect in them, despite the mayenite being a control catalyst.

Literature[30,144] has reported a significant increase in the O/P ratios for iron-based FTS, largely in the C2 fraction and less in the C3 and C5 fractions, through suppression of secondary reactions with product water. In the present study, this mechanism can be ruled out for the explanation of the observed differences due to the identical low conversion conditions. The ethylene/ethane ratio is generally a good indicator of the overall O/P ratio.[198] Ethene adsorption/desorption rates are higher than larger alkenes due to its low heat of adsorption, making it increasingly mobile to undergo secondary hydrogenation resulting in a generally lower O/P ratio of the C2 fraction than other hydrocarbons.[202] This is most notably observed with the O/P ratios of the C2 fraction in the precipitated iron catalyst. Therefore, the large increase in the O/P ratio of this fraction experienced by the supported catalysts may be due to a restriction of the adsorption/desorption probability of hydrogen analogous to that of alkali promoter effects.[81]

While a markedly decrease in methane selectivity with an increase in C5+ selectivity is characteristic for alkali promoted catalysts in conjunction with the rise of the O/P ratio, only one of these major indicators was observed for the

supported catalysts in this study suggesting either their independence from each other or that the selectivity difference is not originated by promotion-like mechanisms.

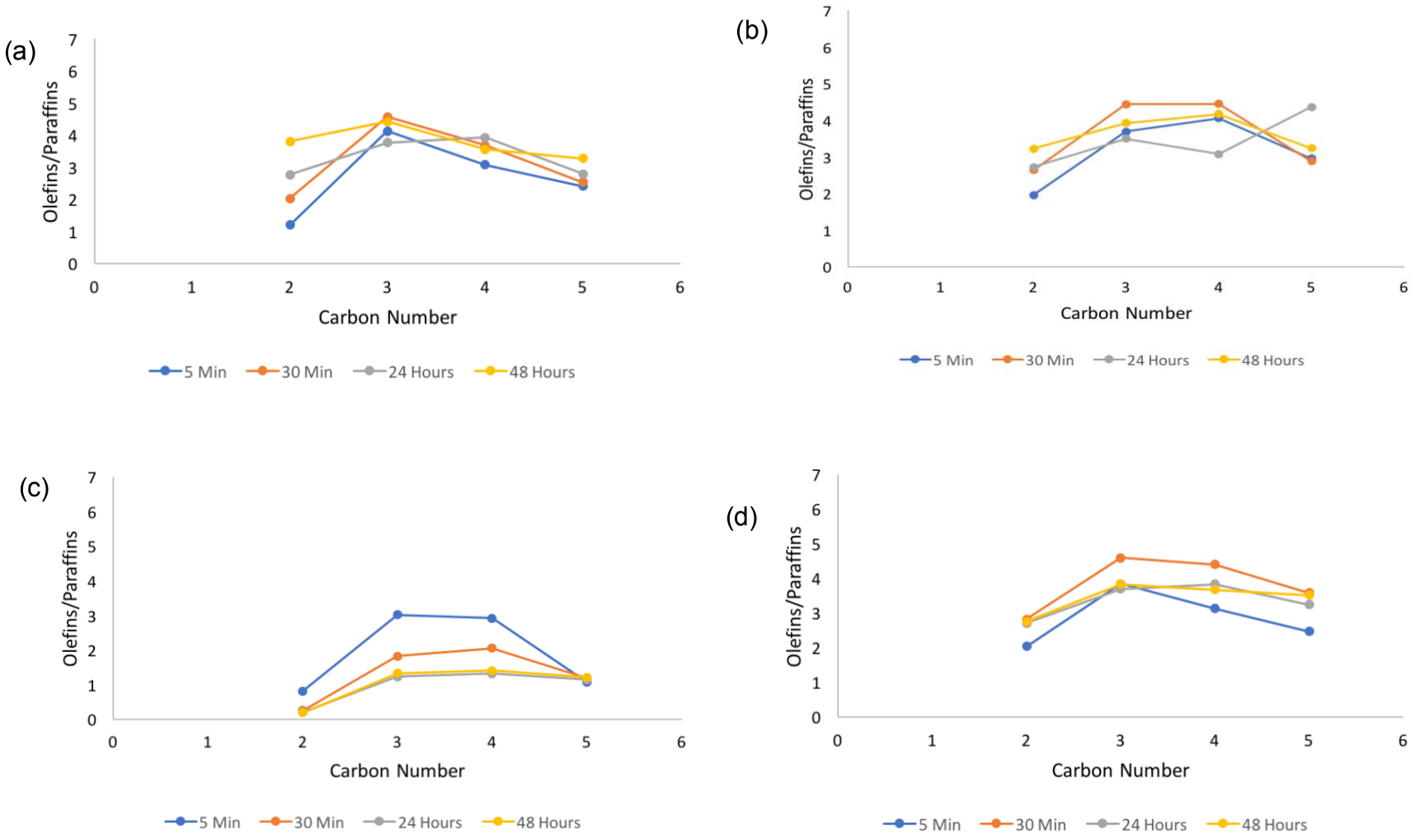

Figure 5-26 O/P ratios as function of carbon number for (a) Fe-C12A7 (b) Fe-C12A7:e^- (800 °C) (c) Unpromoted Precipitated Fe and (d) Fe-C12A7:e^- (1000 °C)

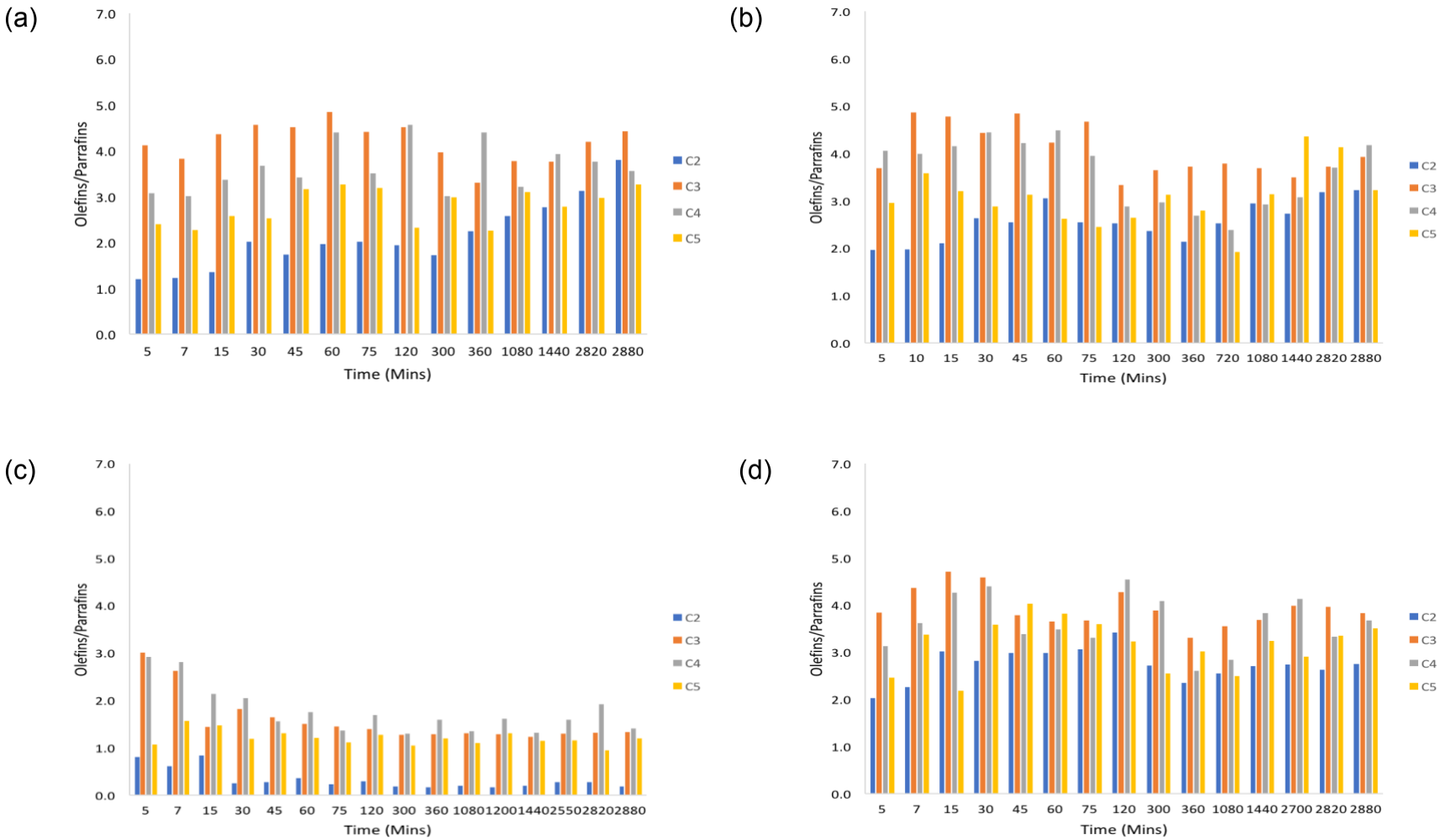

Figure 5-27 O/P ratios as a function of time for (a) Fe-C12A7 (b) Fe-C12A7:e^- (800 °C) (c) Unpromoted Precipitated Fe and (d) Fe-C12A7:e^- (1000 °C)

6 CONCLUSIONS

6.1 Synthesis and Characterisation

Mayenite was successfully synthesised via a hydrothermal process starting from aluminium and calcium hydroxide.[2] The reduction with calcium hydride was conducted after either of two vacuum calcination procedures, at 800 and 1000 °C. The success of the reduction to the electride structure could only be 'confirmed' by an observed shift in colour of the materials from white to grey. The process may not have been run to completion and thus incurring a potential loss of "promoter" effect.

The milling of the starting materials is believed to have a minimal effect on reducing the size of its particles and created a multimodal size range. Despite this, the calcination to the mayenite and final electride compounds is likely to have little difference on its integrity and yield compared to if the micronizing was not performed.

The iron precursor, $Fe(acac)_3$ showed three (in air) and two (in Ar) major exothermic decomposition temperature ranges in thermal gravimetric analysis believed to dispel most of the organics present with complete decomposition around 400 °C. AAS and ICP-OES indicated that the achieved loading was close to the targeted 10 wt % Fe.

The iron oxide present on the support compounds likely comprises of hematite and trace amounts of multiple phases, particularly FeO(OH), magnetite and maghemite. It was difficult to see the iron oxide peaks on the supported compounds via XRD analysis due to the low loading resulting in low intensity peaks. The presence of iron(III) oxide and to some extent iron(II) oxide was indicated by XPS analysis. Most iron is believed to be hematite or α-Fe_2O_3 analogous to the calcined precipitated iron catalyst as the identical conditions of decomposition of the iron precursor onto silica spheres in flowing air strongly suggested this. The iron particles present could possibly consist of a magnetite shell around a hematite core.

The crystallite sizing of the mayenite compound in each of the supported catalysts increased with dehydrated evacuation and the subsequent temperature increase in this. This suggests a higher aggregation of the mayenite compound with heating and evacuated calcination. The 1000 °C electride is also expected to possess tricalcium aluminate from the collapse of some of the mayenite structure due to its high temperature synthesis step.

TPR evidence noticeably showed proof of almost complete reduction of the supported catalysts. The iron oxide phases were largely reduced to metallic **α**-iron and iron carbides. A degree of reduction suggesting over 99% of the iron present in the catalyst was reduced indicates almost all iron present was in the active phase for catalysis.

BET physisorption indicated surface area of the catalysts to decrease with increasing evacuation temperatures during synthesis as seen in literature[2]. The electrides produced in this study did not have a surface area high enough to significantly increase the surface area of the catalyst to many inert support compounds.

6.2 Catalyst Testing

As all CO conversions were very low, the activity of all catalysts including the electrides may indicate little to no promoter activity. This is justified by the lack of a significant change to the methane and C5+ selectivity between test and control catalysts – a decrease and increase respectively that is observed with alkali promotion was not seen. However, significant increase in the O/P ratios and WGS selectivity of the mayenite and electride catalysts over the precipitated iron is analogous to that of alkali promotion. Nevertheless, the significant increase in WGS activity is highest in the mayenite sample and therefore the increase in WGS activity cannot be due to the effect of the electride.

Once again, there was no significant difference between the O/P ratios of mayenite and electride catalysts. The performance differences in this regard can be related to the process of supporting, the synthesis of the iron phase, the physiochemical properties of the support being equal in both mayenite and electride samples and/or as a result of Ca 'impurities' governing the selectivity.

The O/P ratios of the mayenite and electride samples were much higher than the precipitated iron and can be rationalised as a result of a bulk versus a supported effect. Support effects may cause inhomogeneity within a catalyst similar to that observed with manganese oxide on silica/alumina supports via Raman analysis in literature.[203] Other literature studies involving the redox properties of MnO_x catalysts showed higher dispersion and improved reducibility of bulk versus supported catalysts with an increase in average oxidation number improving these qualities in supported catalysts.[204] The O/P ratios of the supported compounds may be higher to the precipitated iron due to higher dispersion and surface area than that of the bulk catalyst.

Should the synthesis of the iron phase from its precursor not be predominantly hematite as expected, it's dispersion and reducibility may not have been as good as it could have been.

The "promotion" effects experienced by the supported compounds, particularly the mayenite catalyst which is said to be "dead" due to oxide ions present instead of anionic electrons in the crystallographic cages, may be due to CaO present acting as a potential electronic promoter. The CaO contains Ca which is an alkaline earth metal and may have electronic properties like alkali metals that promote the mayenite catalyst resulting in a similar increase of its O/P ratios to the electride catalysts. This is just one example describing equal physiochemical properties present in the supported catalysts.

Due to the low activities experienced by the supported catalysts in this study, a change in the syngas composition, normally expected due to the WGS activity increase as well as the effect of re-oxidation of the electride to mayenite compound, can be regarded as negligible. Without the use of UPS technology,

it is difficult to determine if the latter occurs, particularly as the colour change between the mayenite and electride compounds cannot be used to distinguish the supports once loaded with iron.

At this stage, concluding from this research on the C12A7:e^- compound for use in FTS, the electride is not immediately a suitable candidate as a support for alkali promotion replacement. This is based on its low activities and yields having little comparison to control catalysts.

7 OUTLOOK AND RECOMMENDATIONS

Despite the successful synthesis of the C12A7:e^- compounds via the newly established hydrothermal preparation, a more quantitative method to determine the variation between the mayenite and electride material can be explored. Ultraviolet photoelectron spectroscopy (UPS) may be utilised to determine the intrinsic work function of these materials. Several variables in synthesis that could significantly affect the activity of the final catalysts may be studied. This could include changes to the duration and temperature of the autoclave and calcination steps as well as well as crystallite and particle size considerations.

An investigation into improving the method of deposition of the Fe precursor onto the electride/mayenite supports can be identified as a key focus area. This can be to ensure iron deposition does not interfere, change or disrupt the mayenite framework or electride properties. As an alternative to $Fe(acac)_3$ precursor used in this research, a host of other organometallic precursors may be identified and considered for the system prompting potential comparative studies.

Testing of the model system can be optimised for FTS and other possible catalytic reactions. This may include testing under HTFT conditions and comparing its O/P ratios and WGS selectivities to that of this study. The effect of temperature on the WGS activity may enhance or decrease the O/P ratios which could indicate an optimisation of the promotion effects of the supports.

Using the C12A7:e^- system as a fundamental concept, the identification of additional materials that qualify as a support system facilitating increased catalytic efficiency can be explored. If an effective method to remove excess water produced in situ can be established, its combination with C12A7:e^- and the water sensitive 2D electride classes such as dicalcium nitride can be investigated for higher activity in FTS.

REFERENCES

1 M. Kitano, Y. Inoue, Y. Yamazaki, F. Hayashi, S. Kanbara, S. Matsuishi, T. Yokoyama, S.-W. Kim, M. Hara and H. Hosono, *Nat. Chem.*, 2012, **4**, 934–940.

2 Y. Inoue, M. Kitano, S. Kim, T. Yokoyama, M. Hara and H. Hosono, *ACS Catal.*, 2014, **4**, 674–680.

3 A. P. Steynberg, in *Fischer-Tropsch Technology (Studies in Surface Science and Catalysis)*, eds. A. P. Steynberg and M. E. Dry, Elsevier B.V., Amsterdam, 1st edn., 2004, vol. 152, ch. 1, p. 1.

4 B. H. Davis, *Ind. Eng. Chem. Res.*, 2007, **46**, 8938–8945.

5 M. E. Dry, *Catal. Today*, 2002, **71**, 227–241.

6 M. E. Dry, *Appl. Catal. A Gen.*, 1996, **138**, 319–344.

7 M. E. Dry, *Catal. Today*, 1990, **6**, 183–206.

8 A. P. Raje and B. H. Davis, *Catal. Today*, 1997, **36**, 335–345.

9 A. P. Raje, R. J. O'Brien and B. H. Davis, *J. Catal.*, 1998, **180**, 36–43.

10 Q. Zhang, X. Li and K. Fujimoto, *Appl. Catal. A Gen.*, 2006, **309**, 28–32.

11 Y. Cai, Y. Niu and Z. Chen, *Fuel Process. Technol.*, 1997, **50**, 163–170.

12 P. J. Goddard, J. West and R. M. Lambert, *Surf. Sci.*, 1978, **71**, 447–461.

13 F. Zasada, P. Stelmachowski, G. Maniak, J.-F. Paul, A. Kotarba and Z. Sojka, *Catal. Letters*, 2009, **127**, 126–131.

14 A. Faur Ghenciu, *Curr. Opin. Solid State Mater. Sci.*, 2002, **6**, 389–399.

15 I. H. Son, M. Shamsuzzoha and A. M. Lane, *J. Catal.*, 2002, **210**, 460–465.

16 J. Lercher, Fischer Tropsch Synthesis, http://www.tc2.ch.tum.de/fileadmin/tuchtc2/www/ICP1/ICP1_1314/9-FT_synthesis-2013_PW.pdf, (accessed 30 April 2015).

17 K.-W. Jun, H.-S. Roh, K.-S. Kim, J.-S. Ryu and K.-W. Lee, *Appl. Catal.*

A Gen., 2004, **259**, 221–226.

18 R. Mortimer, *Sasol Natural Gas Project Mozambique to South Africa: Specialist Study – Environmental Design Review*, Johannesburg, 2001.

19 D. Sparks, A. Madhlopa, S. Keen, M. Moorlach, A. Dane, P. Krog and T. Dlamini, *J. Energy South. Africa*, 2014, **25**, 80–92.

20 M. E. Dry, *Appl. Catal. A Gen.*, 1999, **189**, 185–190.

21 A. de Klerk, Fischer-Tropsch Process, http://onlinelibrary.wiley.com/, (accessed 30 April 2015).

22 M. Luo and B. H. Davis, *ACS Div. Fuel Chem. Prepr.*, 2002, **47**, 160–163.

23 M. Luo, H. Hamdeh and B. H. Davis, *Catal. Today*, 2009, **140**, 127–134.

24 M. D. Shroff, D. S. Kalakkad, K. E. Coulter, S. D. Kohler, M. S. Harrington, N. B. Jackson, A. G. Sault and A. K. Datye, *J. Catal.*, 1995, **156**, 185–207.

25 J. Xie, H. M. Torres Galvis, A. C. J. Koeken, A. Kirilin, A. I. Dugulan, M. Ruitenbeek and K. P. De Jong, *ACS Catal.*, 2016, **6**, 4017–4024.

26 G. P. Van Der Laan and A. A. C. M. Beenackers, *Catal. Rev.*, 1999, **41**, 255–318.

27 M. Claeys and E. van Steen, in *Fischer-Tropsch Technology (Studies in Surface Science and Catalysis)*, eds. A. P. Steynberg and M. E. Dry, Elsevier B.V., Amsterdam, 1st edn., 2004, vol. 152, ch. 8, pp. 609–692.

28 E. I. Mabaso, PhD thesis, University of Cape Town, 2005.

29 R. L. Espinoza, A. P. Steynberg, B. Jager and A. C. Vosloo, *Appl. Catal. A Gen.*, 1999, **186**, 13–26.

30 C. N. Satterfield, R. T. Hanlon, S. E. Tung, Z. M. Zou and G. C. Papaefthymiou, *Ind. Eng. Chem. Prod. Res. Dev.*, 1986, **25**, 407–414.

31 E. S. Lox and G. F. Froment, *Ind. Eng. Chem. Res.*, 1993, **32**, 61–70.

32 F. Fischer and H. Tropsch, *Brennstoff-Chemie*, 1926, **7**, 97–104.

33 S. R. Craxford and E. Rideal, *Brennstoff-Chemie*, 1939, **20**, 263.

34 M. P. Kaminsky, N. Winograd, G. L. Geoffroy and M. A. Vannice, *J. Am. Chem. Soc.*, 1986, **108**, 1315–1316.

35 R. Ugo, *Catal. Rev. Sci. Eng.*, 1975, **11**, 225–297.

36 W. Erley, P. H. McBreen and H. Ibach, *J. Catal.*, 1983, **84**, 229–234.

37 J. T. Kummer, T. W. DeWitt and P. H. Emmett, *J. Am. Chem. Soc.*, 1948, **70**, 3632–3643.

38 P. M. Maitlis, R. Quyoum, H. C. Long and M. L. Turner, *Appl. Catal. A Gen.*, 1999, **186**, 363–374.

39 H. H. Storch, N. Golumbic and R. B. Anderson, *The Fischer-Tropsch and Related Synthesis*, John Wiley & Sons, Inc., New York, 1951.

40 K. Yoshizawa, S. Toyota and F. Toda, *Tetrahedron Lett.*, 2001, **42**, 7983–7985.

41 C. K. Rofer-DePoorter, *Chem. Rev.*, 1981, **81**, 447–474.

42 H. Pichler and H. Schulz, *Chemie Ing. Tech.*, 1970, **42**, 1162–1174.

43 H. Schulz, *Appl. Catal. A Gen.*, 1999, **186**, 3–12.

44 H. Schulz and H. Gökcebay, in *British Polymer Journal*, eds. G. Ertl, H. Knözinger, F. Schüth and J. Weitkamp, Dekker, New York, 1984, vol. 16, p. 153.

45 E. W. Kuipers, C. Scheper, J. H. Wilson, I. H. Vinkenburg and H. Oosterbeek, *J. Catal.*, 1996, **158**, 288–300.

46 J. Cheng, P. Hu, P. Ellis, S. French, G. Kelly and C. M. Lok, *J. Catal.*, 2008, **257**, 221–228.

47 V. Cheang, PhD thesis, University of Cape Town, 2009.

48 K. D. Kruit, D. Vervloet, F. Kapteijn and J. R. van Ommen, *Catal. Sci. Technol.*, 2013, **3**, 2210–2213.

49 E. de Smit and B. M. Weckhuysen, *Chem. Soc. Rev.*, 2008, **37**, 2758–2781.

50 M. E. Dry and G. J. Oosthuizen, *J. Catal.*, 1968, **11**, 18–24.

51 H. Schulz and M. Claeys, *Appl. Catal. A Gen.*, 1999, **186**, 91–107.

52 L. C. Almeida, O. González, O. Sanz, A. Paul, M. A. Centeno, J. A. Odriozola and M. Montes, in *Studies in Surface Science and Catalysis*, eds. F. B. Noronha, M. Schmal and E. F. Sousa-Aguiar, Elsevier B.V., Amsterdam, 2007, vol. 167, pp. 79–84.

53 X. Li, J. He, M. Meng, Y. Yoneyama and N. Tsubaki, *J. Catal.*, 2009, **265**, 26–34.

54 E. F. Gallei, M. Hesse and E. Schwab, in *Handbook of Heterogeneous Catalysis*, eds. G. Ertl, H. Knözinger, F. Schüth and J. Weitkamp, WILEY-VCH Verlag GmbH and Co., Weinheim, Germany, 2nd edn., 2008, ch. 2, p. 57.

55 K. Sudsakorn, PhD thesis, University of Pittsburgh, 2002.

56 A. Y. Khodakov, W. Chu and P. Fongarland, *Chem. Rev.*, 2007, **107**, 1692–1744.

57 L. Bruce and J. F. Mathews, *Appl. Catal.*, 1982, **4**, 353–369.

58 E. Iglesia, S. L. Soled and R. A. Fiato, *J. Catal.*, 1992, **137**, 212–224.

59 M. L. Turner, H. C. Long, A. Shenton, P. K. Byers and P. M. Maitlis, *Chem. - A Eur. J.*, 1995, **1**, 549–556.

60 J. W. Dun, E. Gulari and K. Y. S. N.G, *Appl. Catal.*, 1985, **15**, 247–263.

61 P. Patterson, T. K. Das and B. H. Davis, *Appl. Catal. A Gen.*, 2003, **251**, 449–455.

62 R. Psaro, R. Ugo, G. M. Zanderighi, B. Besson, A. K. Smith and J. M. Basset, *J. Organomet. Chem.*, 1981, **213**, 215–247.

63 J. Xu, Y. Yang and Y. W. Li, *Fuel*, 2015, **152**, 122–130.

64 L. D. Mansker, Y. Jin, D. B. Bukur and A. K. Datye, *Appl. Catal. A Gen.*, 1999, **186**, 277–296.

65 S. Li, S. Krishnamoorthy, A. Li, G. D. Meitzner and E. Iglesia, *J. Catal.*, 2002, **206**, 202–217.

66 D. J. Duvenhage, R. L. Espinoza and N. J. Coville, in *Studies in Surface Science and Catalysis*, eds. B. Delmon and G. F. Froment, Elsevier B.V., Ostend, Belgium, 1994, vol. 88, pp. 351–358.

67 T. Mccartney, L. J. E. Hofer, W. C. Peebles and B. Anderson, 1952, **766**, 730–736.

68 F. Blanchard, J. P. Reymond, B. Pommier and S. J. Teichner, *J. Mol. Catal.*, 1982, **17**, 171–181.

69 G. P. van der Laan and A. A. C. M. Beenackers, *Appl. Catal. A Gen.*, 2000, **193**, 39–53.

70 A. M. Saib, D. J. Moodley, I. M. Ciobîcă, M. M. Hauman, B. H. Sigwebela, C. J. Weststrate, J. W. Niemantsverdriet and J. van de Loosdrecht, *Catal. Today*, 2010, **154**, 271–282.

71 P. Serp, P. Kalck and R. Feurer, *Chem. Rev.*, 2002, **102**, 3085–3128.

72 M. C. Bahome, L. L. Jewell, D. Hildebrandt, D. Glasser and N. J. Coville, *Appl. Catal. A Gen.*, 2005, **287**, 60–67.

73 G. L. Bezemer, J. H. Bitter, H. P. C. E. Kuipers, H. Oosterbeek, J. E. Holewijn, X. Xu, F. Kapteijn, A. J. van Dillen and K. P. de Jong, *J. Am. Chem. Soc.*, 2006, **128**, 3956–3964.

74 G. Jacobs, T. K. Das, Y. Zhang, J. Li, G. Racoillet and B. H. Davis, *Appl. Catal. A Gen.*, 2002, **233**, 263–281.

75 J. Li, X. Cheng, C. Zhang, J. Wang, W. Dong, Y. Yang and Y. Li, *J. Chem. Technol. Biotechnol.*, 2017, **92**, 1472–1480.

76 A. Vojvodic, A. J. Medford, F. Studt, F. Abild-Pedersen, T. S. Khan, T. Bligaard and J. K. Nørskov, *Chem. Phys. Lett.*, 2014, **598**, 108–112.

77 I. Boz, D. Chadwick, I. S. Metcalfe and K. Zheng, in *New Frontiers in Catalysis (Studies in Surface Science and Catalysis)*, eds. L. Guczi, F. Solymosi and P. Tetenyi, Elsevier, Budapest, 1993, vol. 75, pp. 2785–2788.

78 A. Siahvashi and A. A. Adesina, *Catal. Today*, 2013, **214**, 30–41.

79 P. Legutko, T. Jakubek, W. Kaspera, P. Stelmachowski, Z. Sojka and A. Kotarba, *Catal. Commun.*, 2014, **43**, 34–37.

80 G. Brodén, G. Gafner and H. P. Bonzel, *Surf. Sci.*, 1979, **84**, 295–314.

81 D. O. Uner, *Ind. Eng. Chem. Res.*, 1998, **37**, 2239–2245.

82 M. E. Dry, in *Fischer-Tropsch Technology (Studies in Surface Science and Catalysis)*, eds. M. E. Dry and A. P. Steynberg, Elsevier B.V., Amsterdam, 1st edn., 2004, vol. 152, ch. 3, p. 196.

83 R. B. Anderson, in *Catalysis*, ed. P. H. Emmett, Reinhold Publishing Corporation, New York, 1956, vol. 4, pp. 257–231.

84 R. J. O'Brien, L. Xu, R. L. Spicer, S. Bao, D. R. Milburn and B. H. Davis, *Catal. Today*, 1997, **36**, 325–334.

85 L. Lietti, I. Nova, G. Ramis, L. Dall'Acqua, G. Busca, E. Giamello, P. Forzatti and F. Bregani, *J. Catal.*, 1999, **187**, 419–435.

86 M. Kurtz, H. Wilmer, T. Genger, O. Hinrichsen and M. Muhler, *Catal. Letters*, 2003, **86**, 77–80.

87 A. de Klerk, Y.-W. Li and R. Zennaro, in *Greener Fischer–Tropsch processes for fuels and feedstocks*, eds. P. M. Maitlis and A. de Klerk, Wiley-VCH Verlag GmbH & Co. KGaA, Weinheim, Germany, 1st edn., 2013, pp. 53–69.

88 E. Iglesia, *Appl. Catal. A Gen.*, 1997, **161**, 59–78.

89 A. P. Steynberg, M. E. Dry, B. H. Davis and B. B. Bremen, in *Fischer-Tropsch Technology (Studies in Surface Science and Catalysis)*, eds. A. P. Steynberg and M. E. Dry, Elsevier B.V., Amsterdam, 1st edn., 2004, vol.152, ch. 2, p. 64.

90 M. J. Baird, R. R. Schehl and W. P. Haynes, *Ind. Eng. Chem. Process Des. Dev.*, 1980, **19**, 175–191.

91 M. Janse van Vuuren, J. Huyser, T. Grobler and G. Kupi, *Advances in Fischer-Tropsch Synthesis, Catalysts, and Catalysis*, CRC Press Taylor & Francis Group, Boca Raton, 2010.

92 R. Guettel, U. Kunz and T. Turek, *Chem. Eng. Technol.*, 2008, **31**, 746–754.

93 J. Eilers, S. A. Posthuma and S. T. Sie, *Catal. Letters*, 1991, **7**, 253–269.

94 S. T. Sie, in *Reviews in Chemical Engineering*, eds. D. Luss and B. Neima, Walter de Gruyter GmbH & Co., Berlin, 1998, vol. 14, pp. 109–

157.

95 B. Jager, R. C. Kelfkens and A. P. Steynberg, in *Natural Gas Conversion II (Studies in Surface Science and Catalysis)*, eds. H. E. Curry-Hyde and R. F. Howe, Elsevier B.V., Amsterdam, 1994, vol. 81, pp. 419–425.

96 R. Guettel and T. Turek, *Chem. Eng. Sci.*, 2009, **64**, 955–964.

97 R. Krishna, J. M. van Baten, M. I. Urseanu and J. Ellenberger, *Chem. Eng. Sci.*, 2001, **56**, 537–545.

98 L. Caldwell and D. S. Van Vuuren, *Chem. Eng. Sci.*, 1986, **41**, 89–96.

99 S. L. Suib, in *Selectivity in Catalysis*, eds. M. E. Davis and S. L. Suib, American Chemical Society, Washington, D.C., 1993, vol. 517, pp. 1–19.

100 A. P. Steynberg, R. L. Espinoza, B. Jager and A. C. Vosloo, *Appl. Catal. A Gen.*, 1999, **186**, 41–54.

101 P. V Sushko, A. L. Shluger, K. Hayashi, M. Hirano and H. Hosono, *Phys. Rev. Lett.*, 2003, **91**, 126401.

102 S. Matsuishi, Y. Toda, M. Miyakawa, K. Hayashi, T. Kamiya, M. Hirano, I. Tanaka and H. Hosono, *Science*, 2003, **301**, 626–629.

103 A. S. Ichimura, J. L. Dye, M. A. Camblor and L. A. Villaescusa, *J. Am. Chem. Soc.*, 2002, **124**, 1170–1171.

104 J. L. Dye, *Science*, 1990, **247**, 663–668.

105 M. Miyakawa, S. W. Kim, M. Hirano, Y. Kohama, H. Kawaji, T. Atake, H. Ikegami, K. Kono and H. Hosono, *J. Am. Chem. Soc.*, 2007, **129**, 7270–7271.

106 B. Matović, M. Prekajski, J. Pantić, T. Bräuniger, M. Rosić, D. Zagorac and D. Milivojević, *J. Eur. Ceram. Soc.*, 2016, **36**, 4237–4241.

107 M. Hiraishi, K. M. Kojima, M. Miyazaki, I. Yamauchi, H. Okabe, A. Koda, R. Kadono, S. Matsuishi and H. Hosono, *Phys. Rev. B*, 2016, **93**, 121201.

108 Y. Toda, H. Yanagi, E. Ikenaga, J. J. Kim, M. Kobata, S. Ueda, T.

Kamiya, M. Hirano, K. Kobayashi and H. Hosono, *Adv. Mater.*, 2007, **19**, 3564–3569.

109 S. Matsuishi, T. Nomura, M. Hirano, K. Kodama, S. Shamoto and H. Hosono, *Chem. Mater.*, 2009, **21**, 2589–2591.

110 S. Yang, J. N. Kondo, K. Hayashi, M. Hirano, K. Domen and H. Hosono, *Appl. Catal. A Gen.*, 2004, **277**, 239–246.

111 P. V Sushko, A. L. Shluger, M. Hirano and H. Hosono, *J. Am. Chem. Soc.*, 2007, **129**, 942–951.

112 Z. Li, J. Yang, J. G. Hou and Q. Zhu, *Angew. Chemie - Int. Ed.*, 2004, **43**, 6479–6482.

113 N. Kuganathan, H. Hosono, A. L. Shluger and P. V. Sushko, *J. Am. Chem. Soc.*, 2014, **136**, 2216–2219.

114 P. Kubelka and F. Munk, *Zeitschrift für Tech. Phys.*, 1931, **12**, 593–601.

115 M. Kitano, S. Kanbara, Y. Inoue, N. Kuganathan, P. V. Sushko, T. Yokoyama, M. Hara and H. Hosono, *Nat. Commun.*, 2015, **6**, 6731.

116 Z. Liu, S. Shi and Y. Li, *Chem. Eng. Sci.*, 2010, **65**, 12–17.

117 F. Hayashi, Y. Toda, Y. Kanie, M. Kitano, Y. Inoue, T. Yokoyama, M. Hara and H. Hosono, *Chem. Sci.*, 2013, **4**, 3124–3130.

118 W. Ngantsoue-Hoc, Y. Zhang, R. J. O'Brien, M. Luo and B. H. Davis, *Appl. Catal. A Gen.*, 2002, **236**, 77–89.

119 D. B. Bukur, D. Mukesh and S. A. Patel, *I n d . Eng. Chem. Res*, 1990, **29**, 194–204.

120 A. Rabenau and H. Schulz, *J. Less Common Met.*, 1976, **50**, 155–159.

121 N. E. Brese and M. O'Keeffe, *J. Solid State Chem.*, 1990, **87**, 134–140.

122 U. Steinbrenner and A. Simon, *Zeitschrift für Anorg. und Allg. Chemie*, 1998, **624**, 228–232.

123 D. H. Gregory, A. Bowman, C. F. Baker and D. P. Weston, *J. Mater. Chem.*, 2000, **10**, 1635–1641.

124 Y. Laurent, J. Lang and M. T. Le Bihan, *Acta Crystallogr. Sect. B Struct. Crystallogr. Cryst. Chem.*, 1968, **24**, 494–499.

125 E. T. Keve and A. C. Skapski, *Chem. Commun.*, 1966, **22**, 829.

126 E. T. Keve and A. C. Skapski, *Inorg. Chem.*, 1968, **7**, 1757–1761.

127 T. Inoshita, S. Jeong, N. Hamada and H. Hosono, *Phys. Rev. X*, 2014, **4**, 31023.

128 K. Lee, S. W. Kim, Y. Toda, S. Matsuishi and H. Hosono, *Nature*, 2013, **494**, 336–340.

129 K. P. De Jong, in *Synthesis of Solid Catalysts*, ed. K. P. De Jong, WILEY-VCH Verlag GmbH and Co., Weinheim, Germany, First., 2009.

130 C. Perego and P. Villa, *Catal. Today*, 1997, **34**, 281–305.

131 V. Meille, *Appl. Catal. A Gen.*, 2006, **315**, 1–17.

132 J. W. Geus and A. Jos van Dillen, in *Handbook of Heterogeneous Catalysis*, eds. G. Ertl, H. Knözinger, F. Schüth and J. Weitkamp, WILEY-VCH Verlag GmbH and Co., Weinheim, Germany, 2nd edn., 2008, ch. 2, p. 428.

133 A. Lycourghiotis, in *Synthesis of Solid Catalysts*, ed. K. P. De Jong, WILEY-VCH Verlag GmbH and Co., Weinheim, Germany, First., 2009, ch. 2, pp. 13–31.

134 A. Rajaeiyan and M. M. Bagheri-Mohagheghi, *Adv. Manuf.*, 2013, **1**, 176–182.

135 E. Marceau, X. Carrier, M. Che, O. Clause and C. Marcilly, in *Handbook of Heterogeneous Catalysis*, eds. G. Ertl, H. Knözinger, F. Schüth and J. Weitkamp, WILEY-VCH Verlag GmbH and Co., Weinheim, Germany, 2nd edn., 2008, ch. 2, p. 467.

136 D. C. Bradley, *Chem. Rev.*, 1989, **89**, 1317–1322.

137 M. Argyle and C. Bartholomew, *Catalysts*, 2015, **5**, 145–269.

138 P. Forzatti, *Catal. Today*, 1999, **52**, 165–181.

139 E. B. Maxted, *Adv. Catal.*, 1951, **3**, 129–178.

140 P. Desikan and C. H. Amberg, *Can. J. Chem.*, 1964, **42**, 843–850.

141 J. Voliter and M. Hermann, *Zeitschrift Anorg. und Allg. Chemie*, 1974,

405, 315–328.

142 C. H. Bartholomew, in *Catalyst Deactivation (Studies in Surface Science and Catalysis)*, Elsevier B.V., Amsterdam, 1987, vol. 34, pp. 81–104.

143 M. E. Dry, *Catal. Letters*, 1991, **7**, 241–251.

144 M. E. Dry, in *Catalysis Science & Technology*, eds. J. R. Anderson and M. Boudart, Springer-Verlag, Berlin, 1981, vol. 1, pp. 159–255.

145 R. D. Clay and E. E. Peterson, *J. Catal.*, 1970, **16**, 32–43.

146 K. Baron, *Thin Solid Films*, 1978, **55**, 449–462.

147 C. H. Bartholomew and R. J. Farrauto, in *Fundamentals of Industrial Catalytic Processes*, John Wiley & Sons, Inc., Hoboken, NJ, USA, 2nd ed., 2010, ch. 6, pp. 339–486.

148 C. H. Bartholomew, *Appl. Catal. A Gen.*, 2001, **212**, 17–60.

149 C. H. Bartholomew, *Catal. Rev.*, 1982, **24**, 67–112.

150 B. C. Gates, J. R. Katzer and G. C. A. Schuit, *Chemistry of Catalytic Processes*, McGraw-Hill, New York, 1979.

151 C. Naccache, in *Deactivation and Poisoning of Catalysts*, eds. J. Oudar and H. Wise, Marcel Dekker, New York, 1985, pp. 185–203.

152 P. G. Menon, *J. Mol. Catal.*, 1990, **59**, 207–220.

153 S. E. Wanke and P. C. Flynn, *Catal. Rev.*, 1975, **12**, 93–135.

154 J. A. Moulijn, A. E. Van Diepen and F. Kapteijn, *Appl. Catal. A Gen.*, 2001, **212**, 3–16.

155 C. H. Bartholomew, in *Catalyst Deactivation (Studies in Surface Science and Catalysis)*, eds. B. Delmon and G. F. Froment, Elsevier B.V., Amsterdam, 1994, vol. 88, pp. 1–18.

156 A. G. Shastri, A. K. Datye and J. Schwank, *Appl. Catal.*, 1985, **14**, 119–131.

157 G. Busca, *Appl. Catal. B Environ.*, 1998, **18**, 1–36.

158 M. E. Dry, in *Catalysis Science & Technology*, eds. J. Anderson and M.

Boudart, Springer-Verlag, New York, 1984, pp. 159–218.

159 W. Ning, N. Koizumi, H. Chang, T. Mochizuki, T. Itoh and M. Yamada, *Appl. Catal. A Gen.*, 2006, **312**, 35–44.

160 H. N. Pham, J. Reardon and A. K. Datye, *Powder Technol.*, 1999, **103**, 95–102.

161 J. G. Chen, *Chem. Rev.*, 1996, **96**, 1477–1498.

162 D. B. Bukur, Report on *Development of Improved Fischer-Tropsch Catalysts*, Texas A&M University, College Station, 1994.

163 D. S. Kalakkad, M. D. Shroff, S. Köhler, N. Jackson and A. K. Datye, *Appl. Catal. A Gen.*, 1995, **133**, 335–350.

164 X.-D. Wang, Z.-X. Shen, T. Sang, X.-B. Cheng, M.-F. Li, L.-Y. Chen and Z.-S. Wang, *J. Colloid Interface Sci.*, 2010, **341**, 23–29.

165 M. Iglesias G., C. de Vries, M. Claeys and G. Schaub, *Catal. Today*, 2015, **242**, 184–192.

166 N. Fischer, R. Henkel, B. Hettel, M. Iglesias, G. Schaub and M. Claeys, *Catal. Letters*, 2016, **146**, 509–517.

167 Q. Fu and W. Sun, *Appl. Opt.*, 2001, **40**, 1354.

168 A. L. Patterson, *Phys. Rev.*, 1939, **56**, 978–982.

169 U. Holzwarth and N. Gibson, *Nat. Nanotechnol.*, 2011, **6**, 534.

170 S. Brunauer, P. H. Emmett and E. Teller, *J. Am. Chem. Soc.*, 1938, **60**, 309–319.

171 S. Brunauer, L. S. Deming, W. E. Deming and E. Teller, *J. Am. Chem. Soc.*, 1940, **62**, 1723–1732.

172 P. Cairns, PhD thesis, University of Cape Town, 2008.

173 N. Fischer, PhD thesis, University of Cape Town, 2011.

174 H. Schulz, W. Bohringer, C. Kohl, N. Rahman and A. Will, *DGMK Forschungsbericht*, 1984, **3**, 320.

175 R. Kaiser, *Methoden der Phys. Anal.*, 1969, **5**, 357.

176 E. S. Kováts, *Fresenius' Zeitschrift für Anal. Chemie*, 1961, **181**, 351–

364.

177 A. Tavakoli, M. Sohrabi and A. Kargari, *Chem. Eng. J.*, 2008, **136**, 358–363.

178 N. K. Sahu, A. Prakash and D. Bahadur, *Dalt. Trans.*, 2014, **43**, 4892–4900.

179 F. Mederos-Henry, B. P. Pichon, Y. T. Yagang, A. Delcorte, C. Bailly, I. Huynen and S. Hermans, *J. Mater. Chem. C*, 2016, **4**, 3290–3303.

180 Y. Li, M. Afzaal and P. O'Brien, *J. Mater. Chem.*, 2006, **16**, 2175.

181 C. Ianasi, O. Costisor, A.-M. Putz, R. Lazau, A. Negrea, D. Niznansky, L. Sacarescu and C. Savii, *Process. Appl. Ceram.*, 2016, **10**, 265–275.

182 B. Pal and M. Sharon, *Thin Solid Films*, 2000, **379**, 83–88.

183 J. Von Hoene, R. G. Charles and W. M. Hickam, *J. Phys. Chem.*, 1958, **62**, 1098–1101.

184 N. K. Sahu, A. Prakash and D. Bahadur, *Dalt. Trans.*, 2014, **43**, 4892–4900.

185 A. Irabien, J. R. Viguri and I. Ortiz, *Ind. Eng. Chem. Res.*, 1990, **29**, 1599–1606.

186 A. Irabien, J. R. Viguri, F. Cortabitarte and I. Ortiz, *Ind. Eng. Chem. Res.*, 1990, **29**, 1606–1611.

187 M. A. Amod, MSc thesis, University of Cape Town, 2011.

188 A. Martínez, C. López, F. Márquez and I. Díaz, *J. Catal.*, 2003, **220**, 486–499.

189 M. C. Biesinger, B. P. Payne, A. P. Grosvenor, L. W. M. Lau, A. R. Gerson and R. S. C. Smart, *Appl. Surf. Sci.*, 2011, **257**, 2717–2730.

190 M. C. Biesinger, B. P. Payne, A. P. Grosvenor, L. W. M. Lau, A. R. Gerson and R. S. C. Smart, *Appl. Surf. Sci.*, 2011, **257**, 2717–2730.

191 A. P. Grosvenor, B. A. Kobe, M. C. Biesinger and N. S. McIntyre, *Surf. Interface Anal.*, 2004, **36**, 1564–1574.

192 T. Yamashita and P. Hayes, *Appl. Surf. Sci.*, 2008, **254**, 2441–2449.

193 C. R. A. Catlow, L. Ackermann, R. G. Bell, D. H. Gay, S. Holt, D. W. Lewis, M. A. Nygren, G. Sastre, D. C. Sayle and P. E. Sinclair, *J. Mol. Catal. A Chem.*, 1997, **115**, 431–448.

194 M. E. Dry, in *Fischer-Tropsch Technology (Studies in Surface Science and Catalysis)*, eds. A. Steynberg and M. E. Dry, Elsevier B.V., Amsterdam, 1st edn., 2004, vol. 152, ch. 7, p. 533.

195 M. E. Dry, *Catalysis and Science Technology*, Springer Verlag, New York, 1st edn., 1981.

196 M. Matsuka, R. D. Braddock, T. Hanaoka, K. Shimura, T. Miyazawa and S. Hirata, *Energy & Fuels*, 2016, **30**, 7971–7981.

197 H. Arakawa and A. T. Bell, *Ind. Eng. Chem. Process Des. Dev.*, 1983, **22**, 97–103.

198 M. Vannice, *J. Catal.*, 1975, **37**, 449–461.

199 S. K. Das, S. Majhi, P. Mohanty and K. K. Pant, *Fuel Process. Technol.*, 2014, **118**, 82–89.

200 R. Dictor, *J. Catal.*, 1986, **97**, 121–136.

201 M. E. Dry and A. P. Steynberg, in *Fischer-Tropsch Technology (Studies in Surface Science and Catalysis)*, eds. A. P. Steynberg and M. E. Dry, Elsevier B.V., Amsterdam, 1st edn., 2004, vol. 152, ch 5, p. 406.

202 R. Snel, *J. Mol. Catal.*, 1989, **53**, 143–154.

203 F. Buciuman, F. Patcas, R. Craciun and D. R. T. Zahn, *Phys. Chem. Chem. Phys.*, 1999, **1**, 185–190.

204 F. Arena, T. Torre, C. Raimondo and A. Parmaliana, *Phys. Chem. Chem. Phys.*, 2001, **3**, 1911–1917.

APPENDIX A

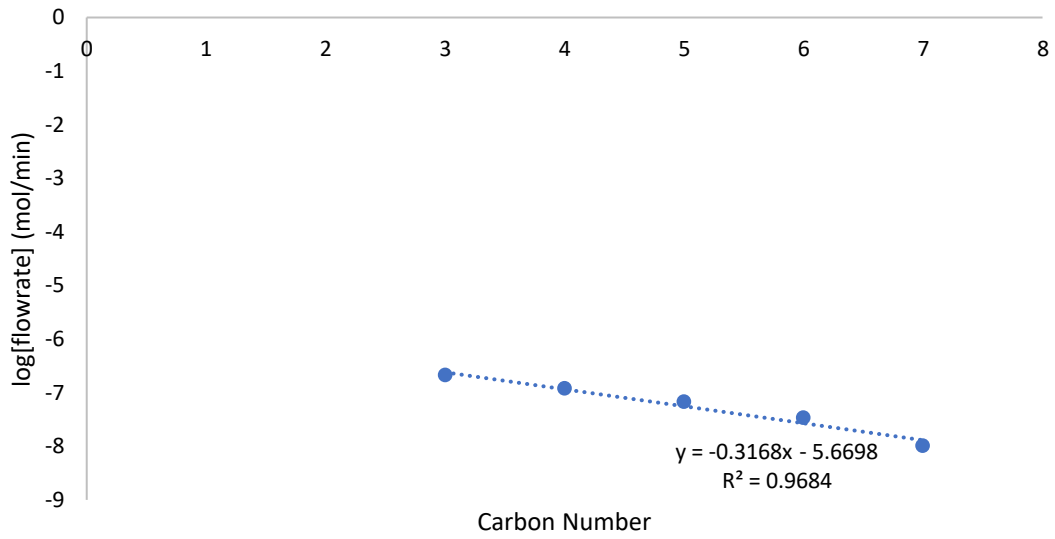

.

Figure A-1 Example of the Anderson-Schulz-Flory (ASF) 'plot'.

Extrapolated Carbon Number (C_n) converted:

$$\log[flowrate\ for\ C_n] = -0.3168\ (C_n) - 5.6698 = X$$

$$flowrate\ for\ C_n = 10^X$$

Sum of flowrate for C_{5+}:

$$\sum_{5}^{100} C_n$$